7-6-2017

Design, Synthesis and Characterization of Transition Metal Oxide/Sulfide-Based Catalysts for Environmental and Energy Applications

Ran Miao
miaoran8847@gmail.com

Design, Synthesis and Characterization of Transition Metal Oxide/Sulfide-Based Catalysts for Environmental and Energy Applications

Ran Miao, Ph.D.

University of Connecticut, 2017

In this thesis, I will focus on the synthesis of transition metal oxide/sulfide-based composite materials for different types of environmental and sustainable energy applications under ambient conditions. Controlled synthesis of these catalysts with unique crystalline structures, physical, and chemical properties will be carried out to achieve an improved catalytic activity. The correlations between the material structure and catalytic activity will be investigated by various characterization techniques. Finally, the catalytic activities for the resulting materials will be evaluated for environmental friendly photocatalytic dye degradation and electrochemical water splitting reaction, respectively.

In the first part, I will demonstrate the design of a carbon quantum dots (CQDs)/mesoporous TiO_2 composite using a recently developed inverse micelle sol-gel method. In order to exploit full usage of the visible spectrum of sunlight, CQDs were introduced into the titanium oxide due to the up-conversion property and electron withdrawing property. The proposed CQDs modified mesoporous TiO_2 maintained the pure anatase phase and mesoporous structure, and exhibited high adsorption capacity and excellent visible light photocatalytic activity under ambient conditions.

In the second part, I helped develop a reduced graphene oxide supported Ni-Mn-Co ternary oxide nanocomposite synthesized by a two-step solvothermal synthesis followed by calcination under inert gas, during which GO is further reduced to rGO (denoted as rGO/NMC). The resulting

product was further converted into a corresponding sulfide via a direct sulfurization reaction (denoted as rGO/NMC-S). Based on the experimental results, the obtained rGO/NMC composites exhibit a comparable OER electrocatalytic activity than the state-of-the-art RuO2 and IrO2 catalysts, and the as-converted rGO/NMC sulfide composites present an efficient HER activity under alkaline conditions. Density functional theory (DFT) calculations were performed to better understand the nature of the HER reaction processes. The results indicate a higher preferability of the HER reaction for sulfide surfaces than oxide surfaces.

The third part exhibits the preparation of mesoporous FeS_2 with high surface area. The resulting material was synthesized via a facile two-step synthetic protocol including inverse micelle sol-gel method followed by low-temperature sulfurization treatment. The structure of the resulting material was studied via multiple characterization techniques. The mesoporous FeS_2 material exhibit superior performance as a HER electrocatalyst under alkaline conditions.

Design, Synthesis and Characterization of Transition Metal Oxide/Sulfide-Based Catalysts for Environmental and Energy Applications

Ran Miao

B.E., East China University of Science and Technology, China, 2010

A Dissertation

Submitted in Partial Fulfillment of the

Requirements for the Degree of

Doctor of Philosophy

at the

University of Connecticut

2017

APPROVAL PAGE

Doctor of Philosophy Dissertation

Design, Synthesis and Characterization of Transition Metal Oxide/Sulfide-Based Catalysts for Environmental and Energy Applications

Presented by

Ran Miao, B.E.

Major Advisor _____

Steven L. Suib

Associate Advisor _____

Alfredo Angeles-Boza

Associate Advisor _____

Jing Zhao

University of Connecticut
2017

Dedicated to my family and all my friends

Acknowledgement

I would like to express my sincere gratitude to my advisor Dr. Steven L. Suib for his support, encouragement, and guidance throughout my graduate studies. He is the best advisor anyone can ask for. Things I have learned from Dr. Suib are not only all about research, but also the enthusiasm to work, the positive altitude to life, and the responsibility to others. I am also grateful to my associate advisors, Dr. Alfredo Angeles-Boza, Dr. Jing Zhao, Dr. S. Pamir Alpay, and Dr. Fatma Selampinar for their generous help and advice. Also, I greatly appreciate Dr. Frank Galasso for his suggestion and motivation throughout my Ph.D. life, and Mrs. Bonnie Suib for giving me courage and help.

My sincere thanks also go to my colleagues for their helpful discussion and generous contributions to my research and Ph.D. life, Dr. Zhu Luo, Dr. Sheng-Yu Chen, Dr. Sanjubala Sahoo, Dr. Curtis Guild, Dr. Sourav Biswas, Dr. Yongtao Meng, Dr. Wenqiao Song, Dr. Ting Jiang, Dr. Jing Jin, Dr. David Kriz, Dr. Saiful Islam, Dr. Chung-Hao Kuo, Dr. Abdelhamid El-Sawy, Dr. Lakshitha Pahalagedara, Dr. Madhavi Pahalagedara, Dr. Yashan Zhang, Dr. Niluka Wasalathanthri, Junkai He, Wei Zhong, Biswanath Dutta, Tahereh Jafari, Mahbubur Shakil, Yang Wu, Ehsan Moharreri, Shanka Dissanayke, and everyone else in Suib's group. I also thank the teaching faculty and chemistry department staff, Dr. William Willis, Dr. You-Jun Fu, Dr. Clyde Cady, Dr. Joseph DePasquale, Charlene Fuller, Emilie Hogrebe, Osker Dahabsu, Joshua Strecker, and all the undergraduate laboratory staff.

Finally, I especially thank my parents and my husband, Xiaojiao Xu. Their unconditional love and support keep me moving forward when times are rough. I could not imagine myself getting this far without them.

Table of Contents

List of Figures

List of Tables

Chapter 1. Introduction

1.1 Overview

Increasing environmental issues and depletion of fossil fuels has motivated intense research on the development of efficient catalytic systems. The use of heterogeneous catalysts for environmental contamination control and sustainable energy production has attracted widespread attention. Among various heterogeneous catalysts, first-row transition metal oxides and sulfides, such as TiO_2, Co_3O_4, MnO_2, NiO, and FeS_2, are of considerable interest due to their low cost and high abundance in the earth.[1–4] Moreover, the physicochemical properties including oxidation states, morphology, crystallinity, and particle size are easy to modify via controlled material synthesis protocol. The transition metal-based metal oxides and sulfides have been widely used as heterogeneous catalysts in a variety of different applications, such as photocatalytic reactions, adsorption, heterogeneous catalytic reactions, and electricity-driven water splitting.[5–8]

In order to further enhance the catalytic activities of the heterogeneous transition metal-based catalysts, numerous protocols have been utilized for a modification, including doping,[9] structural changes,[10] and construction of nanocomposite with carbonaceous species.[11] A great number of nanocarbon fabricated metal oxide composite materials have been developed and have shown remarkable merits toward catalytic reactions.[12–14] The nanocarbon materials include graphene, carbon nanotubes, carbon quantum dots and their derivatives.[15] Apart from nanocarbon-based composite materials, mesoporous transition metal oxide and sulfide materials have also received tremendous research interest in the past decades.[16,17]

To achieve superior catalytic performance, nanocarbon modified transition metal-based materials and mesoporous transition metal oxide/sulfide materials were synthesized, characterized, and investigated in this thesis. The above catalysts were applied to photocatalytic dye degradation, electrochemical oxygen evolution reaction, and hydrogen evolution reaction which are separated into three chapters in this dissertation.

1.2 Background and Significance

1.2.1 Titanium Dioxide Photocatalyst in Dye Degradation Reaction

The development of highly efficient heterogeneous photocatalysts for the dye degradation has been a focus in a wide range of research fields, especially for energy and environmental-related field.[18,19] In a typical photocatalytic process, the photo-generated electron will be excited under the illumination of solar light from the valence band (VB) to the conduction band (CB) if the photon energy is equal to or greater than that of the band gap of the photocatalyst, and leave behind a photo-generated hole in the VB. Once the charge carriers separated, they will migrate to the surface of photocatalyst and drive aqueous contamination removal process. The electrons in the semiconductor conduction band will diffuse to the surface to further react with molecular oxygen to produce superoxide anion radicals ($O_2^{\bullet-}$). Meanwhile, the photogenerated holes in the valence band will migrate to the surface and then react with hydroxyl species to form active hydroxyl radicals ($OH^{\bullet}$).

There are many properties of the photocatalyst have a significant effect on the photocatalytic performance, including stability, toxicity, surface area, crystallinity, and transparency to sunlight.[20] Among various photocatalysts, Titanium dioxide (TiO_2) has been regarded as a promising photocatalyst due to its non-toxic nature, low cost, and long-term stability against photo-corrosion.[20,21] However, the wide application of commercial TiO_2 is limited by the low response

under visible light irradiation and nonporous character.[22] Therefore, numerous protocols have been used to modify TiO_2 materials to achieve an improved photocatalytic performance, such as doping TiO_2 with foreign elements,[9] sensitizing,[23] structural modification,[24] construction of a hybrid structure.[19]

1.2.2 Transition Metal-Based Electrocatalyst for Electrocatalytic Water Splitting

Growing depletion of fossil fuels has motivated intense research on the generation of clean and sustainable energy alternatives.[25] In order to meet the global demand for renewable energy supplies, hydrogen is considered as a promising chemical fuel,[22] owing to its high specific energy (142 kJ/g), high abundance as a natural source, and is environmentally benign merit since no pollutant other than water is produced as a by-product.[26,27] Nowadays, industrial hydrogen production is based on the steam reforming process from hydrocarbon fuels, but the process involves high temperatures and pressure treatments, and carbon dioxide release. Growing concern about global warming urged the development of a clean and sustainable pathway to generate hydrogen fuel. Electrochemical water splitting into hydrogen and oxygen has been regarded as an appealing approach to fulfilling energy conversion.

Currently, the state-of-the-art catalysts for hydrogen evolution reaction (HER) are Pt-based materials, and the most efficient catalysts that catalyze oxygen evolution reaction (OER) are RuO_2 and IrO_2. However, the high cost and low abundance of these materials limited their widespread industrial applications. In addition, the OER process suffers from intrinsically sluggish reaction kinetics due to multiple proton-coupled electron transfers, which makes the development of electrode materials more critical.[28–30] Due to the sluggish kinetics of the OER on the anode and high cost of the state-of-the-art water splitting catalysts, substantial efforts have been made to develop highly efficient and non-noble transition metal based electrocatalysts.[31]

Transition metal oxides and sulfides have shown desirable electrocatalytic performance toward OER and HER such based on non-precious earth-abundant metals such as Ni,[32] Mn,[33] Co,[34] Fe,[35] and Mo.[36] In particular, Co-based OER electrocatalysts have demonstrated their superior catalytic behavior. Wu et al.[37] developed a stable cobalt nanoparticles assembled into a monolayer array, which exhibits excellent OER activity. Jin et al.[34] synthesized a cobalt-cobalt oxide-carbon hybrid electrode material and applied to HER and OER processes, inspired by the favorable H atom binding energy of metallic cobalt. On the basis of the appealing merits of transition metals, the formation of mixed metal oxides/sulfides have been widely investigated and shown to be a family of promising electrocatalysts, benefiting from their remarkable electrical conductivity.[38] The electrocatalytic performance can be greatly improved by adjusting the structural and compositional features of the mixed metal ternary materials. Based on the current progress, the design of highly active mixed transition-metal ternary oxide and sulfide for water splitting reaction is crucial for electrochemical energy conversion process.

1.2.3 Mesoporous Transition Metal Sulfide as Electrocatalyst in Hydrogen Evolution Reaction

In pursuit of an inexpensive and earth-abundant alternative to Pt as the HER electrocatalyst, a great deal of effort has been made. Metal sulfides have risen as promising alternatives to Pt-based materials, oxides, and hydroxides as cathode materials.[39] Intensive research efforts have been devoted to investigating the HER catalytic activity of molybdenum disulfide (MoS_2) since the earliest work by Hinnemann and co-workers.[40] The MoS_2 edge structure features similar properties to the active centers of hydrogen producing enzyme. Kong et al.[41] studied the first-row transition metal chalcogenides such as CoS_2, NiS_2 that possess the pyrite or marcasite structure with undercoordinated surface cations, which exhibit similar structural features as the natural enzyme.

This indicates that they might be promising candidates for HER. Pyrite iron sulfide (FeS_2) is another sulfide material of great interest, even though there are few existing studies focused on catalytic activity for HER. The most common approach of synthesizing metal sulfides is solvothermal method by using thiourea or thioacetamide as sulfur source.[42–44] However, the HER catalytic activity is restrained by the limited number of active sites due to the low surface area.

To satisfy the high requirement of water electrolysis, efficient and innovative electrode materials with enhanced performances are highly demanded. Efforts have been made to modify the metal sulfide-based materials with various functional materials, such as carbonaceous materials,[45] precious metal support,[46] doping with foreign elements,[47] and other metal oxides or sulfides.[48] Apart from synthesizing the hybrid structure materials, optimized properties and enhanced performances can also be achieved via preparing the mesoporous metal chalcogenides as electrode materials. The development of mesoporous transition metal oxide materials synthesis have been a focus of tremendous attention since the pioneering work done by Mobil researchers.[49] Mesoporous materials represent the solid materials within a network with a distribution of pores in the range of 2-50 nm.[50] Great interest in the field of mesoporous materials is due to their tunable intrinsic properties such as surface area, pore size, pore volume, and various mesostructures, which endow them to be promising candidates for numerous potential applications in adsorption, separations, gas sensors, catalysis, lithium-ion batteries, and fuel cells.[16, 50–53]

1.3 References

(1) Zhou, W.; Li, W.; Wang, J.-Q.; Qu, Y.; Yang, Y.; Xie, Y.; Zhang, K.; Wang, L.; Fu, H.; Zhao, D. *J. Am. Chem. Soc.* **2014**, *136* (26), 9280.

(2) Meng, Y.; Song, W.; Huang, H.; Ren, Z.; Chen, S.; Suib, S. L. *J. Am. Chem. Soc.* **2014**, *136*, 11452.

(3) Li, Y.; Hasin, P.; Wu, Y. *Adv. Mater.* **2010**, *22* (17), 1926.

(4) Samad, L.; Caba, M.; Shearer, M. J.; Park, K.; Hamers, R. J.; Jin, S. *Chem. Mater.* **2015**, *27*, 3108.

(5) Li, W.; Wu, Z.; Wang, J.; Elzatahry, A. A.; Zhao, D. *Chem. Mater.* **2014**, *26*, 287.

(6) Poyraz, A. S.; Song, W.; Kriz, D.; Kuo, C.; Seraji, M. S.; Suib, S. L. *ACS Appl. Mater. Interfaces* **2014**, *6*, 2.

(7) Fominykh, K.; Chernev, P.; Zaharieva, I.; Sicklinger, J.; Stefanic, G.; DoBlinger, M.; Mu, A.; Pokharel, A.; Bo, S.; Scheu, C.; Bein, T.; Fattakhova-rohlfing, D. *ACS Nano* **2015**, *9* (5), 5180.

(8) Faber, M. S.; Lukowski, M. A.; Ding, Q.; Kaiser, N. S.; Jin, S. *J. Phys. Chem. C* **2014**, *118*, 21347.

(9) Zeng, L.; Lu, Z.; Li, M.; Yang, J.; Song, W.; Zeng, D.; Xie, C. *Appl. Catal. B Environ.* **2016**, *183*, 308.

(10) Song, W.; Poyraz, A. S.; Meng, Y.; Ren, Z.; Chen, S.; Suib, S. L. *Chem. Mater.* **2014**, *26*, 4629.

(11) Ma, W.; Ma, R.; Wang, C.; Liang, J.; Liu, X.; Zhou, K. *ACS Nano* **2015**, *9* (2), 1977.

(12) Liang, Y.; Li, Y.; Wang, H.; Zhou, J.; Wang, J.; Regier, T.; Dai, H. *Nat. Mater.* **2011**, *10* (10), 780.

(13) Yang, S.; Feng, X.; Ivanovici, S.; Müllen, K. *Angew. Chemie - Int. Ed.* **2010**, *49* (45), 8408.

(14) Wang, H.; Wei, Z.; Matsui, H.; Zhou, S. *J. Mater. Chem. A* **2014**, *2*, 15740.

(15) Wang, D. W.; Su, D. *Energy Environ. Sci.* **2014**, *7*, 576.

(16) Sun, L.-B.; Liu, X.-Q.; Zhou, H.-C. *Chem. Soc. Rev.* **2015**, *44* (15), 5092.

(17) Yonemoto, B. T.; Hutchings, G. S.; Jiao, F. *J. Am. Chem. Soc.* **2014**, *136*, 8895.

(18) Kudo, A.; Miseki, Y. *Chem. Soc. Rev.* **2009**, *38* (1), 253.

(19) Regulacio, M. D.; Han, M. *Acc. Chem. Res.* **2015**, *49* (3), 511.

(20) Nakata, K.; Fujishima, A. *J. Photochem. Photobiol. C Photochem. Rev.* **2012**, *13*, 169.

(21) Scanlon, D. O.; Dunnill, C. W.; Buckeridge, J.; Shevlin, S. a; Logsdail, A. J.; Woodley, S. M.; Catlow, C. R. a; Powell, M. J.; Palgrave, R. G.; Parkin, I. P.; Watson, G. W.; Keal, T. W.; Sherwood, P.; Walsh, A.; Sokol, A. a. *Nat. Mater.* **2013**, *12*, 798.

(22) Moniz, S. J. a.; Shevlin, S. a.; Martin, D. J.; Guo, Z.-X.; Tang, J. *Energy Environ. Sci.* **2015**, *8*, 731.

(23) Hurum, D. C.; Agrios, A. G.; Gray, K. A.; Rajh, T.; Thurnauer, M. C. *J. Phys. Chem. B*

2003, *107*, 4545.

(24) Alvaro, M.; Aprile, C.; Benitez, M.; Carbonell, E. *J. Phys. Chem. B* **2006**, *110*, 6661.

(25) Yuan, L.; Han, C.; Yang, M.-Q.; Xu, Y.-J. *Int. Rev. Phys. Chem.* **2016**, *35*, 1.

(26) Thomas, G. *Annu. Rev.* **2000**.

(27) Acar, C.; Dincer, I.; Zamfirescu, C. *Int. J. energy Res.* **2014**, *38*, 1903.

(28) Li, R.; Wei, Z.; Gou, X. *ACS Catal.* **2015**, *5*, 4133.

(29) Chang, J.; Xiao, Y.; Xiao, M.; Ge, J.; Liu, C.; Xing, W. *ACS Catal.* **2015**, *5*, 6874.

(30) Shan, Z.; Archana, P. S.; Shen, G.; Gupta, A.; Bakker, M. G.; Pan, S. *J. Am. Chem. Soc.* **2015**, *137* (37), 11996.

(31) Wang, J.; Zhong, H.; Wang, Z.; Meng, F.; Zhang, X. *ACS Nano* **2016**, *10*, 2342.

(32) Feng, L.-L.; Yu, G.; Wu, Y.; Li, G.-D.; Li, H.; Sun, Y.; Asefa, T.; Chen, W.; Zou, X. *J. Am. Chem. Soc.* **2015**, *137*, 14023.

(33) Huynh, M.; Shi, C.; Billinge, S. J. L.; Nocera, D. G. *J. Am. Chem. Soc.* **2015**, *137*, 14887.

(34) Jin, H.; Wang, J.; Su, D.; Wei, Z.; Pang, Z.; Wang, Y. *J. Am. Chem. Soc.* **2015**, *137* (7), 2688.

(35) Gong, M.; Li, Y.; Wang, H.; Liang, Y.; Justin, Z.; Zhou, J.; Wang, J.; Regier, T.; Wei, F.; Dai, H.; Wu, J. Z. *J. Am. Chem. Soc.* **2013**, *135*, 8452.

(36) Vrubel, H.; Hu, X. *Angew. Chemie Int. Ed.* **2012**, *51*, 12703.

(37) Wu, L.; Li, Q.; Wu, C. H.; Zhu, H.; Mendoza-Garcia, A.; Shen, B.; Guo, J.; Sun, S. *J. Am. Chem. Soc.* **2015**, *137* (22), 7071.

(38) Yuan, C.; Wu, H. Bin; Xie, Y.; Lou, X. W. *Angew. Chemie - Int. Ed.* **2014**, *53* (6), 1488.

(39) Anantharaj, S.; Ede, S. R.; Sakthikumar, K.; Karthick, K.; Mishra, S.; Kundu, S. *ACS Catal.* **2016**, *6*, 8069.

(40) Hinnemann, B.; Moses, P. G.; Bonde, J.; Jørgensen, K. P.; Nielsen, J. H.; Horch, S.; Chorkendorff, I.; Nørskov, J. K. *J. Am. Chem. Soc.* **2005**, *127*, 5308.

(41) Kong, D.; Cha, J. J.; Wang, H.; Lee, H. R.; Cui, Y. *Energy Environ. Sci.* **2013**, *6*, 3553.

(42) Cell, D. S.; Kung, C.; Chen, H.; Lin, C.; Huang, K.; Vittal, R.; Ho, K. *ACS Nano* **2012**, *6* (8), 7016.

(43) Xie, J.; Zhang, J.; Li, S.; Grote, F.; Zhang, X.; Zhang, H.; Wang, R.; Lei, Y.; Pan, B.; Xie, Y. *J. Am. Chem. Soc.* **2013**, *135*, 17881.

(44) Shukla, S.; Loc, N. H.; Boix, P. P.; Koh, T. M.; Prabhakar, R. R. *ACS Nano* **2014**, *8*, 10597.

(45) Wang, H. L.; Liang, Y. Y.; Li, Y. G.; Dai, H. J. *Angew. Chemie-international Ed.* **2011**, *50* (46), 10969.

(46) Gao, M.-R.; Gao, Q.; Jiang, J.; Cui, C.-H.; Yao, W.-T.; Yu, S.-H. *Angew. Chemie Int. Ed.* **2011**, *50* (21), 4905.

(47) Wang, D.; Gong, M.; Chou, H.; Pan, C.; Chen, H.; Wu, Y.; Lin, M.; Guan, M.; Yang, J.; Chen, C.; Wang, Y.; Hwang, B.; Chen, C.; Dai, H. *J. Am. Chem. Soc.* **2015**, *137*, 1587.

(48) Reaction, H.; Xu, J.; Cui, J.; Guo, C.; Zhao, Z.; Jiang, R.; Xu, S.; Zhuang, Z.; Huang, Y.; Wang, L.; Li, Y. *Angew. Chemie Int. Ed.* **2016**, *55*, 6502.

(49) Kresge, C. T.; Leonowicz, M. E.; Roth, W. J.; Vartuli, J. C.; Beck, J. S. *Nature* **1992**, *359*, 710.

(50) Walcarius, A. *Chem. Soc. Rev.* **2013**, *42* (9), 4098.

(51) Bao, N.; Li, Y.; Wei, Z.; Yin, G.; Niu, J. *J. Phys. Chem. C* **2011**, *115* (13), 5708.

(52) Zhou, W.; Li, W.; Wang, J.-Q.; Qu, Y.; Yang, Y.; Xie, Y.; Zhang, K.; Wang, L.; Fu, H.; Zhao, D. *J. Am. Chem. Soc.* **2014**, *136* (26), 9280.

(53) Gu, D.; Schűth, F. *Chem. Soc. Rev.* **2014**, *43*, 313.

Chapter 2. Mesoporous TiO_2 Modified with Carbon Quantum Dots as a High-Performance Visible Light Photocatalyst

2.1 Introduction

Environmental and energy concerns have attracted significant attention on the development of highly efficient heterogeneous photocatalysts for the degradation of various kinds of organic contaminants.[1–3] Semiconductors have been widely studied as photocatalysts due to their wide absorbance range. Among the common semiconductors, such as iron oxide,[4] copper oxide,[5] and zinc oxide,[6] titanium dioxide (TiO_2) has been widely studied and utilized in many photocatalytic applications. As a result of its long-term chemical and optical stability, strong oxidizing ability, nontoxicity, and low cost, TiO_2 is considered to be the most efficient photocatalyst to date.[7] The photocatalytic properties of TiO_2 are attributed to the production of photogenerated electrons in the conduction band (CB) and holes in the valence band (VB), which occur upon the radiation of ultraviolet (UV) light (10-400 nm). The photogenerated electrons and holes diffuse to the TiO_2 surface and form highly reactive radicals ($OH^{\bullet}$, $O_2^{\bullet -}$), which are capable of oxidizing nearby organic molecules.[8–11] Among various TiO_2 materials reported, commercial TiO_2 (Degussa P25) is a benchmark photocatalyst and has been widely studied. P25 is a mixed phase TiO_2 material with 70-80% anatase and 30-20% rutile.[12,13] The remarkable photocatalytic efficiency contributes to the synergistic effect between anatase and rutile phases.[14,15] However, due to the relatively large band gap (3.0-3.2 eV), TiO_2 can only absorb short wavelength light, which falls in the UV region.[16,17] Given that the entire solar light consists of less than 5% ultraviolet light, the photocatalytic activity of TiO_2 under natural sunlight is largely limited.[18] In addition, commercial P25 is nonporous and has a relatively low surface area, which impedes the adsorption of target

molecules, thus lowering the photocatalytic efficiency.[19] Therefore, the design of a high surface area and visible light responsive photocatalytic system has become an urgent task.[16,20]

Mesoporous materials are considered as excellent catalysts for applications requiring high surface area and large amount of active sites, due to their tunable structural properties such as surface area, pore volume, size, and nanocrystallinity.[21,22] Mesoporous titanium dioxide that combines a photoactive framework and an open porous structure is of great interest.[23] Mesoporous TiO_2 applied in the photocatalysis area has been extensively reported. Li et al.[24] synthesized gold nanoparticles embedded in a mesoporous titania photocatalyst and showed that gold nanoparticles are well dispersed in the mesoporous TiO_2 networks. The mesoporous channels offer a larger surface area and enhanced accessibility than P25. Feng et al.[25] reported that mesoporous titanium dioxide exhibits an enhanced photoreactivity relative to P25 due to the synergetic effects of the mesoporosity and light-transmittance ability of the catalysts. Zhu et al.[26] prepared flowerlike hierarchical TiO_2 materials with a high surface area and mesoporous channels, which exhibit good photocatalytic performance towards degradation of methylene blue. Both the mesoporous structure and unique morphology contributed to the enhanced activity compared to commercial TiO_2. However, the main drawbacks of conventional mesoporous TiO_2 materials are their poorly ordered mesoporous structure, low crystallinity, and low thermal stability. In 2013, our group has developed a general inverse micelle sol-gel approach for the preparation of a series of mesoporous metal oxide materials, which are called UCT materials (University of Connecticut mesoporous materials).[27] The inverse micelle sol-gel method used Pluronic P123 as a surfactant species, which formed inverse micelles in at low pH conditions. The presence of nitrate ions facilitates the penetration of positively charged metal nitro-clusters into the inverse micelle followed by a thermal decomposition of nitrate ions into nitric oxide species, which controlled the sol-gel chemistry. The 1-butanol, which served as an interface modifier and solvent, further prevented the undesirable aggregation. The subsequent calcination treatment generates thermally stable and

crystalline mesoporous materials with monomodal and tunable pore sizes. The UCT materials have been used in various applications, such as photocatalytic reactions,[28] water oxidation,[29] methane oxidation,[30] and CO oxidation.[31] Based on the inverse micelle sol-gel process, mesoporous TiO_2 (UCT-62) has been synthesized in this study.

In an attempt to improve the visible light photocatalytic activity of metal oxides, carbon nano-species have been utilized as modifying materials recently.[32–34] In terms of photophysical properties, carbon quantum dots have been found to possess excellent up-conversion photoluminence (UCPL). Up-conversion is a process where lower-energy light (near-infrared or infrared) is converted to higher-energy light (ultraviolet or visible) through multiple photon absorption. That is usually achieved via the use of lanthanide, actinide ions, transition metals, and semiconductor quantum dots.[35–38] Compared to down-conversion materials, materials with an up-conversion property are less common and more versatile, which are able to utilize the visible spectrum of sunlight, resulting in an improved photocatalysis efficiency.[39,40] Due to their unique optical properties such as bright fluorescence and strong absorption, CQDs have received much interest. Compared to the traditional metallic quantum dots, which are limited in use due to environmental hazard issues,[41,42] CQDs possess low toxicity, good biocompatibility, high photostability, high aqueous solubility, strong emission, high natural abundance, and also are an electron reservoir.[39,43–46] Therefore, CQDs have gradually become promising carbon nanomaterials. Considerable work has been done on photocatalytic dye degradation with quantum dot-based materials, but only a few researchers are using CQDs on mesoporous materials. Yu et al.[2] developed CQDs embedded in a mesoporous hematite complex photocatalyst, which led to a high degradation efficiency of 97% for MB with the assistance of H_2O_2 under visible light. The intimate contact between CQDs and mesoporous hematite facilitated the electron transfer, and thus inhibited the electron-hole recombination. However, this photocatalyst requires coexistence of a strong oxidizing agent during the photocatalytic tests.

The CQDs embedded in mesoporous TiO_2 composite photocatalytic systems have not been reported previously. In this work, we demonstrated the design of a CQDs/mesoporous TiO_2 (UCT-62) composite to exploit full usage of the visible spectrum of sunlight based on the up-conversion property of CQDs. The CQDs modified mesoporous TiO_2 maintained the pure anatase phase and mesoporous structure, and exhibited high adsorption capacity and excellent visible light photocatalytic activity under ambient conditions.

2.2 Experimental Section

2.2.1 Chemicals

Titanium (IV) isopropoxide (≥ 97%). 1-butanol (anhydrous, 99.8%), Poly(ethylene glycol)-block-Poly(propylene glycol)-block-Poly (ethylene glycol) PEO_{20}-PPO_{70}-PEO_{20} (Pluronic P123), L-ascorbic acid were purchased from Sigma-Aldrich. Concentrated nitric acid (HNO_3, 68-70%) was purchased from J. T. Baker. All chemicals were used as received and used without further purification.

2.2.2 Preparation of Meso-Ti-X and CQDs/meso-Ti-X

The mesoporous TiO_2 was synthesized by the recently developed inverse micelle template sol-gel approach.[27] In a typical synthesis, 2.84 g (0.01 mol) of titanium isopropoxide was dissolved in a solution containing 7.0 g (0.094 mol) of 1-butanol, 1.0 g (0.016 mol) of HNO_3 and 1.0 g (1.72×10^{-4} mol) of P123 surfactant in a 150 mL beaker at room temperature (RT) under magnetic stirring to obtain a clear gel. The formed clear gel was placed in an oven heated at 120 °C for 4 h, followed by a heat treatment under air at 250, 350, 450, 550 °C for 4 h, respectively. The as-prepared sample was labeled as meso-Ti-X (X=250, 350, 450, and 550), representing the calcination treatment temperature. The carbon quantum dots were synthesized by an ultrasonic-

hydrothermal method. L-ascorbic acid was used as the carbon source. L-ascorbic acid (1.0 g) was dissolved in a mixture of deionized water and anhydrous ethanol and treated ultrasonically for 2 h. Then, the obtained clear solution was transferred to a Teflon-lined stainless steel autoclave with a volume of about 23 mL, sealed and maintained at 160 °C for 4 h. The reaction mixture was then cooled to room temperature and extracted with dichloromethane. The water phase solution was collected and dialyzed. The above samples were labeled CQDs. Subsequently, 0.2 g meso-Ti-450 was dispersed in a suitable amount of CQDs solution. After continuous stirring the mixture for 30 min, the resulting mixture was washed with water, and dried in a vacuum oven at 80 °C to produce the CQDs/meso-Ti-450 composites. CQDs/meso-Ti-450 composites with different CQDs loading amounts were fabricated by adjusting the as-prepared CQDs amount.

2.2.3 Characterization of Meso-Ti-450 and CQDs/meso-Ti-450

All the synthesized materials were ground to a fine powder in an agate mortar. The Powder X-ray diffraction (XRD) analysis was carried out at room temperature on a Rigaku Ultima IV diffractometer (Cu Kα radiation, λ = 1.5406 A). A beam voltage of 40 kV and a current of 44 mA were used. The morphologies of the CQDs/meso-Ti-450 materials were investigated using an FEI Nova NanoSEM 450 with an accelerating voltage of 2.0 kV. Transmission electron microscopy (TEM) and high-resolution transmission electron microscopy (HRTEM) images were collected using a JEOL 2010 UHR FasTEM microscope operating at 200 kV. Fluorescence spectra were collected on an Agilent Cary 50 Eclipse fluorescence spectrophotometer using a 1.0 cm quartz cuvette. The excitation wavelength was set in the range of 350-750 nm. N_2 sorption measurements were performed on a Quantachrome Autosorb-1-1C automated sorption system. The samples were degassed at 150 °C for 4 h prior to the experiments. The surface areas were calculated by the Brunauer−Emmett−Teller (BET) method, and the pore size distributions were obtained by the Barrett−Joyner−Halenda (BJH) method from the desorption branch of the isotherms. The

thermogravimetric analysis (TGA) was performed using a Hi-Res TA instrument Model Q100, in the temperature range between 25 and 800 °C at a ramping rate of 10 °C min^{-1} in an air atmosphere. Raman spectra were taken on a Renishaw 2000 Raman microscope with an Ar^+ ion laser (514 nm) as the excitation source. Diffuse reflectance ultraviolet-visible (DR UV-vis) spectra of the powder samples were obtained with a diffuse reflectance apparatus attached to a Shimadzu UV-2450 ultraviolet-visible spectrophotometer. The powder samples were diluted with barium sulfate in proportions of 10 to 1, and pressed into the sample holder. X-ray photoelectron spectroscopy (XPS) measurements were performed in a PHI model 590 spectrometer with multiprobes (Al Kα radiation, λ = 1486.6 eV, operated at 250 W).

2.2.4 Photocatalytic Activity Under Visible Light Irradiation

The adsorption capacity was first investigated by dispersing 50 mg of photocatalyst in 50 mL of MB dye solution (1×10^{-4} M) under dark conditions for 100 min. Adsorption capacity was calculated by the ratio of dye concentration after adsorption (C) to that before adsorption (C_0). The photocatalytic activity of CQDs/meso-Ti-450 was investigated based on the photocatalytic degradation of Methyl Blue (MB) and N-Benzylideneaniline. Experiments were carried out in a Rayonet Model RPR-100 photochemical reactor. A magnetic stirrer was placed at the center of the photoreactor. A 1000 W halogen lamp with a cutoff filter (λ > 450 nm) was used as a constant, separate, and intense visible light source. The photoreactor was covered with aluminum foil to reduce the effect of interference by ambient light. For MB degradation, 50 mg of CQDs/meso-Ti-450 was dispersed in a 50 mL MB dye solution (1×10^{-4} M) in a 200 mL glass beaker. For N-Benzylideneaniline degradation, 50 mg of photocatalyst and 50 mL 20 ppm of N-Benzylideneaniline aqueous solution were applied. After 1 h of vigorous stirring in the dark, the solution was transferred with a magnetic stirrer inside the photochemical reactor, and the visible light lamps were turned on. The dye solution containing photocatalyst was kept stirring under

irradiation for 2 or 3 h. A 3 mL sample solution was collected every 20 min. After removing the photocatalyst with centrifuging, the clear solution was analyzed in a UV-vis spectrometer. Dye degradation efficiency was calculated by the ratio of absorbance intensity (I/I0, where I and I0 are the final and initial absorbance intensity, respectively). For MB degradation, calculations were based on the absorbance intensity of the 665 nm peak. For N-Benzylideneaniline, calculations were based on intensity of the 252 nm absorbance. After the dye degradation tests, the photocatalysts were collected and washed with ethanol several times until methylene blue molecules desorbed back into solution. Then the photocatalyst powder was dried at 80 °C overnight. The subsequent recycle tests were carried out using the same photocatalytic reaction conditions as above. The stability test was conducted with the CQDs/meso-Ti-450 sample after the third recycle test by wide angle XRD techniques. To compare with the CQDs/meso-Ti-450, CQDs modified P25 material was prepared using the same method as CQDs/meso-Ti-450. The commercial P25 was used as received and without further treatment. The obtained sample was labeled as CQDs/P25. The photocatalytic degradation of MB was also performed in the absence of oxygen. The experimental procedure was the same as described above, except for purging nitrogen gas during the visible light irradiation to remove dissolved oxygen.

2.3 Results

2.3.1 Physiochemical Properties of mesoporous TiO_2

Figure 2.1 shows both the wide angle and low angle diffraction lines for titanium oxide materials calcined at different temperatures. All materials exhibit a typical anatase TiO_2 crystalline pattern according to JCPDS card (No. 00-021-1272). Increasing calcination temperature leads to a better crystallinity (**Figure 2.1a**). The low angle diffraction peak is an indicator of a regular mesopore structure in soft-template prepared mesoporous materials. Since most mesoporous materials are amorphous on the atomic scale and process large unit cells, the diffraction angles are relatively

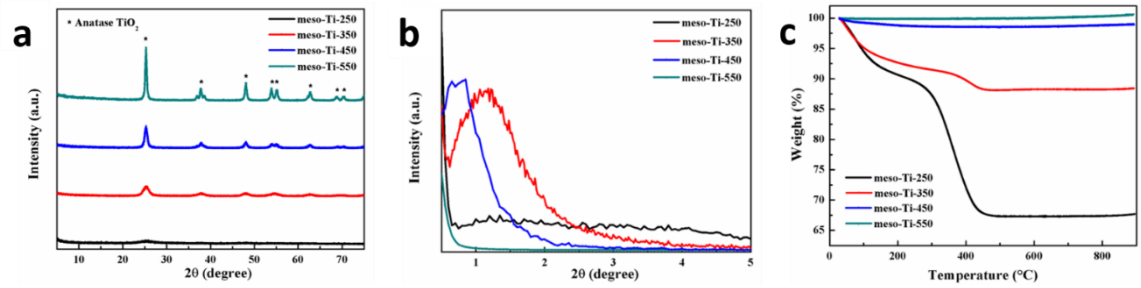

Figure 2.1 (a) Wide angle XRD patterns; (b) low angle XRD patterns; and (c) Thermogravimetric analysis profiles of meso-Ti-X (X = 250, 350, 450 and 550)

small. **Figure 2.1b** gives the low angle XRD patterns of titanium oxide materials. Meso-Ti-350 and meso-Ti-450 show a characteristic diffraction line in the low angle region, which reflects the existence of a mesoporous structure. Compared to meso-Ti-450, the low angle XRD diffraction line of meso-Ti-350 red shifted to a larger 2θ value, which can be explained by the particle size effect. According to the general trend in UCT materials, the pore expansion and particle size increase occurred when the heat treatment temperature increased. The lower angle position of the diffraction line for meso-Ti-450 indicated expanded pores and particles. When the heat treatment temperature was elevated above 450 °C, the low angle diffraction line was shifted to a lower angle. Meso-Ti-550 sample may preserve the mesoporous structure, but exceeds the detection limit of XRD. The mesoporous structure will be further confirmed by the N_2 sorption measurement. In order to examine the residue surfactant in each sample when different calcination temperatures are used, thermogravimetric analyses were performed. The meso-Ti-250 and meso-Ti-350 samples exhibit a total weight loss of 33% and 12%, respectively (**Figure 2.1c**). The TGA results show an incomplete removal of carboxyl and nitrate components in meso-Ti-250 and meso-Ti-350 samples. The existence of surfactant species and nitrate ions in residues will lead to a thermally unstable mesoporous structure,[27] while both meso-Ti-450 and meso-Ti-550 samples present high thermal stability. Therefore, the surfactant species can be totally removed during calcination treatment above 450 °C.

To further confirm the trends shown in the XRD patterns and TGA analysis results, N_2 sorption measurements were carried out. As shown in **Figure 2.2**, only meso-Ti-450 exhibits a Type-IV adsorption isotherm, which indicates the presence of a mesoporous structure. The meso-Ti-250 shows its structure with a high surface area of 266 m^2/g, which is possibly due to the existence of surfactant. Along with increasing calcination temperature, the meso-Ti-450 demonstrates a pore size expansion (0.08 cc/g) and a large surface area (83 m^2/g). **Figure 2.2c** shows a typical Type-IV N_2 sorption isotherm and BJH pore size distribution, suggesting a uniform mesoporous structure. Compared to meso-Ti-450, a drastic drop in surface area is observed for meso-Ti-550 samples. The loss of porosity at high treatment temperature confirms the tunable pore characteristics via heat treatments. Since only meso-Ti-450 exhibits good crystallinity, high

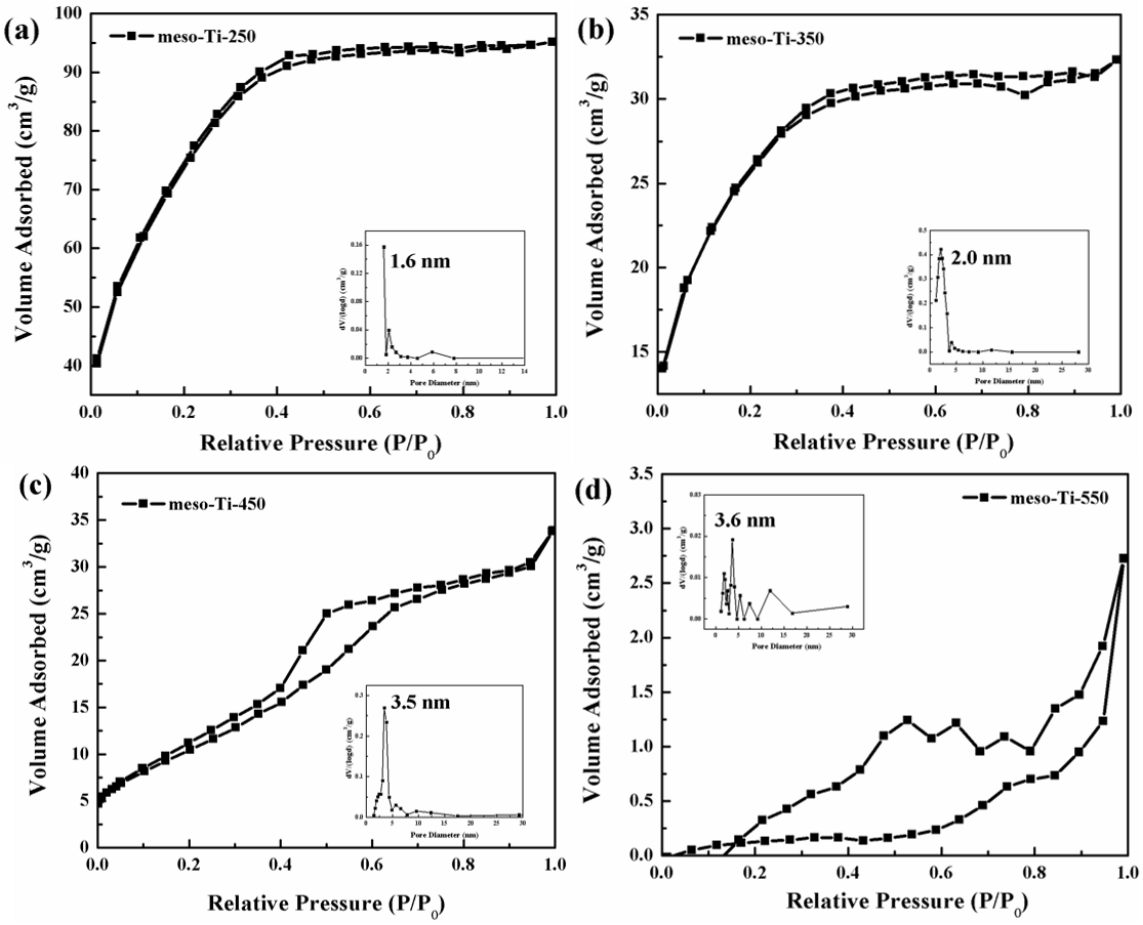

Figure 2.2 N_2 sorption isotherms of (a) meso-Ti-250, (b) meso-Ti-350, (c) meso-Ti-450, and (d) meso-Ti-550. Inset: BJH desorption pore size distributions of each sample.

---

thermal stability, and a mesoporous structure with characteristic type-IV adsorption isotherms, all the characterization and photocatalytic tests were performed with CQDs/meso-Ti-450 samples. The detailed BET multipoint surface area, BJH desorption pore size distribution and pore volume of meso-Ti-X (X = 250, 350, 450 and 550) are displayed in **Table 2.1**.

2.3.2 Preparation and Characterization of CQDs

Carbon quantum dots have been produced by many methods, such as electrochemical synthesis,[47]

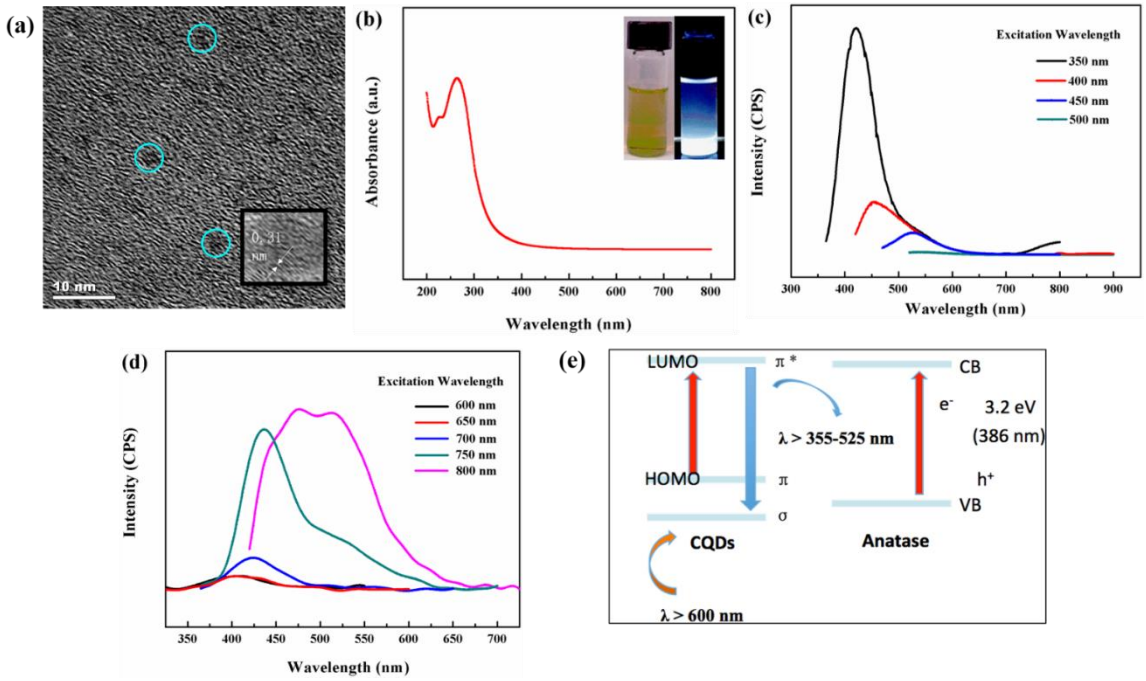

Figure 2.3 (a) TEM images of as-prepared CQDs. (b) UV-vis absorption spectrum of the CQDs in aqueous solution. Inset: CQDs dispersed in water illuminated under white light (left) and UV light (right). (c) Down converted PL spectra of CQDs. (d) Up-converted PL spectra of CQDs. (e) Schematic illustration of electronic transition of CQDs.

laser ablation,[48] reflux synthesis,[49] hydrothermal synthesis,[50] and microwave synthesis.[51] CQDs with unique fluorescent properties can be obtained by ultrasonic-hydrothermal treatment of L-ascorbic acid. This preparation method of CQDs has the merit of being environmentally friendly, facile, and lower cost than conventional preparation methods. The hydrothermal carbonization process required no strong acid, base, or organic solvent.

Figure 2.3a shows the TEM images of CQDs, which clearly express the well-dispersed nanoparticles with a near spherical-shaped morphology. The HRTEM image of the CQDs reveals the lattice spacing was around 0.32 nm, which corresponds to the (002) diffraction plane spacing of graphitic carbon. In the UV-vis spectra (**Figure 2.3b**), the ultrasonic-hydrothermal synthesized CQDs exhibit a strong absorption peak around 260 nm, which indicated the typical absorption of aromatic π systems. In addition, the as-prepared carbon quantum dots showed broad absorption in the visible light region, which represented the high photocatalytic activities under visible light. In the inset picture (**Figure 2.3b**, top right corner), two photographs of the CQDs aqueous solution under white light and UV light are shown. The bright blue fluorescence of CQDs is readily observed.

Photoluminescence is one of the most attractive features of carbon quantum dots. To further explore the optical properties of the CQDs in aqueous solution, photoluminescence studies were carried out by using different excitation wavelengths. As shown in **Figure 2.3c**, the PL spectra of carbon quantum dots are dependent on the excitation wavelength. When the excitation wavelength changes from 350 to 500 nm, the PL peaks shifted to a longer wavelength. The above result shows that the CQDs exhibit an excitation-dependent PL behavior. In addition to the strong down-conversion PL behavior, CQDs show a clear remarkable up-conversion property. **Figure 2.3d**

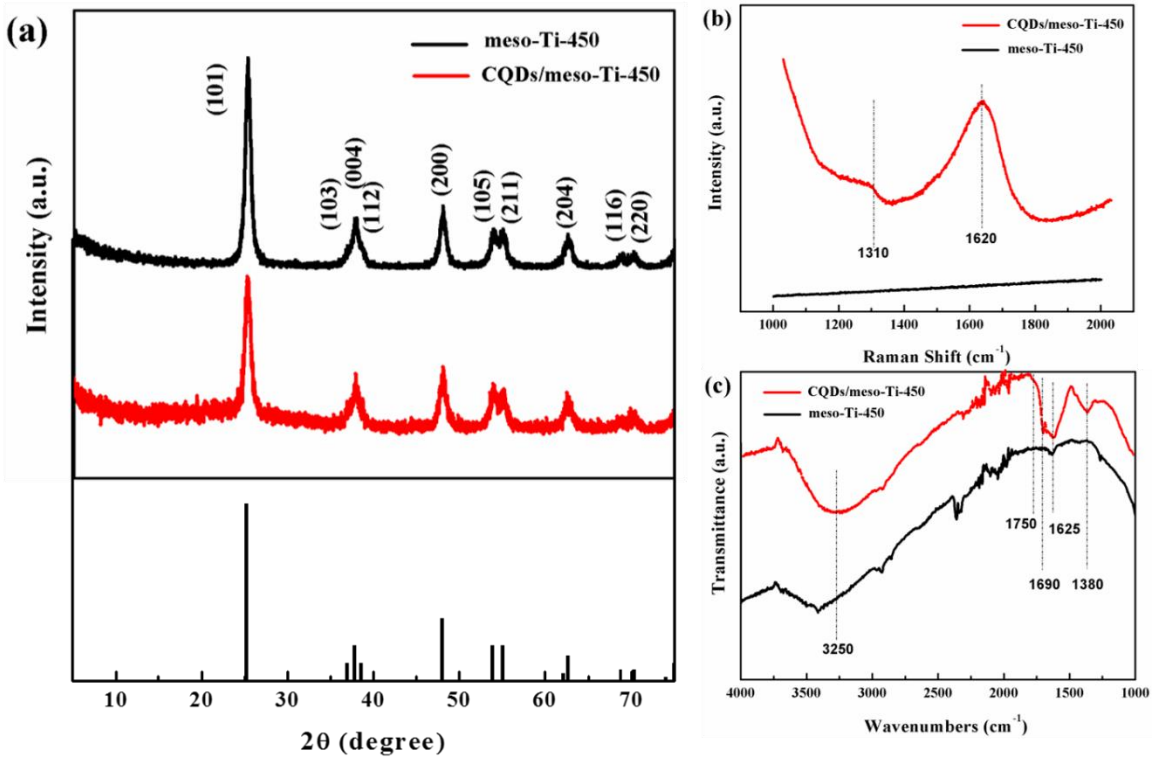

Figure 2.4 (a) XRD patterns of pure meso-Ti-450, CQDs/meso-Ti-450, and the JCPDS pattern for standard Anatase. (b) Raman spectra of CQDs and CQDs/meso-Ti-450. (c) FT-IR spectra of meso-Ti-450 and CQDs/meso-Ti-450.

shows the PL spectra of CQDs excited by long wavelength light. The up-conversion PL shows the excitation-dependent PL behavior, similar to the down-conversion PL spectra. Along with increasing excitation wavelengths at 550, 600, 650, 700, and 750 nm, the up-converted emission peaks show a red shift with stronger intensity (from 355 to 525 nm). According to the previous

Table 2.1 BET surface area, BJH desorption pore diameter and pore volume of meso-Ti-X (X=250, 350, 450 and 550) and CQDs/ meso-Ti-450 samples.

Sample	Surface Area (m^2/g)	Pore Size (nm)	Pore Volume (cc/g)
meso-Ti-250	266	1.6	0.166
meso-Ti-350	92	2.0	0.057
meso-Ti-450	83	3.5	0.08
meso-Ti-550	1	3.6	0.007

reports about CQDs, the up-conversion property of CQDs should be ascribed to a two-photon absorption process.[52,53] As illustrated in **Figure 2.3e**, when electrons in the π orbital are excited by

low-energy photons, the photo-generated electrons would move to the high-energy state. Then, the excited electrons can fall back to the σ orbital by radiative relaxation. Thus, a shorter wavelength light is emitted.[54]

2.3.3 Characterization of CQDs/ meso-Ti-450 Composites

Powder X-ray diffraction (XRD) was used to identify the phase of the products, crystal structure, and to determine the effect of CQDs on the crystallization of the TiO_2. **Figure 2.4a** shows the XRD pattern of meso-Ti-450, the CQDs/meso-Ti-450 composite material, and the Joint Committee on Powder Diffraction Standards (JCPDS) pattern for anatase titania (JCPDS card No. 00-021-1272) as well. The CQDs/meso-Ti-450 composite was obtained via a hydrothermal method to achieve the deposition of CQDs on meso-Ti-450. As shown in **Figure 2.4a**, CQDs/meso-Ti-450 composite shows the same characteristic diffraction lines of mesoporous TiO_2, which agree well with the standard pattern. Both materials display a pure anatase crystal structure. There is no additional carbon peak, which indicates the small amount and high dispersion of CQDs in CQDs/meso-Ti-450 composite.

Raman and Fourier Transform Infrared Spectroscopy (FT-IR) studies were used to determine the graphitic component structure of the as-prepared CQDs and to investigate the functional groups present on the surface of CQDs/meso-Ti-450, respectively. Raman spectra of CQDs and CQDs/meso-Ti-450 samples are shown in **Figure 2.4b**. The Raman spectrum of the CQDs sample

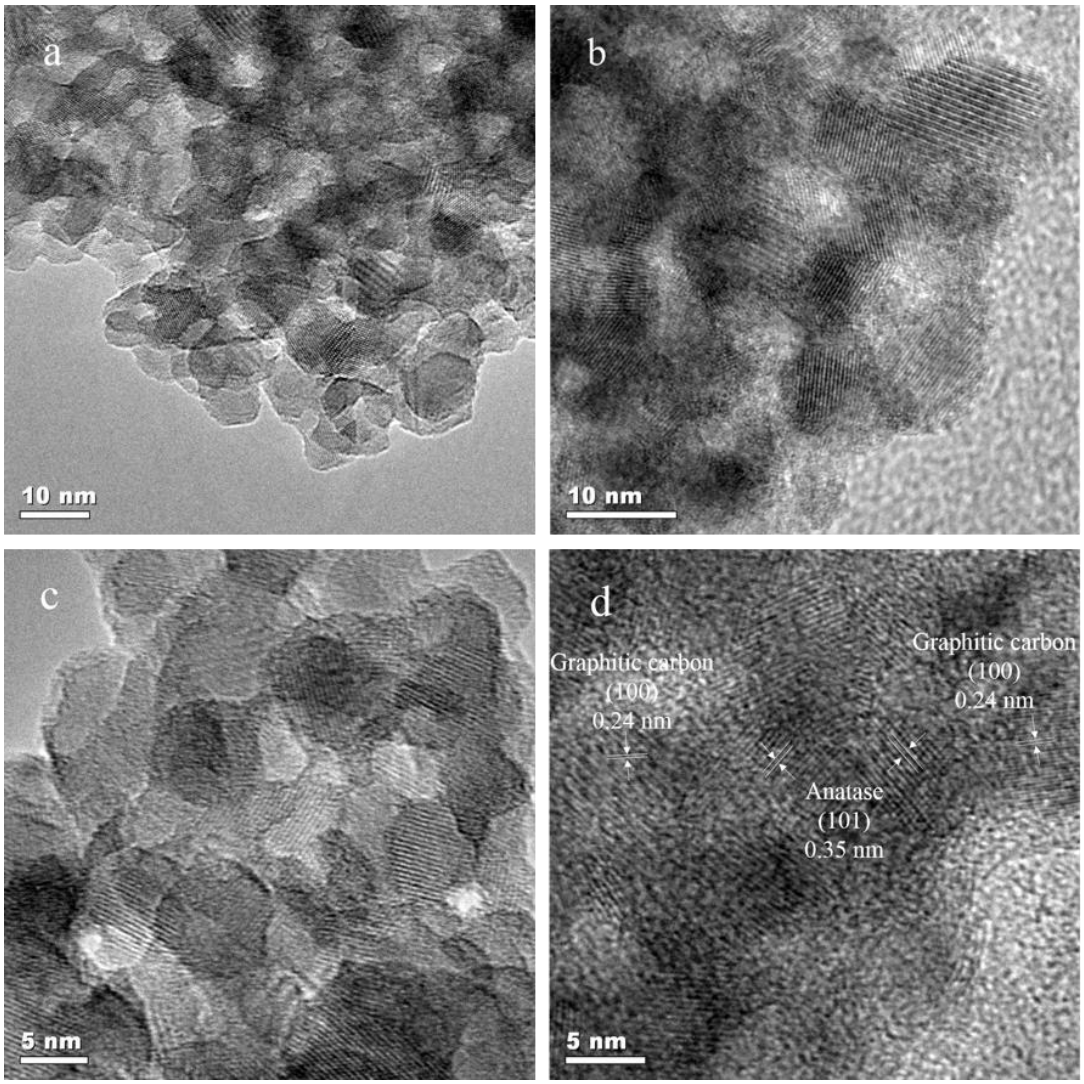

Figure 2.5 Low magnification HRTEM images of (a) meso-Ti-450, (b) CQDs/meso-Ti-450 composites, and high magnification HRTEM images of (c) meso-Ti-450, (d) CQDs/meso-Ti-450 composites.

shows no Raman signal under our measurement conditions, which is due to the strong fluorescence background of CQDs.[55] However, two bands at 1310 and 1620 cm^{-1} were detected for the CQDs/meso-Ti-450 sample, which can be attributed to the D and G bands of carbon, respectively. This observation indicates the strong fluorescence of CQDs in the CQDs/meso-Ti-450 composite quenched by TiO_2. The Raman spectra serve as further proof of a firm combination of CQDs with meso-Ti-450. The infrared spectra of meso-Ti-450 and CQDs/meso-Ti-450 are shown in **Figure 2.4b**. The band around 1625 cm^{-1} and the band over the range 3200-3600 cm^{-1} present in both meso-Ti-450 and CQDs/meso-Ti-450 composites are due to the presence of surface adsorbed water molecules. The absorption band around 1380 cm^{-1} is associated with the vibration of the C-O-C group. The band around 1690 cm^{-1} corresponds to the C=C stretch, while the band located at 1750 cm^{-1} indicates the presence of C=O groups.[2,5,44,51,55,56]

Since CQDs were not observed in the XRD pattern, TEM and HRTEM were carried out to further characterize the CQDs/meso-Ti-450 composites. **Figure 2.5a and b** were collected from the bare meso-Ti-450 prepared by a sol-gel method, while **Figure 2.5c and d** were collected from the 5% CQDs/meso-Ti-450. In **Figure 2.5a**, the domain exhibits relatively small nanoparticles with a mean size of 10 nm. The mesopores are evenly dispersed among particles. **Figure 2.5c** shows the high magnification HRTEM image of meso-Ti-450. They possess the anatase phase, with a lattice spacing of 0.35 nm, which agrees well with the (101) planes of the anatase phase. With the CQDs introduced into the system, the CQDs/meso-Ti-450 maintains a mesoporous structure. The mesoporosity of the composite materials was confirmed by N_2 sorption measurements (**Figure 2.6**) and low angle XRD (**Figure 2.1b**). As shown in **Figure 2.5b**, the composite materials also consist of an anatase phase with the CQDs deposited on the surface of TiO_2. In **Figure 2.5d**, the high magnification HRTEM image of CQDs/meso-Ti-450 shows the

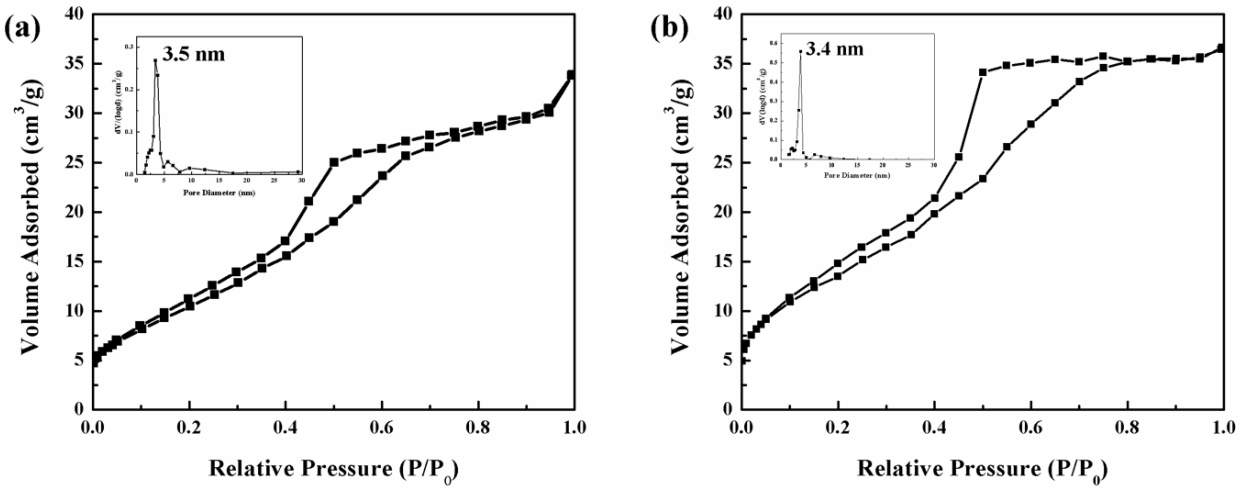

Figure 2.6 Nitrogen adsorption-desorption isotherms for (a) meso-Ti-450, (b) CQDs/meso-Ti-450, and the corresponding BJH desorption pore size distributions curve.

---

lattice spacing of 0.24 nm, corresponding to the (100) planes of graphitic carbon. The above results confirm the successful deposition of CQDs on the surface of meso-Ti-450 nanoparticles.

The surface area and pore size distribution of meso-Ti-450 and CQDs/meso-Ti-450 samples were determined by N_2 sorption measurements. **Figure 2.6** shows N_2 sorption isotherms along with the BJH pore size distributions. Meso-Ti-450 has a surface area of 83 m^2/g and CQDs/meso-Ti-450 has a surface area of 53 m^2/g. The decrease in surface area may indicate the adsorption of CQDs inside the mesopores. This might also be due to the partial loss of mesoporosity. As shown in **Figure 2.6a**, **b**, both isotherms show Type IV adsorption isotherms and a H_2-type hysteresis loop, according to the 1985 IUPAC classification,[58] which confirms the presence of regular capillary pores.[59] The BJH desorption pore size distributions are presented in the insets of **Figure 2.6**. The narrow pore size distributions were found to be 3.5 nm for meso-Ti-450 and 3.4 nm for CQDs/meso-Ti-450. The above results suggest the mesoporous structure was preserved with the

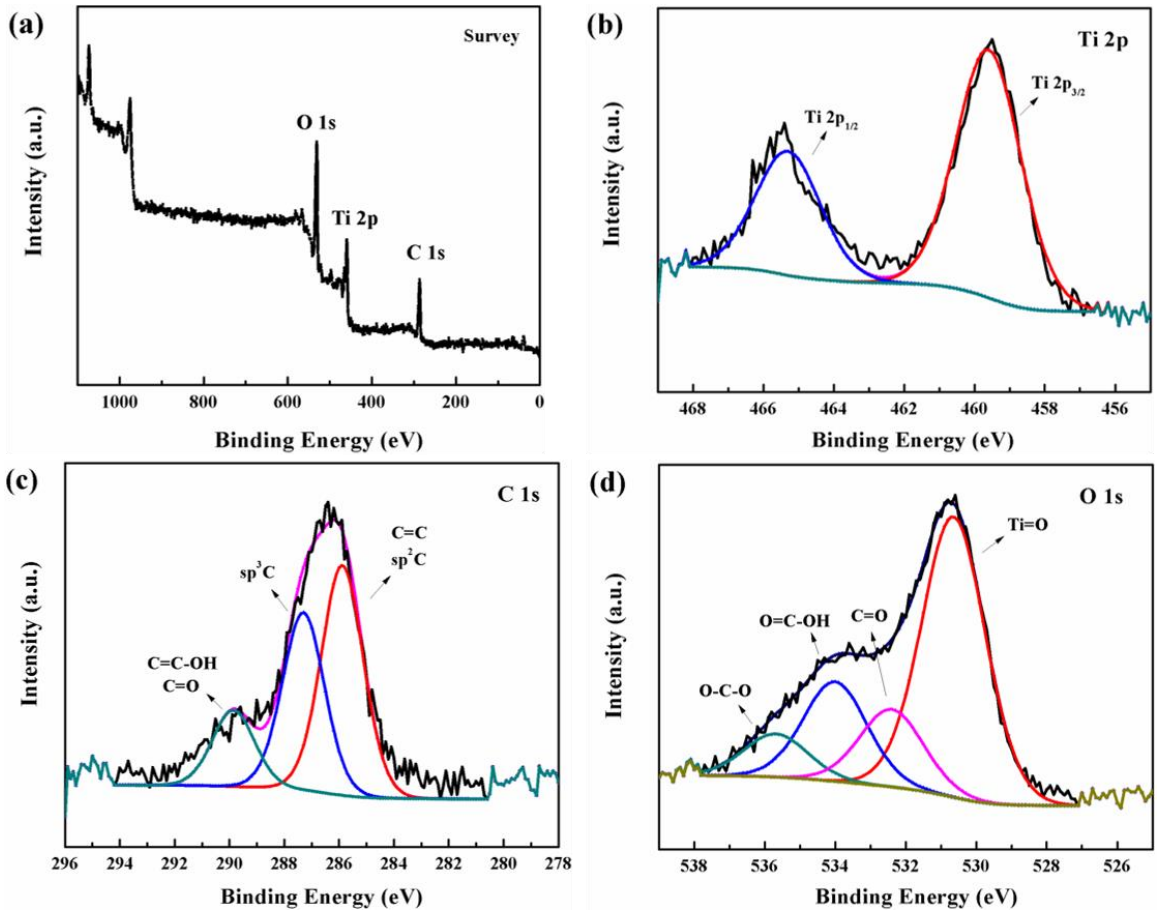

Figure 2.7 X-ray photoelectron spectroscopy (XPS) patterns for CQDs/meso-Ti-450 composite.

introduction of CQDs. The composite material exhibits an open mesoporous structure, which may provide more active sites for the adsorption of organic molecules.

XPS was used to investigate the chemical compositions and surface properties of the as prepared CQDs/meso-Ti-450 composite. **Figure 2.7** shows the full survey spectrum and narrow scan XPS patterns for the CQDs/meso-Ti-450 composite. The wide survey spectrum (**Figure 2.7a**) verified the existence of titanium (Ti 2p), carbon (C 1s), and oxygen (O 1s) in the CQDs/meso-Ti-450 composite. The Ti 2p spectrum (**Figure 2.7b**) was fitted to two peaks at 458.2 and 464.3 eV, which correspond to the $2p_{3/2}$ and $2p_{1/2}$, respectively. The spin energy separation of 6.1 eV was attributed to spin-orbital coupling. In the narrow scan of the C 1s (**Figure 2.7c**), the deconvoluted XPS peaks of the C 1s at 283.9, 286.0, and 288.4 eV were assigned to the sp^2 hybridized carbons, sp^3 hybridized carbons, C=O and C=C-OH, respectively. The expanded pattern of O 1s is shown in **Figure 2.7d**. The broad peak was deconvoluted into four peaks. The peaks at 528.9, 530.8, 532.5, and 534.2 eV are ascribed to Ti=O, C=O, O=C-OH, and O-C-O, respectively.[2,45,60] Both the C 1s and O 1s XPS patterns show the presence of carbon-oxygen bonds in CQDs/meso-Ti-450 composites, which agrees well with the FT-IR spectroscopy results (**Figure 2.5b**) indicating the presence of surface passivation groups on the surface of as-prepared CQDs/meso-Ti-450.

2.3.4 Photocatalytic Dye Degradation under Visible Light Irradiation

For a photocatalyst, the absorption range of sunlight plays a crucial role in the photoinduced dye degradation. In order to study the relationship between light absorption range and CQDs introduction into the meso-Ti-450, diffuse reflectance spectra (DRS) measurements of the CQDs/meso-Ti-450 composite were carried out. Pure anatase phase has a larger band gap (3.2 eV), which makes the material more transparent in the visible light region, and hence exhibits lower

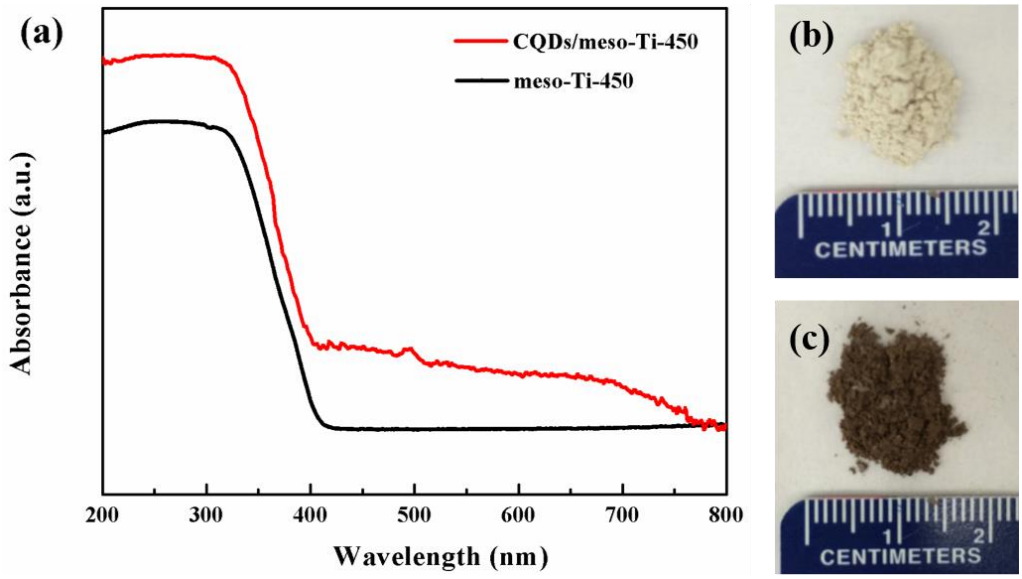

Figure 2.8 (a) DR UV-vis spectra for meso-Ti-450 and CQDs/meso-Ti-450 samples. (b) Photo for Meso-Ti-450. (c) Photo for CQDs/meso-Ti-450.

photocatalytic activity under visible light irradiation.[61] As shown in **Figure 2.8a**, meso-Ti-450 shows no absorption in the visible region of 410-800 nm, which agrees well with the absorption ability of mesoporous TiO_2. **Figure 2.8b and 2.8c** present the color changes of TiO_2 before and after addition of CQDs. The CQDs/meso-Ti-450 composite powder shows a brownish color, which indicates its ability to absorb visible light. Compared to the bare meso-Ti-450, CQDs/meso-Ti-450 exhibits an obvious red shift, and remarkable absorption in the visible light region. The result demonstrated that the CQDs/meso-Ti-450 composites may exhibit a narrowed band gap compared to that of meso-Ti-450 due to the addition of CQDs. As a result of the extended absorption range, the photocatalytic ability of CQDs/meso-Ti-450 showed a great enhancement, due to a better utilization of visible light. To value the synergistic effect between CQDs and mesoporous TiO_2, the CQDs modified P25 material is prepared for comparison. Compared to the obvious extended

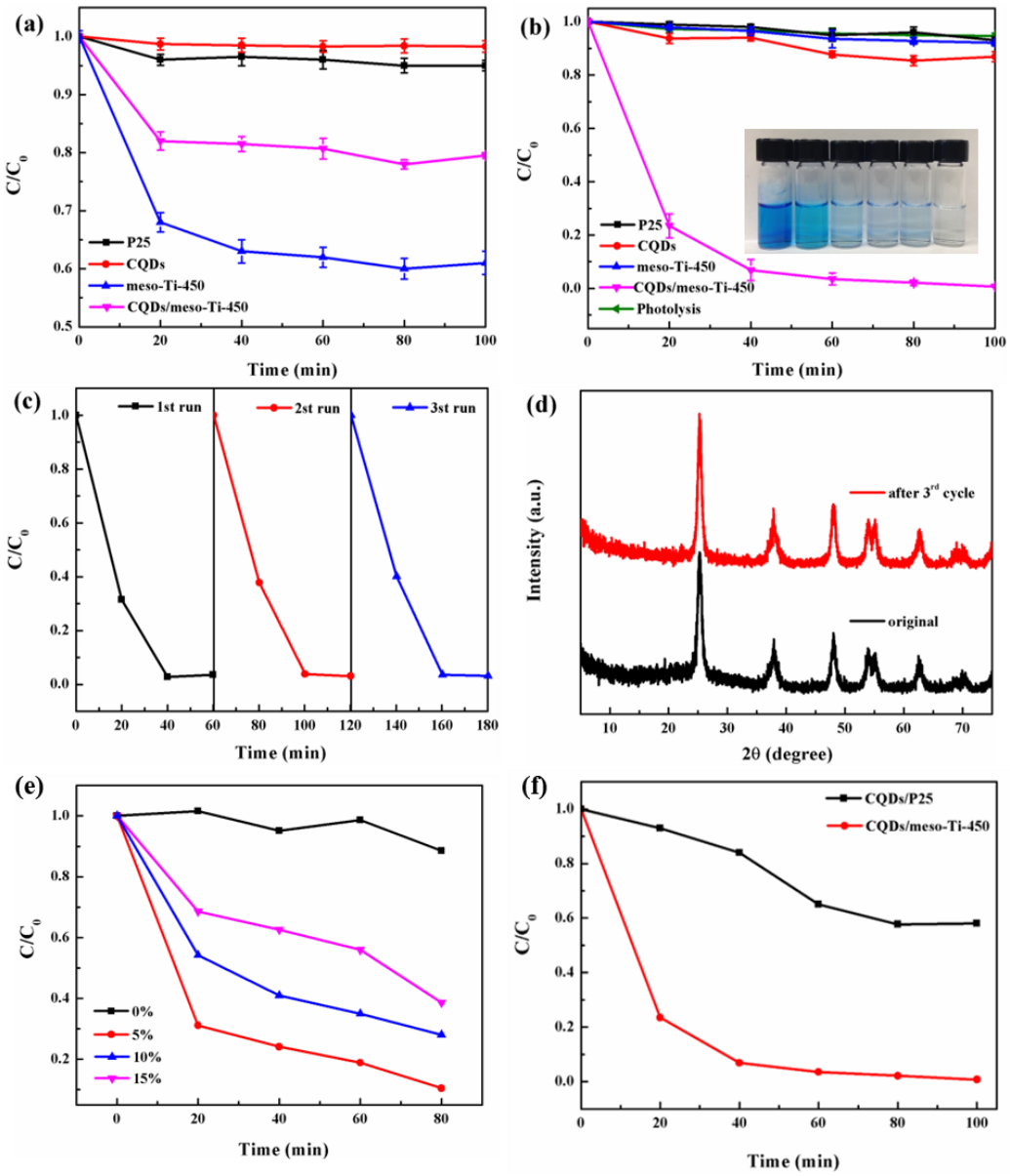

Figure 2.9 (a) Adsorption efficiency tests for P25, CQDs, meso-Ti-450, and CQDs/meso-Ti-450 by dispersing 50 mg each sample in 50 mL, 1×10^{-4} M MB dye aqueous solution under dark conditions. (b) Photocatalytic degradation of 50 mL, 1×10^{-4} M MB dye aqueous solution under visible light in 100 min by using 50 mg of P25, CQDs, meso-Ti-450, CQDs/meso-Ti-450, and blank control without any photocatalyst (photolysis), respectively. Inset: Color change of MB solution under visible light irradiation in the presence of CQDs/meso-Ti-450 corresponding to different times of 20, 40, 60, 80, 100 min. (c) Recycle performance test of CQDs/meso-Ti-450 sample. (d) Wide angle XRD patterns of CQDs/meso-Ti-450 sample before and after recycle performance test. (e) Photocatalytic degradation efficiency of CQDs/meso-Ti-450 composites with different CQDs loading amount 0%, 5%, 10%, and 15%, respectively. (f) Photocatalytic degradation of 50 mL, 1×10^{-4} M MB dye aqueous solution under visible light in 100 min by using 50 mg of CQDs/P25, and CQDs/meso-Ti-450, respectively. Visible light was turned on after 100 min adsorption under dark conditions.

absorption range of CQDs/meso-Ti-450, the absorption range of P25 barely shows an extension after the addition of CQDs, which is probably due to the nonporous nature of P25. In order to further confirm the synergistic effect, CQDs modified P25 has been prepared and used as photocatalyst in the degradation of MB. Compared to the CQDs/meso-Ti-450, CQDs/P25 exhibits less dye adsorption capacity within 1 h adsorption in the dark. When we transferred the dye solution contained CQDs/P25 photocatalyst into a photochemical reactor for dye degradation tests, there was about 40 % degradation of MB observed by CQDs/P25 photocatalysts (**Figure 2.9f**).

The photocatalytic activity of as-prepared CQDs/meso-Ti-450 composites was studied via photocatalytic degradation of Methylene Blue (MB) under visible light irradiation. Prior to the dye degradation studies, the adsorption ability tests were carried out under dark conditions. P25 and CQDs barely show adsorption ability, while meso-Ti-450 and CQDs/meso-Ti-450 composites exhibit fair adsorption capacities. Compared to CQDs/meso-Ti-450 composites, the adsorption efficiency of meso-Ti-450 is higher (**Figure 2.9a**). The relatively low adsorption capacity of CQDs/meso-Ti-450 composites is due to the contracted pore size as the CQDs are filling inside the mesopores. The results are well in accordance with the N_2 sorption results (**Figure 2.6**). When visible light and a very high starting concentration of methylene blue were used (32 mg/L), the CQDs/meso-Ti-450 exhibited excellent photocatalytic efficiency. The relationship between concentration of MB solution and visible light irradiation time is shown in **Figure 2.9b**. As can be seen, the photo-induced dye degradation efficiency is up to 98% in 1 h with as-prepared CQDs/meso-Ti-450 as the photocatalyst. For comparison, commercial P25, pure meso-Ti-450, and pure CQDs aqueous solution were used as photocatalysts in the contrast experiments. There is less than 5% degradation of MB observed, which confirmed the enhanced visible light response of CQDs modified mesoporous TiO_2. The remarkable photocatalytic activity of CQDs/meso-Ti-450 can be ascribed to the interaction between CQDs and meso-Ti-450. **Figure 2.9b inset** displays the color change of methylene blue solution before and after the photocatalytic test. Before the start

of irradiation, the methylene blue solution containing the photocatalyst was placed under dark conditions for 2 h to reach adsorption-desorption equilibria. As shown in **Figure 2.9b inset,** there is a vague color change from deep blue to light blue, which indicated the adsorption ability of CQDs/meso-Ti-450. After the visible light was turned on, the methylene blue solution was changed from light blue to a colorless solution within 80 min under ambient conditions. The dye degradation mechanism was further investigated by intermediate analysis using Electrospray Ionization Mass Spectrometry and CO_2 evolution. In order to test the recycling ability and stability of CQDs/meso-Ti-450, the photocatalyst was collected after degradation reaction, and washed by deionized water. Then the sample was dried at 100 °C in an oven overnight. The recovered photocatalyst was used for recycle tests. **Figure 2.9c** shows the photocatalytic performance of CQDs/meso-Ti-450 for three cycles in dye degradation tests. The photocatalyst exhibits repeatable catalytic activity during three cycles with only a slight decrease. In the wide angle XRD patterns of CQDs/meso-Ti-450 sample before and after three cycles, no obvious change in characteristic lines was observed (**Figure 2.9d**). The above results demonstrated the good recyclability and stability of the composite material.

To further explore the photocatalytic activity of the CQDs modified meso-Ti-450, the effect of loading amount of CQDs was investigated. Notably, the loading amount of CQDs in the present system can largely affect the dye degradation efficiency. As shown in **Figure 2.9e**, the photocatalytic degradation efficiency is the highest (about 90% degradation in 40 min) when 5% (weight percent) CQDs was added into the system. However, further increasing the loading amount of CQDs decreases the dye degradation efficiency to 60%. This indicates that the capacity of mesopores on the surface of meso-Ti-450 correlates with the loading amount of CQDs. The excessive CQDs can impede the reaction of photo-generated electrons and holes with surface adsorbed oxidants and reducers[62]. Another factor to consider is the inner filter effect, which occurred due to a high concentration of fluorescent molecules, CQDs in this case. In the presence

of highly concentrated CQDs, the excitation energy or emission energy will be absorbed by CQDs themselves and resulted in lower energy reached onto the CQDs/meso-Ti-450 composite. The results indicate that the proper control of the quantity of the absorbing fluorophore molecules is important to the photocatalytic activity.

In order to better understand the photocatalytic mechanism of CQDs modified mesoporous TiO_2, 5% CQDs/meso-Ti-450 was used as a photocatalyst in the degradation of colorless aromatic pollutants. N-Benzylideneaniline was chosen as a target organic molecule, because of its zero absorbance under visible light. Prior to the degradation study, the adsorption ability was first investigated. Fifty mg of catalyst dispersed in 50 mL of 20 ppm N-Benzylideneaniline aqueous solution was applied in dark conditions for 1 h. The halogen lamp was turned on when the solution achieved adsorption equilibrium. As a result, 30% of N-Benzylideneaniline was degraded after 2 h. CQDs/meso-Ti-450 material not only can be used for dye degradation but also for colorless organic pollutants. Thus, we can conclude that the as-prepared photocatalyst can be excited by visible light without the presence of dye molecules. In other word, the dye-sensitized semiconductor mechanism can be excluded.

2.4 Discussion

In this study, the mesoporous TiO_2 was synthesized by a recently developed inverse micelle sol-gel method.[27] This approach involves sol-gel reactions of the transition metal oxo-clusters with surfactant species in hydrated inverse micelle nanoreactors. The reaction was controlled by the unique thermal decomposition of nitrate ions. The formed NO_x species are attached to metal oxo-clusters, followed by an increased acidity and the formation of mesoporous metal oxides.[63] The formed mesostructure of the meso-Ti-450 sample was confirmed by the N_2 sorption measurements (**Figure 2.2c**), which showed typical Type IV adsorption isotherms. To further decorate the mesoporous TiO_2, mono-dispersed CQDs were added into the system. In comparison with

mesoporous TiO_2, the CQDs modified meso-TiO_2 exhibits a decreased surface area and smaller pore size, which contributed to the CQDs being embedded into the mesopores and probably partial loss of mesoporosity. However, the presence of aromatic rings and oxygen containing groups of CQDs may contribute to the adsorption toward methylene blue and N-Benzylideneaniline molecules on the photocatalyst composite via π-π conjugation. This process facilitates the photo-induced degradation of the adsorbed target molecules. The CQDs were prepared by an ultrasonic-hydrothermal method. The ultrasonic waves lead to aromatization of L-ascorbic acid followed by carbonization under hydrothermal treatment.[64,65] In order to explore the surface functional groups, the Raman spectrum of CQDs/meso-TiO_2 was collected. A weak D band and a strong G band were observed in the spectrum (**Figure 2.4b**). As the intensity ratio of the D and G bands is an indicator of the disordered content of carbon and the ratio of the sp^3/sp^2 carbon components, abundant oxygenated sp^2 carbon groups are mainly occupied at the surface of the CQDs/meso-TiO_2 composite. The surface properties were further confirmed by XPS, which suggested the presence of surface hydroxyl and carboxyl groups (**Figure 2.7c**). Other evidence related to the surface carbon components of the composite material involves the HRTEM images of as-prepared CQDs modified mesoporous TiO_2. As shown in **Figure 2.5d**, the area exhibits relatively small particles embedded in the mesopores or attached on the surface of TiO_2. The small particles display a lattice spacing of 0.24 nm, which can be assigned to the (100) planes of the graphitic carbon. Based on the above results, the close contact between CQDs and mesoporous TiO_2 could be an advantage for the electron transfer process, thus the enhanced photocatalytic activity.

The adsorption capacity and photocatalytic performance of CQDs/meso-Ti-450 was investigated by dye degradation of MB under dark condition and visible light irradiation, respectively (**Figure 2.8a** and **b**). The efficiency of photocatalysts is affected by various factors. In this study, both the mesoporous structure of CQDs/meso-Ti-450 and introduction of carbon quantum dots greatly contribute to the enhanced dye degradation efficiency. The unique mesoporous structure

contributes a great deal to the photocatalytic activity of as-prepared materials. Since small organic molecules can be adsorbed into the pores more efficiently, adsorption is considered as a prerequisite for good photo-induced dye degradation activity.[19] In this reaction protocol, the mesoporous structure of TiO_2 acts as a substrate for CQDs nanoparticles. The open mesoporous structure and large surface area produced more active sites, which can facilitate the interaction between CQDs and mesoporous TiO_2.[2] Thus, CQDs can act as active sites for adsorption of target molecules via the strong π-π conjugation. To confirm the important role of mesoporous TiO_2 in photocatalysis, CQDs modified nonporous commercial P25 is synthesized for comparison. However, compared to CQDs/meso-Ti-450, introduction of CQDs does not greatly alter the absorption band of P25. The corresponding dye degradation performance of CQDs/P25 is in accordance with the DRS results. Compared to CQDs/P25, the CQDs/meso-TiO_2 composite photocatalyst showed much higher degradation ability toward the MB dye (**Figure 2.9f**). Therefore, the mesoporous structure may play an important role in the high photocatalytic activity of the

Scheme 2.1 Mechanism of the photocatalytic process for CQDs/meso-Ti-450 under visible light irradiation

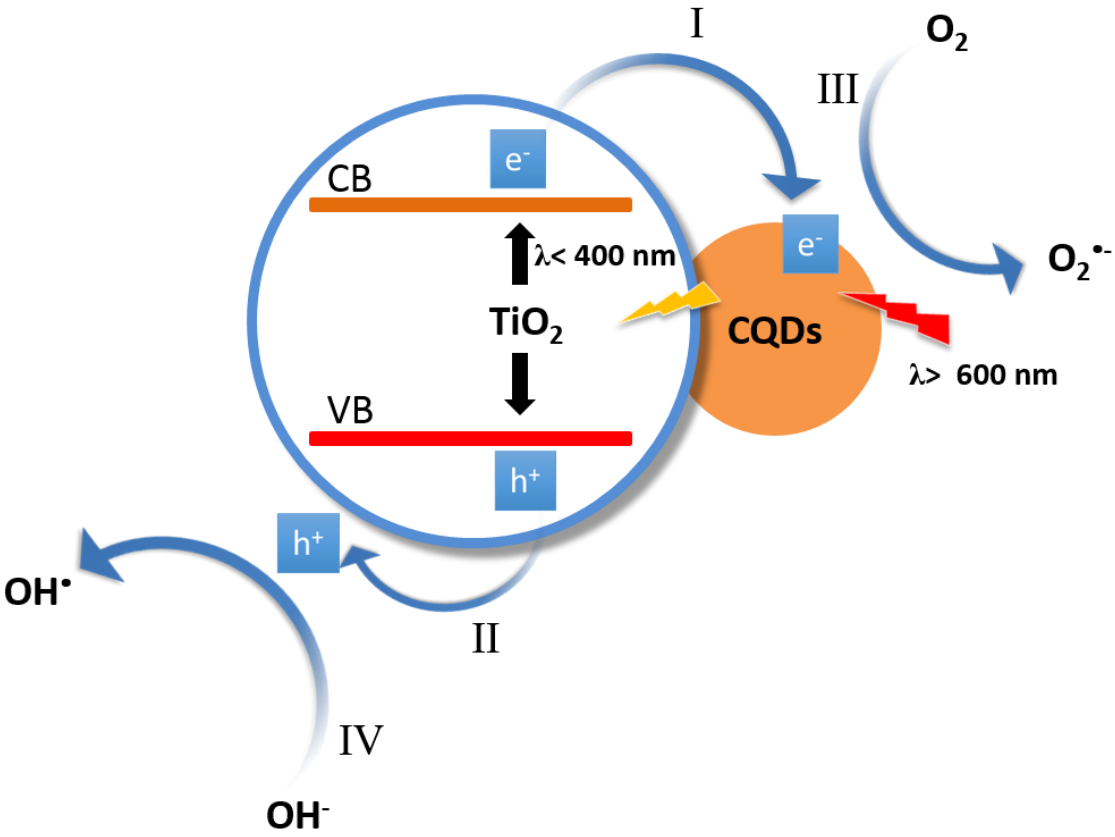

composite material. However, in this photocatalytic system, the CQDs modified meso-Ti-450 has lower adsorption efficiency than that of unmodified meso-Ti-450. The optical properties of CQDs are other key reasons for the high photocatalytic activity.

CQDs have an attractive up-conversion photoluminescence property (**Figure 2.3d**) in addition to the normal down-conversion photoluminescence. In a typical up-conversion fluorescence process, the emission photon energy is higher than that of the excitation. The possible mechanism is a multiple photon process.[45,66,67] Due to this unique property, CQDs can act as efficient energy converters. The CQDs first absorbed long-wavelength light (λ > 600 nm), followed by shorter wavelength light emission located in the range of UV light, which further excites TiO_2 to produce photogenerated electrons and holes (**Scheme 2.1**). In addition, CQDs existed as efficient electron reservoirs, which can trap electrons emitted from the conduction band of TiO_2.[68] Thus, the electrons in the TiO_2 conduction band will transfer to the CQDs (process I), to further react with molecular oxygen to produce superoxide anion radicals ($O_2^{\bullet -}$) (process III). Meanwhile, the photogenerated holes in the valence band will migrate to the surface of TiO_2 (process II), and then react with hydroxyl species to form active hydroxyl radicals ($OH^{\bullet}$) (process IV).[7,11,69] Similar to the mechanism reported in the literature, those highly active radicals exhibit remarkable oxidizing ability to organic molecules adsorbed on the surface of TiO_2. Based on the proposed mechanism, the presence of CQDs can hinder the electron-hole recombination, and improve the photocatalytic efficiency. To confirm the role of CQDs as an electron scavenger, photocatalytic degradation of MB was conducted in a N_2 atmosphere. Since oxygen can work as a potential electron acceptor, we removed dissolved oxygen by purging with N_2 during the measurements.[70] Compared to mesoporous TiO_2, the CQDs modified TiO_2 exhibits higher degradation efficiency. This suggests CQDs prohibits the recombination process of photogenerated electrons and holes, by facilitating electrons migrating from the conduction band of TiO_2 to CQDs on the surface. However, N_2 saturation leads to a decreased photocatalytic efficiency overall, in comparison with the same

photocatalytic reaction under ambient conditions. As shown in **Figure 2.8b**, the MB dye can be mostly decomposed (98%) in the presence of CQDs/meso-Ti-450 in 1 h under visible light irradiation. The dye degradation performance is much superior to that of commercial P25 and unmodified meso-Ti-450.

Methylene blue dye molecules can work as photosensitizers to produce electrons, which are injected to the conduction band of TiO_2.[71,72] In the present study, the colorless organic molecule, N-Benzylideneaniline, can also be partially degraded by the composite photocatalyst. We may exclude the dye sensitization mechanism and prove that the CQDs modified mesoporous TiO_2 can be excited by visible light without the presence of a dye. This agrees well with our proposed mechanism. In this study, the CQDs modified meso-Ti-450 shows much higher photocatalytic activity under visible light under ambient conditions.

2.5 Conclusions

In summary, CQDs embedded mesoporous TiO_2 composites were first successfully synthesized by a low cost, environmentally friendly sol-gel and ultrasonic-hydrothermal method. The mesoporous structure was preserved with the introduction of CQDs. The photocatalytic activity was investigated using methylene blue degradation under visible light irradiation. Compared to commercial Degussa P25, pure mesoporous TiO_2, and CQDs/P25, CQDs/meso-Ti-450 composites showed enhanced catalytic performance. The optimized composite (5% CQDs-meso-Ti-450) possessed a surface area of 53 m^2/g and a pore size of 3.4 nm. The composite exhibits the highest visible light induced photocatalytic activity toward methylene blue dye (up to 98% degradation efficiency in 1 h). Photocatalytic activity of 5% CQDs-meso-Ti-450 was also investigated by N-Benzylideneaniline degradation under visible light irradiation, 30% degradation efficiency was achieved in 2 h. The mesoporous structure of TiO_2 offers more active sites for efficient adsorption

of target organic molecules. Meanwhile, the up-conversion property and electron acceptor property of CQDs facilitate the usage of visible light and hinder the electron/hole recombination process, respectively. The synergistic effects of optical properties of CQDs and mesoporosity of TiO_2 lead to a remarkable visible light responsive photocatalyst. The CQDs/meso-Ti-450 composite has great potential as an environmentally friendly catalyst in visible light induced photocatalysis.

2.6 References

(1) Zu, G.; Shen, J.; Wang, W.; Zou, L.; Lian, Y.; Zhang, Z. *ACS Appl. Mater. Interfaces* **2015**, *7*, 5400–5409.

(2) Yu, B. Y.; Kwak, S.-Y. *J. Mater. Chem.* **2012**, *22*, 8345–8353.

(3) Zhang, Y.; Jin, L.; Sterling, K.; Luo, Z.; Jiang, T.; Miao, R.; Guild, C.; Suib, S. L. *Green Chem.* **2015**, *17* (6), 3600–3608.

(4) Sun, L.; Wu, W.; Yang, S.; Zhou, J.; Hong, M.; Xiao, X.; Ren, F.; Jiang, C. *ACS Appl. Mater. Interfaces* **2014**, *6*, 1113–1124.

(5) Li, H.; Liu, R.; Liu, Y.; Huang, H.; Yu, H.; Ming, H.; Lian, S.; Lee, S.-T.; Kang, Z. *J. Mater. Chem.* **2012**, *22*, 17470–17475.

(6) Xu, L.; Hu, Y. L.; Pelligra, C.; Chen, C. H.; Jin, L.; Huang, H.; Sithambaram, S.; Aindow, M.; Joesten, R.; Suib, S. L. *Chem. Mater.* **2009**, *21*, 2875–2885.

(7) Nakata, K.; Fujishima, A. *J. Photochem. Photobiol. C Photochem. Rev.* **2012**, *13*, 169–189.

(8) Macak, J. M.; Zlamal, M.; Krysa, J.; Schmuki, P. *Small* **2007**, *3*, 300–304.

(9) Liu, S.; Yu, J.; Jaroniec, M. *J. Am. Chem. Soc.* **2010**, *132*, 11914–11916.

(10) Kumar, S. G.; Devi, L. G. *J. Phys. Chem. A* **2011**, *115*, 13211–13241.

(11) Genuino, H. C.; Hamal, D. B.; Fu, Y.; Suib, S. L. *J. Phys. Chem. C* **2012**, *116*, 14040–14051.

(12) Jafry, H. R.; Liga, M. V; Li, Q.; Barron, A. R. *Environ. Sci. Technol.* **2011**, *45*, 1563–1568.

(13) Zhang, H.; Lv, X.; Li, Y.; Wang, Y.; Li, J. *ACS Nano* **2010**, *4*, 380–386.

(14) Hurum, D. C.; Agrios, A. G.; Gray, K. A.; Rajh, T.; Thurnauer, M. C. *J. Phys. Chem. B*

2003, *107*, 4545–4549.

(15) Scanlon, D. O.; Dunnill, C. W.; Buckeridge, J.; Shevlin, S. a; Logsdail, A. J.; Woodley, S. M.; Catlow, C. R. a; Powell, M. J.; Palgrave, R. G.; Parkin, I. P.; Watson, G. W.; Keal, T. W.; Sherwood, P.; Walsh, A.; Sokol, A. a. *Nat. Mater.* **2013**, *12*, 798–801.

(16) Sakthivel, S.; Kisch, H. *Angew. Chem. Int. Ed. Engl.* **2003**, *42*, 4908–4911.

(17) Ren, W.; Ai, Z.; Jia, F.; Zhang, L.; Fan, X.; Zou, Z. *Appl. Catal. B Environ.* **2007**, *69*, 138–144.

(18) Chen, X.; Burda, C. *J. Am. Chem. Soc.* **2008**, *130*, 5018–5019.

(19) Luo, Z.; Poyraz, A. S.; Kuo, C.; Miao, R.; Meng, Y.; Chen, S.; Jiang, T.; Wenos, C.; Suib, S. L. *Chem. Mater.* **2015**, *27*, 6–17.

(20) Zhuo, S.; Shao, M.; Lee, S.-T. *ACS Nano* **2012**, *6*, 1059–1064.

(21) Li, W.; Wu, Z.; Wang, J.; Elzatahry, A. A.; Zhao, D. *Chem. Mater.* **2014**, *26*, 287–298.

(22) Jiang, T.; Du, S.; Jafari, T.; Zhong, W.; Sun, Y.; Song, W.; Luo, Z.; Hines, W. a.; Suib, S. L. *Appl. Catal. A Gen.* **2015**, *502*, 105–113.

(23) Bao, N.; Li, Y.; Wei, Z.; Yin, G.; Niu, J. *J. Phys. Chem. C* **2011**, *115*, 5708–5719.

(24) Li, H.; Bian, Z.; Zhu, J.; Huo, Y.; Li, H.; Lu, Y. *J. Am. Chem. Soc.* **2007**, *129*, 4538–4539.

(25) Feng, Y.; Li, L.; Ge, M.; Guo, C.; Wang, J.; Liu, L. *ACS Appl. Mater. Interfaces* **2010**, *2*, 3134–3140.

(26) Zhu, T.; Li, J.; Wu, Q. *ACS Appl. Mater. Interfaces* **2011**, *3*, 3448–3453.

(27) Poyraz, A. S.; Kuo, C.; Biswas, S.; Suib, S. L. *Nat. Commun.* **2013**, *4*, 2952–2961.

(28) Jiang, T.; Poyraz, A. S.; Iyer, A.; Zhang, Y.; Luo, Z.; Zhong, W.; Miao, R.; El-Sawy, A. M.; Guild, C. J.; Sun, Y.; Kriz, D. a.; Suib, S. L. *J. Phys. Chem. C* **2015**, *119*, 10454–10468.

(29) Kuo, C.-H.; Mosa, I. M.; Poyraz, A. S.; Biswas, S.; El-Sawy, A. M.; Song, W.; Luo, Z.; Chen, S.-Y.; Rusling, J. F.; He, J.; Suib, S. L. *ACS Catal.* **2015**, *5*, 1693–1699.

(30) Wasalathanthri, N. D.; Poyraz, A. S.; Biswas, S.; Meng, Y.; Kuo, C.-H.; Kriz, D. a.; Suib, S. L. *J. Phys. Chem. C* **2015**, *119*, 1473–1482.

(31) Song, W.; Poyraz, A. S.; Meng, Y.; Ren, Z.; Chen, S.; Suib, S. L. *Chem. Mater.* **2014**, *26*, 4629–4639.

(32) Yao, Y.; Li, G.; Ciston, S.; Lueptow, R. M. *Environ. Sci. Technol.* **2008**, *42*, 4952–4957.

(33) Zhang, L.-W.; Fu, H.-B.; Zhu, Y.-F. *Adv. Funct. Mater.* **2008**, *18*, 2180–2189.

(34) Kong, S.; Jin, Z.; Liu, H.; Wang, Y. *J. Phys. Chem. C* **2014**, *118*, 25355–25364.

(35) Zhang, P.; Rogelj, S.; Nguyen, K.; Wheeler, D. *J. Am. Chem. Soc.* **2006**, *128* (38), 12410–12411.

(36) Boyer, J.; Vetrone, F.; Cuccia, L. A.; Capobianco, J. A.; Hb, Q. C.; National, I.; Recherche, D. *J Am Chem Soc* **2006**, *128*, 7444–7445.

(37) Boyer, J.; Cuccia, L. A.; Capobianco, J. A. *Nano Lett.* **2007**, *7*, 847–852.

(38) Chen, Z.; Chen, H.; Hu, H.; Yu, M.; Li, F.; Zhang, Q.; Zhou, Z.; Yi, T.; Huang, C. *J Am Chem Soc* **2008**, *130* (6), 3023–3029.

(39) Han, Y.; Huang, H.; Zhang, H.; Liu, Y.; Han, X.; Liu, R.; Li, H.; Kang, Z. *ACS Catal.* **2014**, *4*, 781–787.

(40) Li, H.; Kang, Z.; Liu, Y.; Lee, S.-T. *J. Mater. Chem.* **2012**, *22*, 24230–24253.

(41) Michalet, X.; Pinaud, F. F.; Bentolila, L. a; Tsay, J. M.; Doose, S.; Li, J. J.; Sundaresan, G.; Wu, a M.; Gambhir, S. S.; Weiss, S. *Science* **2005**, *307*, 538–544.

(42) Xu, H.; Miao, R.; Fang, Z.; Zhong, X. *Anal. Chim. Acta* **2011**, *687* (1), 82–88.

(43) Sun, Y.; Zhou, B.; Lin, Y.; Wang, W.; Fernando, K. A. S.; Pathak, P.; Meziani, M. J.; Harruff, B. A.; Wang, X.; Wang, H.; Luo, P. G.; Yang, H.; Kose, M. E.; Chen, B.; Veca, L. M.; Xie, S.; Carolina, S. *J. Am. Chem. Soc.* **2006**, *128*, 7756–7757.

(44) Yu, P.; Wen, X.; Toh, Y.-R.; Tang, J. *J. Phys. Chem. C* **2012**, *116*, 25552–25557.

(45) Yu, X.; Liu, J.; Yu, Y.; Zuo, S.; Li, B. *Carbon N. Y.* **2014**, *68*, 718–724.

(46) Zhu, Y.; Ji, X.; Pan, C.; Sun, Q.; Song, W.; Fang, L.; Chen, Q.; Banks, C. E. *Energy Environ. Sci.* **2013**, *6*, 3665–3675.

(47) Zhou, J.; Booker, C.; Li, R.; Zhou, X.; Sham, T. K.; Sun, X.; Ding, Z. *J. Am. Chem. Soc.* **2007**, *129*, 744–745.

(48) Yang, S. T.; Cao, L.; Luo, P. G.; Lu, F.; Wang, X.; Wang, H.; Meziani, M. J.; Liu, Y.; Qi, G.; Sun, Y. P. *J. Am. Chem. Soc.* **2009**, *131*, 11308–11309.

(49) Liu, H.; Ye, T.; Mao, C. *Angew. Chemie - Int. Ed.* **2007**, *46*, 6473–6475.

(50) Pan, D.; Zhang, J.; Li, Z.; Wu, M. *Adv. Mater.* **2010**, *22*, 734–738.

(51) Gong, N.; Wang, H.; Li, S.; Deng, Y.; Chen, X.; Ye, L.; Gu, W. *Langmuir* **2014**, *30*, 10933–10939.

(52) Li, H.; He, X.; Kang, Z.; Huang, H.; Liu, Y.; Liu, J.; Lian, S.; Tsang, C. H. A.; Yang, X.; Lee, S.-T. *Angew. Chemie Int. Ed.* **2010**, *49*, 4430–4434.

(53) Cao, L.; Wang, X.; Meziani, M. J.; Lu, F.; Wang, H.; Luo, P. G.; Lin, Y.; Harruff, B. a; Veca, L. M.; Murray, D.; Xie, S.-Y.; Sun, Y.-P. *J. Am. Chem. Soc.* **2007**, *129*, 11318–11319.

(54) Nie, H.; Li, M.; Li, Q.; Liang, S.; Tan, Y.; Sheng, L.; Shi, W.; Zhang, S. X.-A. *Chem. Mater.* **2014**, *26*, 3104–3112.

(55) Links, D. A. *Phys. Chem. Chem. Phys.* **2012**, *14*, 7360–7366.

(56) Yang, Z.; Wang, M.; Yong, M.; Wong, Y.; Zhang, X. *Chem. Commun.* **2011**, *47*, 11615–11617.

(57) Ming, H.; Ma, Z.; Liu, Y.; Pan, K.; Yu, H.; Wang, F.; Kang, Z. *Dalton Trans.* **2012**, *41*, 9526–9531.

(58) Search, H.; Journals, C.; Contact, A.; Iopscience, M.; Address, I. P. *reports Prog. Phys.* **1999**, *62*, 1573–1659.

(59) Storck, S.; Bretinger, H.; Maier, W. F. *Appl. Catal. A Gen.* **1998**, *174*, 137–146.

(60) Wang, J.; Wang, C.-F.; Chen, S. *Angew. Chemie Int. Ed.* **2012**, *51*, 9297–9301.

(61) Zeng, L.; Lu, Z.; Li, M.; Yang, J.; Song, W.; Zeng, D.; Xie, C. *Appl. Catal. B Environ.* **2016**, *183*, 308–316.

(62) Pan, J.; Sheng, Y.; Zhang, J.; Wei, J.; Huang, P.; Zhang, X.; Feng, B. *J. Mater. Chem. A* **2014**, *2*, 18082–18086.

(63) Poyraz, A. S.; Song, W.; Kriz, D.; Kuo, C.; Seraji, M. S.; Suib, S. L. *ACS Appl. Mater. Interfaces* **2014**, *6*, 2–7.

(64) Li, H.; He, X.; Liu, Y.; Huang, H.; Lian, S.; Lee, S. T.; Kang, Z. *Carbon N. Y.* **2011**, *49*, 605–609.

(65) Kozák, O.; Datta, K. K. R.; Greplová, M.; Ranc, V.; Kašlík, J.; Zbořil, R. *J. Phys. Chem. C* **2013**, *117*, 24991–24996.

(66) Wen, X.; Yu, P.; Toh, Y.-R.; Ma, X.; Tang, J. *Chem. Commun. (Camb).* **2014**, *50*, 4703–4706.

(67) Wang, H.; Wei, Z.; Matsui, H.; Zhou, S. *J. Mater. Chem. A* **2014**, *2*, 15740–15745.

(68) Zhang, H.; Huang, H.; Ming, H.; Li, H.; Zhang, L.; Liu, Y.; Kang, Z. *J. Mater. Chem.* **2012**, *22*, 10501–10506.

(69) Zhang, L.; Lian, J.; Wu, L.; Duan, Z.; Jiang, J.; Zhao, L. *Langmuir* **2014**, *30*, 7006–7013.

(70) Adamu, H.; Dubey, P.; Anderson, J. A. *Chem. Eng. J.* **2016**, *284*, 380–388.

(71) Yan, X.; Ohno, T.; Nishijima, K.; Abe, R.; Ohtani, B. *Chem. Phys. Lett.* **2006**, *429* (4–6), 606–610.

(72) Ohtani, B. *J. Photochem. Photobiol. C Photochem. Rev*. **2010**, *11 (4)*, 157–178.

Chapter 3. Reduced Graphene Oxide Supported Nickel-Manganese-Cobalt Spinel Ternary Oxide Nanocomposites and Their Chemical-Converted Sulfide Nanocomposites as Efficient Electrocatalysts for Alkaline Water Splitting

3.1 Introduction

Increasing depletion of fossil fuels has stimulated intense research on the generation of clean and sustainable energy supply.[1] The electrochemical water splitting ($2H_2O(l) \rightarrow 2H_2(g) + O_2(g)$) is a promising pathway to fulfilling environmental friendly energy conversion and storage.[2,3] The water splitting reaction consists of two half-reactions: the oxygen evolution reaction (OER) and the hydrogen evolution reaction (HER). For the anode reaction, one of the key bottlenecks for the OER process in a large-scale production is the sluggish kinetics.[4–6] In this half-reaction, multiple proton-coupled electron transfers are occurred to generate molecular oxygen (acidic media: $2H_2O(l) \rightarrow 4H^+(aq) + O_2(g) + 4e^-$ or basic media: $4OH^-(aq) \rightarrow 2H_2O(l) + O_2(g) + 4e^-$). These electrochemical reactions also induce a relatively large overpotential (η). On the cathode side, the hydrogen evolution reaction not only provide a sustainable pathway to derive hydrogen from water but also serve as a reactant in fuel cell devices.[7] Currently, ruthenium oxide (RuO_2), iridium oxide (IrO_2), and Pt-based materials are regarded as state-of-the-art OER and HER catalysts, respectively.[8–10] However, the long-term utility of both active OER and HER catalysts in wide applications are highly limited by their high cost and low abundance.[11,12] Bifunctional catalyst

development is a critical topic in the solar fuel synthesis field. Alloys of precious metals have been found to present decent bifunctional electrochemical activity.[13] However, those metals are rare elements with a high cost.[14] Therefore, it is desirable to search for a low cost, highly abundant, and highly efficient materials as alternative catalysts for OER and HER, which are capable of achieving large-scale synthesis in the solar energy production industry.

First row transition metal oxides and sulfides, such as Co_3O_4, NiO, FeS have been widely used as electrocatalysts in electricity-driven water splitting in an alkaline medium, because they are accessible and abundant in the earth.[15–20] Co_3O_4 spinels have been specifically explored, which were found to be highly efficient electrocatalysts toward OER and HER.[21] In the normal spinel structure, Co_3O_4 consists of two types of cobalt ions, divalent cobalt ions (Co^{2+}) usually in the tetrahedral sites and trivalent cobalt ions (Co^{3+}) in the octahedral sites.[22] Metallic cobalt has been found to have a low energy barrier for H adsorption, which makes the Co-based catalyst promising candidates for HER.[23] However, because of the toxicity of Co^{2+}, environmentally friendly metal ions have been attempted to replace Co^{2+} and therefore promote the electron transfer efficiency.[24] The divalent cobalt component could be substituted partially with other divalent transition metals because of similarities in atom radii, such as Cu, Mn, and Ni.[25,26] Divalent cobalt ions in tetrahedral sites can be extended to bond with neighboring oxygen anions, which make the cobalt ions octahedral centered. Regarding the catalytic activities of these spinel oxides, the degree of substitution has a significant effect on the physicochemical properties, which are correlated with the catalytic performance. The co-existence of Ni, Mn, and Co in the spinel structure leads to the formation of single-phase ternary oxides. In such a spinel metal oxide system, the activation energies required for electron transfer between cations are relatively low, due to the presence of mixed valent multiple cations.[27,28] Therefore, the single-phase ternary oxides usually exhibit higher electrical conductivity, which is beneficial to their electrochemical activity.

To enhance the charge and mass transport efficiency, a coupling of transition metal oxides or sulfides with a three-dimensional conductive nanocarbon support such as graphene (oxide) and carbon nanotubes is an efficient strategy to improve the electrocatalytic activity and the durability, due to their high electric conductivity, high surface area, and good mechanical strength.[29] For example, a hybrid material composed of Co_3O_4 and N-doped graphene oxide has been reported for its superior oxygen electrocatalytic activity. The good catalytic performance contributed to the synergetic effects between Co_3O_4 nanocrystals and graphene oxides.[30] Graphene (oxide) has also been widely used as a substrate for supports, such as metal oxides,[31] metal sulfides,[32] metal hydroxides,[33] and layered double hydroxides.[34] Bottom-up syntheses allow the self-assembly of ternary oxides or sulfides on the graphene sheets with versatile structures. The electron transfer behaviors and physicochemical properties could be greatly modified by the incorporation of graphene sheets. Inspired by the virtues of graphene oxide and the low electron transfer activation energy of multi-phase mixed metal oxides, ternary oxide and graphene oxide heterostructure catalysts could be superior for electrochemistry applications.

In this work, we developed reduced graphene oxide supported Ni-Mn-Co ternary oxide nanocomposites synthesized by a two-step solvothermal synthesis followed by calcination under inert gas, during which GO is further reduced to rGO (denoted as rGO/NMC). The resulting product was further converted into a corresponding sulfide via a direct sulfurization reaction (denoted as rGO/NMC-S). Their catalytic activities were evaluated for OER and HER under alkaline conditions, respectively. Based on the experimental results, the obtained rGO/NMC composites exhibit a comparable OER electrocatalytic activity than the state-of-the-art RuO_2 and IrO_2 catalysts, and the as-converted rGO/NMC sulfide composites present an efficient HER activity under alkaline conditions. Density functional theory (DFT) calculations were performed to better understand the nature of the HER reaction processes. The results indicate a higher preferability of the HER reaction for sulfide surfaces than oxide surfaces.

3.2 Experimental Section

3.2.1 Chemicals

Graphite flakes, sodium chloride, sulfuric acid, sodium nitrate, 30% hydrogen peroxide, nickel(II) nitrate hexahydrate, manganese(II) nitrate tetrahydrate, cobalt(II) nitrate hexahydrate, sodium hydroxide, ammonium hydroxide solution, ethyl alcohol, 2-proponal, 5 wt% Nafion. All chemicals were used as received and used without further purification.

3.2.2 Synthesis of Graphene Oxide (GO)

GO was synthesized by a modified Hummer's method.[35] The obtained GO was washed with 5% HCl and deionized water until neutral, and finally re-dispersed in a certain amount of deionized water to give an aqueous solution with a concentration of 1.8 mg/mL. The concentration of the GO suspension was determined by measuring the volume of the GO suspension and the mass of GO after freeze drying overnight.

3.2.3 Synthesis of rGO/NMC Ternary Oxide Composites

In a typical synthesis procedure, rGO/NMC ternary oxide composites were prepared via a two-step solvothermal method. Stoichiometric amounts of $Ni(NO_3)_2•6H_2O$, $Mn(NO_3)_2•4H_2O$ and $Co(NO_3)_2•6H_2O$ were dissolved in ethanol to obtain a homogeneous solution. Subsequently, a NH_4OH solution and a GO suspension were separately added to the above solution under magnetic stirring. The resultant solution was refluxed at 80 °C for 12 h and then transferred into a Teflon-lined stainless steel autoclave, which was sealed for a solvothermal treatment at 180 °C for 6 h. The resulting product was washed with water, and dried at 80 °C overnight to produce the GO/NMC ternary oxide nanocomposite. In the second step, the resulting product from the first step was placed in a tubular furnace and calcined at 300 °C under an Ar atmosphere for 4 h, which reduced GO to rGO. The final product is denoted as rGO/NMC.

3.2.4 Direct Conversion of rGO/NMC-312 Ternary Oxide Composites into rGO/NMC-312 Ternary Sulfide Composites

The rGO/NMC-312 ternary oxide composite was used for direct conversion to its corresponding sulfide. The oxide-to-sulfide conversion experiments were carried out in a laboratory scale sulfurization apparatus, as shown in **Scheme 3.1**. The experimental setup consists of a tubular quartz reactor in a tube furnace with programmable digital control under atmospheric pressure. The sample was loaded in a porcelain combustion boat for each experiment. A gas mixture (1% H_2S in He) was passed through the catalyst bed at a flow rate of 40 sccm at 250 °C for 10 h. The obtained sample was labeled as rGO/NMC-312-S.

3.2.5 Materials Characterization

All the synthesized materials were ground to a fine powder in an agate mortar. The Powder X-ray diffraction (XRD) analysis was carried out at room temperature on a Rigaku Ultima IV diffractometer (Cu Kα radiation, λ = 1.5406 A). A beam voltage of 40 kV and a current of 44 mA were used. The morphologies of the materials were investigated using an FEI Nova NanoSEM 450 with an accelerating voltage of 2.0 kV. Transmission electron microscopy (TEM) and high-resolution transmission electron microscopy (HRTEM) images were collected using a JEOL 2010 UHR FasTEM microscope operating at 200 kV. N_2 sorption measurements were performed on a

Scheme 3.1 Schematic Diagram of Sulfurization Experimental Setup

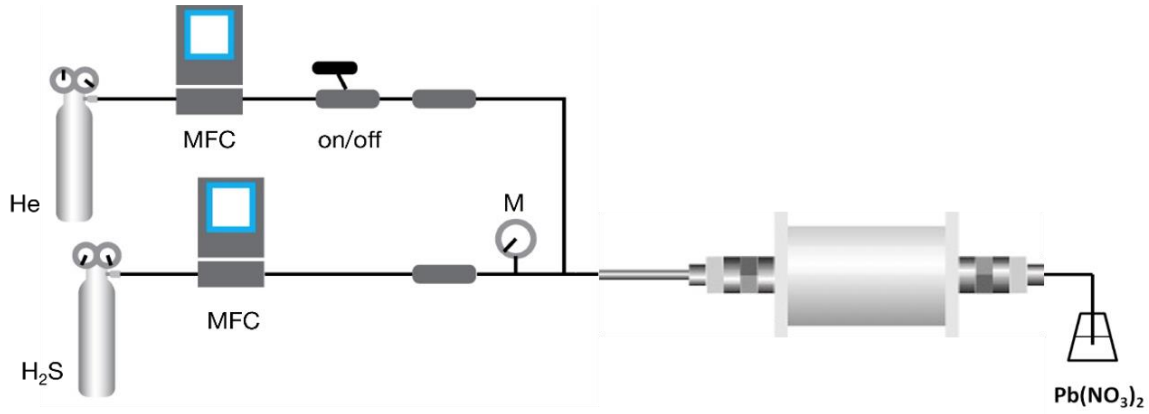

Quantachrome Autosorb-1-1C automated sorption system. The samples were degassed at 150 °C for 6 h prior to the experiments. The surface areas were calculated by the Brunauer−Emmett−Teller (BET) method, and the pore size distributions were obtained by the Barrett−Joyner−Halenda (BJH) method from the desorption branch of the isotherms. The thermogravimetric analysis (TGA) was performed using a Hi-Res TA Instrument Model Q100, in the temperature range between 25 and 800 °C at a ramping rate of 10 °C min^{-1} in an air atmosphere. Raman spectra were taken with a Renishaw 2000 Raman microscope with an Ar^+ ion laser (514 nm) as the excitation source. X- ray photoelectron spectroscopy (XPS) measurements were performed in a PHI Model 590 spectrometer with multiprobes (Al Kα radiation, λ = 1486.6 eV, operated at 250 W).

3.2.6 Electrochemical Measurements

All the electrochemical measurements were performed in a three-electrode cell on a CHI 760E electrochemical workstation at room temperature. A platinum wire and a saturated calomel electrode (SCE) were used as a counter electrode and a reference electrode, respectively. The potentials reported in this work are referenced to the reversible hydrogen electrode (RHE). The working electrode consists of pyrolytic graphite carbon, coated with the as-prepared sample. The working electrode was prepared as follows: 5 mg of catalyst sample was dispersed in 1 mL of a deionized water/2-propanol mixture with a volume ratio of 3:1; then 40 μL of 5 wt% Nafion solution was added. The mixture catalyst ink was ultrasonicated for 30 min. Then, 8 μL of the suspension was loaded onto the pyrolytic graphite substrate. Finally, the as-prepared working electrode was air-dried at room temperature for electrochemical measurements. The active loadings of catalyst were 0.2 $mg \cdot cm^{-2}$. The OER activity of the catalysts was evaluated using linear sweep voltammetry (LSV) in the potential window ranging from 1.1 to 1.7 V versus RHE. Electrochemical impedance spectroscopy (EIS) was carried out in O_2-saturated 0.1 M KOH solution at an applied potential of 1.67 V (vs. RHE). The spectra were collected at an ac voltage

of 5 mV with the frequency range from 0.1 to 105 Hz. Chronopotentiometry experiments were performed at a constant current density of 10 $mA \cdot cm^{-2}$ at a rotation speed of 1600 rpm. The potential window was set between 1.4 V and 1.8 V (vs. RHE), which falls in the OER active potential range. The HER measurements were carried out by using Ni foam (1×1 cm) covered with electrocatalysts as the working electrode, a graphite rod, and an SCE as a counter electrode and a reference electrode, respectively. The working electrode was prepared as follows: 5 mg of catalyst sample and 40 μL of a 5 wt% Nafion solution was dispersed in 400 μL of a water/ethanol solvent mixture with a volume ratio of 1:3. The mixture catalyst ink was ultrasonicated for 30 min. Then 40 μL of the homogeneous suspension was dropped onto Ni foam and left air dry. The active loadings of catalyst were 0.53 $mg \cdot cm^{-2}$. The HER activity of the catalysts was evaluated using linear sweep voltammetry (LSV) in the potential window ranging from -0.5 to 0.0 V versus RHE. Electrochemical impedance spectroscopy (EIS) was carried out in O_2-saturated 0.1 M KOH solution at an applied potential of -0.2 V (vs. RHE). The spectra were collected at an ac voltage of 5 mV with the frequency range from 0.01 to 100 kHz. Chronopotentiometry experiments were performed at a constant current density of 10 $mA \cdot cm^{-2}$. The potential window was set between -0.2 V and 0.0 V (vs. RHE), which falls in the HER active potential range. Note all the LSV and CV tests were 100% iR compensated.

3.3 Results

3.3.1 Structure Characterization

The rGO/NMC-312 composite was synthesized by a two-step solvothermal pathway using $Ni(NO_3)_2 \cdot 6H_2O$, $Mn(NO_3)_2 \cdot 4H_2O$, $Co(NO_3)_2 \cdot 6H_2O$, GO as precursors in a solution containing ammonia and ethanol at 80 °C. The key issue for the successful preparation of the spinel ternary oxide without phase separation is the presence of the chelating agent. During the hydrolysis

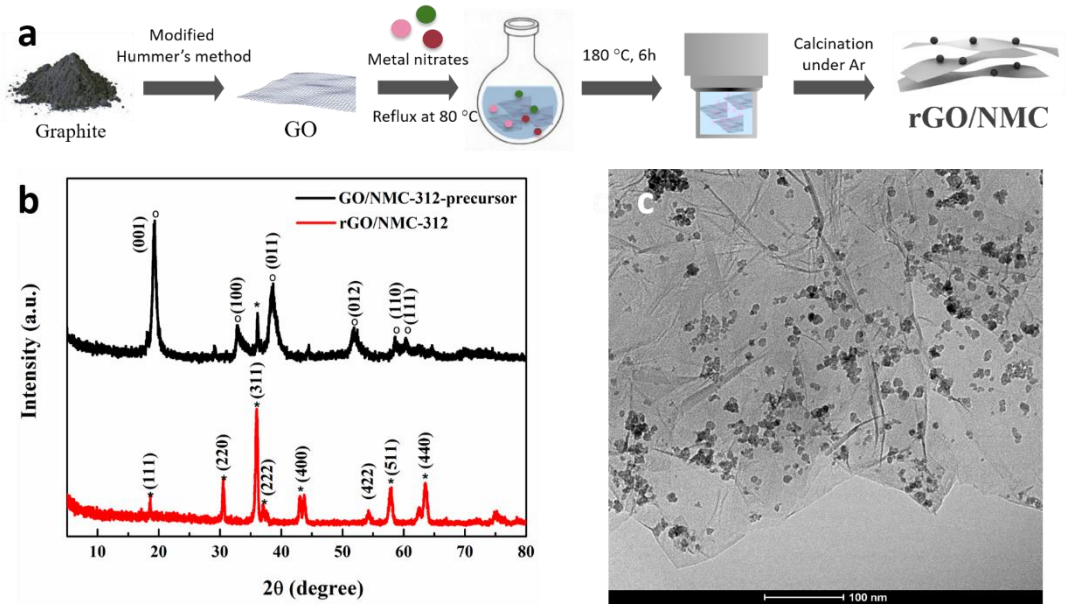

Figure 3.1 (a) Schematic illustration of the synthesis of rGO/NMC materials; (b) XRD patterns of GO/NMC-312-precursor and rGO/NMC-312 ternary oxide composite; (c) TEM images of rGO/NMC-312 ternary oxide composite.

process, the Ni-Mn-Co ternary oxide was *in situ* growing on the surface of oxidized graphene sheets from the oxidation of metal nitrate precursors, in which ammonia acts as a chelating agent, to prevent the formation of single metal hydroxide (oxide). Ethanol provides a mild reducing condition. The reaction mixture initially contains metal nitrate salt with a high ammonia concentration and a high pH value. In the presence of concentrated ammonia solution, metal-ammonia complex cations started to form at room temperature by coordinating with metal nitrate salts. Then the resulting solution was heated to reflux at 80°C overnight in a semi-closed atmosphere. The slow evaporation of ammonia molecules during the reflux process facilitates the hydrolysis of metal-ammonia complexes to metal hydroxide co-precipitates. We investigated the pH change with time to track the degree of ammonia evaporation. The pH value was slowly decreasing along with the reflux process due to the condensing process. The pH value was tested to be 9.2 at the end of the reflux reaction, which confirmed the existence of ammonia after reflux. Various O-containing functional groups and defects on GO facilitate the *in situ* growth of the rGO/NMC-312 composite. A further hydrothermal treatment results in a further reduction of GO and better crystallization. Subsequently, the above composite is calcined at 300 °C under an Ar atmosphere to achieve a completed reduction of GO and crystallization of NMC-312 spinel ternary oxide (See experimental section for detailed information, **Figure 3.1a**).

The crystal structures of the as-synthesized composite and its precursor after co-precipitation during reflux reaction were characterized by X-ray diffraction (XRD). As shown in **Figure 3.1b**, the diffraction pattern of the precursor can be indexed as having the hexagonal $Mn(OH)_2$ structure, indicating the formation of a mixed hydroxide after co-precipitation in a basic environment. Hydrothermal treatment and annealing led to the oxidation and crystallization of a metal hydroxide precursor, forming the spinel ternary oxide immobilized on GO sheets. The XRD pattern of rGO/NMC-312 ternary oxide confirms the spinel structure. All the diffraction lines can be indexed to be a cubic spinel Co_3O_4 structure with a space group of Fd3m. The absence of any separate

nickel oxide or manganese oxide phases indicates the successful incorporation of Ni and Mn atoms into the Co_3O_4 lattice. The TEM image in **Figure 3.1c** shows that the NMC spinel oxide nanoparticles are present as fine nanospheres with a size of 7~10 nm dispersed on a uniform thin graphene sheet, which further verified the successful formation of the hybrid materials.

To demonstrate the choice of 3:1:2 as the optimal ratio of Ni: Mn: Co, the phase composition of each NMC material with a different metal ratio was confirmed by XRD. The values of lattice parameters were significantly affected by the degree of substitution of Ni and Mn in Co_3O_4. When Mn acts as the leading metal, the cubic spinel crystal structure was stretched into a tetragonal crystal system, with a large crystallite size and volume. In contrast, with increased Ni content in the ternary oxides, the crystallite size along the (311) directions of NMC-312 decreased to 7.8 nm. The cubic spinel structure was also preserved in the NMC-312 sample, with an increased lattice parameter. Other than the crystal structure, the morphologies of samples with different metal ratios are also varied. Both NMC-213 and NMC-231 samples exhibit aggregate particle clusters attached on the surface of the graphene sheet, while the NMC-312 sample shows a smooth surface. Thus, the rGO/NMC-312 nanocomposites were used for further characterization, electrocatalytic activity tests for OER, and direct oxide-to-sulfide conversion.

The reduction of GO is further confirmed by Raman spectroscopy, as the D band/G band intensity ratio is an indicator of the degree of oxidation.[36,37] We used a modified Hummer's method for the synthesis of mildly oxidized graphene oxides. As shown in **Figure 3.2a**, the as-prepared graphene oxides exhibit a D band located at around 1340 cm^{-1} and a G band located at around 1590 cm^{-1}, along with a 2D band located at around 2705 cm^{-1} and an S3 band located at around 2925 cm^{-1}. Compared to pure graphene oxides, there is no obvious position change observed in the Raman bands of rGO/NMC-312. The D/G intensity ratio of the rGO/NMC-312 composite showed a clear

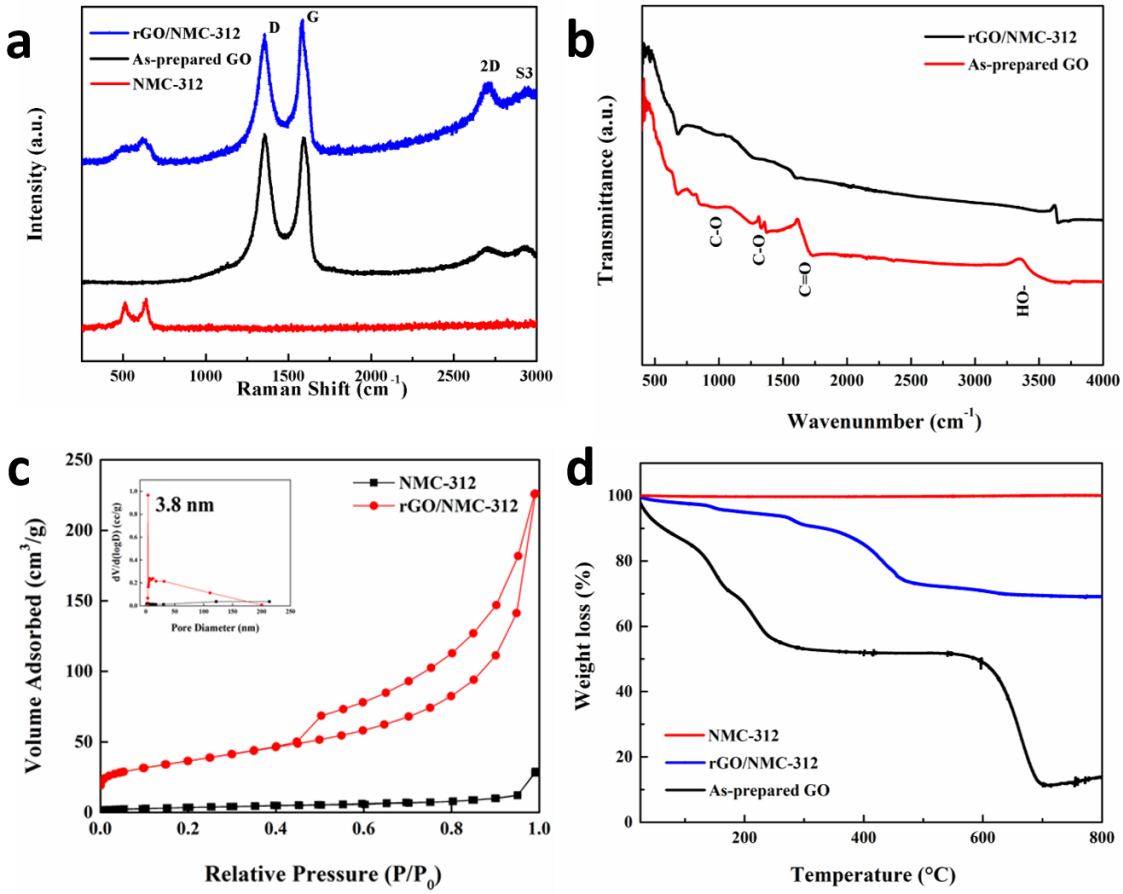

Figure 3.2 (a) Raman spectra of rGO/NMC-312 ternary oxide composite, as-prepared GO and rGO/NMC-312; (b) FT-IR spectra of a prepared GO and rGO/NMC-312 ternary oxide composite; (c) N_2 sorption isotherms and the corresponding pore size distribution curve of NMC-312 and rGO/NMC-312 ternary oxide composite; (d) Thermogravimetric analysis profiles of NMC-312, rGO/NMC-312, and As-prepared GO.

decrease, suggesting a lower defect concentration and an increased average size of the crystalline graphene domains.[38] The presence of the Raman bands around 512 cm^{-1} and 640 cm^{-1} in the spectrum of rGO/NMC-312 confirms the uniform formation of rGO/NMC-312 composites. A Fourier transform infrared spectroscopy (FT-IR) study (**Figure 3.2b**) revealed the reduction of graphene oxides as well. Compared to the as-prepared GO, most of the oxygen-containing functional groups in rGO/NMC-312 are removed, as indicated by the weaker signal in the FT-IR spectra. These data prove a successful growth of NMC ternary oxide on graphene sheets and a reduction of graphene oxides.

N_2 sorption measurements were carried out to study the porous structure and textural properties of the rGO/NMC-312 composites. As shown in **Figure 3.2c**, the NMC-312 ternary oxide has a nonporous structure with a surface area of 8 m^2/g, while the surface area increased to 128 m^2/g when the material is nucleated and grown on the graphene sheet. The rGO/NMC-312 composite exhibits a Type-H3 adsorption isotherm, according to the IUPAC classification. The rGO/NMC-312 composites show a much larger N_2 uptake than the NMC-312 ternary oxide, indicating the existence of slit-shaped pores, which may result from the layered structure of graphene sheets.[39] Thermal-gravimetric analysis (TGA) was used to determine the actual graphene/ternary oxide ratio in the rGO/NMC-312 composite and to confirm the high thermal stability of the composite. **Figure 3.2d** shows the TGA profile of as-prepared GO in an air atmosphere. Due to a significant amount of oxygen-containing groups in GO, the first weight loss below 250 °C was a result of the release of CO_2 and H_2O upon decomposition of carboxylic and ketone groups.[40,41] With increased temperature, the GO was completely decomposed after 700 °C. As a sharp contrast, the TGA profile of as-prepared NMC nanoparticles barely shows a weight loss, which confirmed the high thermal stability of the ternary oxide materials. To confirm the actual fraction of graphene in the

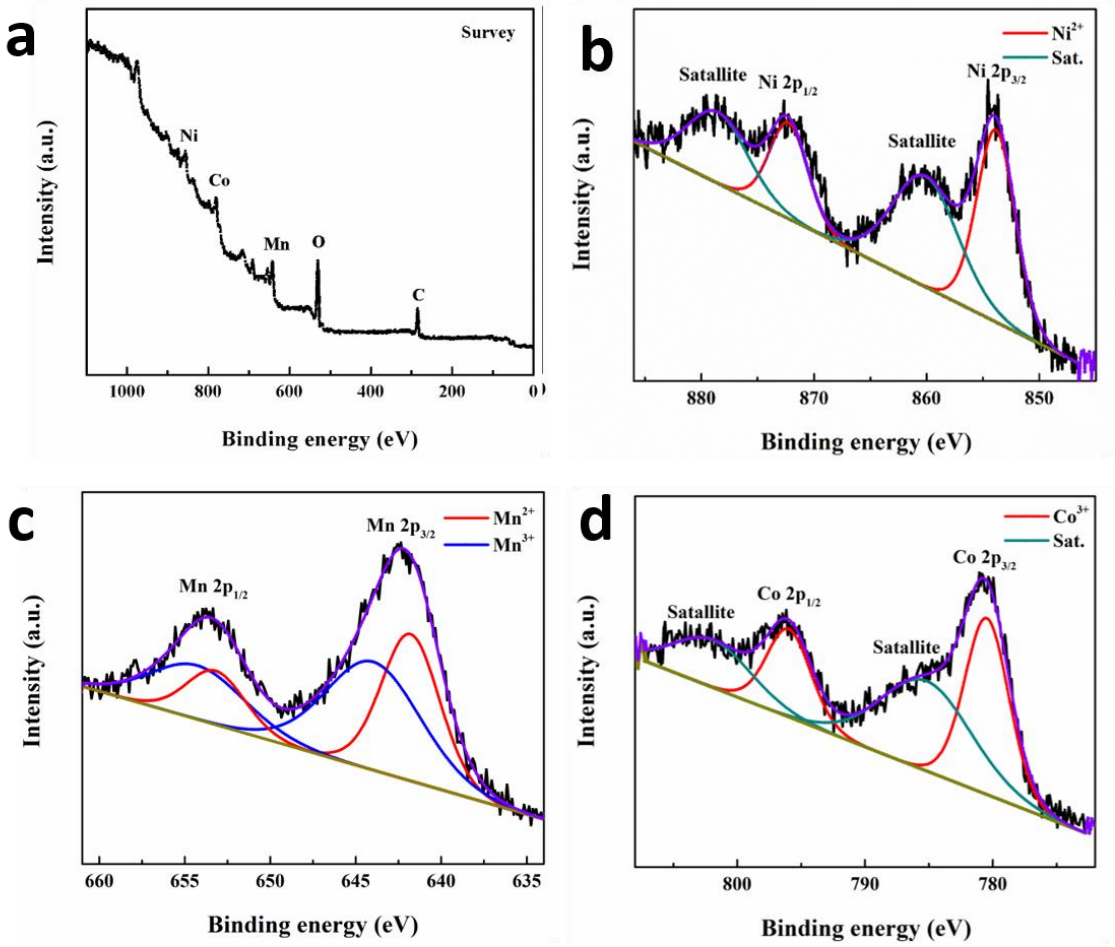

Figure 3.3 (a) XPS survey scan; (b-d) High-resolution XPS patterns of Ni 2p, Mn 2p, Co 2p for rGO/NMC-312.

composite, TGA analysis was performed on the rGO/NMC-312 composite. As NMC-312 ternary oxide exhibits high thermal stability, the weight loss of 20% between 400 and 700 °C should be attributed to the burning of the carbon skeleton.[42] Thus the graphene oxide loading amount in the composite is found to be around 20% based on the TGA results, which is in agreement with the feeding amount in the synthetic procedure.

X-ray photoelectron spectroscopy (XPS) was used to investigate the oxidation states of each metal ion in the rGO/NMC-312 composite (**Figure 3.3**). The survey spectrum revealed Ni, Mn, Co, C, and O species in the material, consistent with the EDX results (**Figure 3.4e**). The peak deconvolution was carried out using Gaussian-Lorentzian curve fitting based on the Shirley background correction. **Figure 3.3b** shows the Ni 2p XPS spectrum. These two peaks were fitted into two peaks at 873.3 and 854.9 eV, which can be ascribed to Ni^{2+}, corresponding to Ni $2p_{1/2}$ and Ni $2p_{3/2}$, respectively. In **Figure 3.3c**, two peaks are observed at 641.6 and 651.9 eV, and another two Mn $2p_{3/2}$ and Mn $2p_{1/2}$ spin-orbit coupling peaks are at 642.4 and 653.8 eV, which are characteristic lines of Mn^{2+} and Mn^{3+}, respectively. These results implied the presence of mixed-valent manganese in NMC spinel oxide, with a Mn^{2+}/Mn^{3+} ratio of 0.8 (estimated from the corresponding peak areas). **Figure 3.3d** shows the peaks of Co $2p_{3/2}$ and Co $2p_{1/2}$ of rGO/NMC-312. These two fitted peaks at 780.3 and 795.8 eV are ascribed to Co^{3+}. The results probably indicated that Co^{2+} had been fully substituted by Ni^{2+} and Mn^{2+}.

The uniform growth of ternary oxide nanoparticles on graphene sheets is clearly shown in TEM images. The rGO/NMC-312 nanoparticles with a crystalline grain sizes in the range of 7-10 nm are dispersed on the graphene sheets (**Figure 3.4a, b**). The grain sizes of these crystalline NMC nanoparticles are in accordance with the calculated crystal size from the XRD pattern (7.8 nm). The reduced graphene oxide sheets exhibit large, thin, flexible, and transparent features. The lattice fringe of the nanoparticles showed an interplanar distance of 0.46 nm correspond to the (111) planes of NMC spinel oxide. The lattice spacing of 0.24 nm corresponds to the (311) planes of

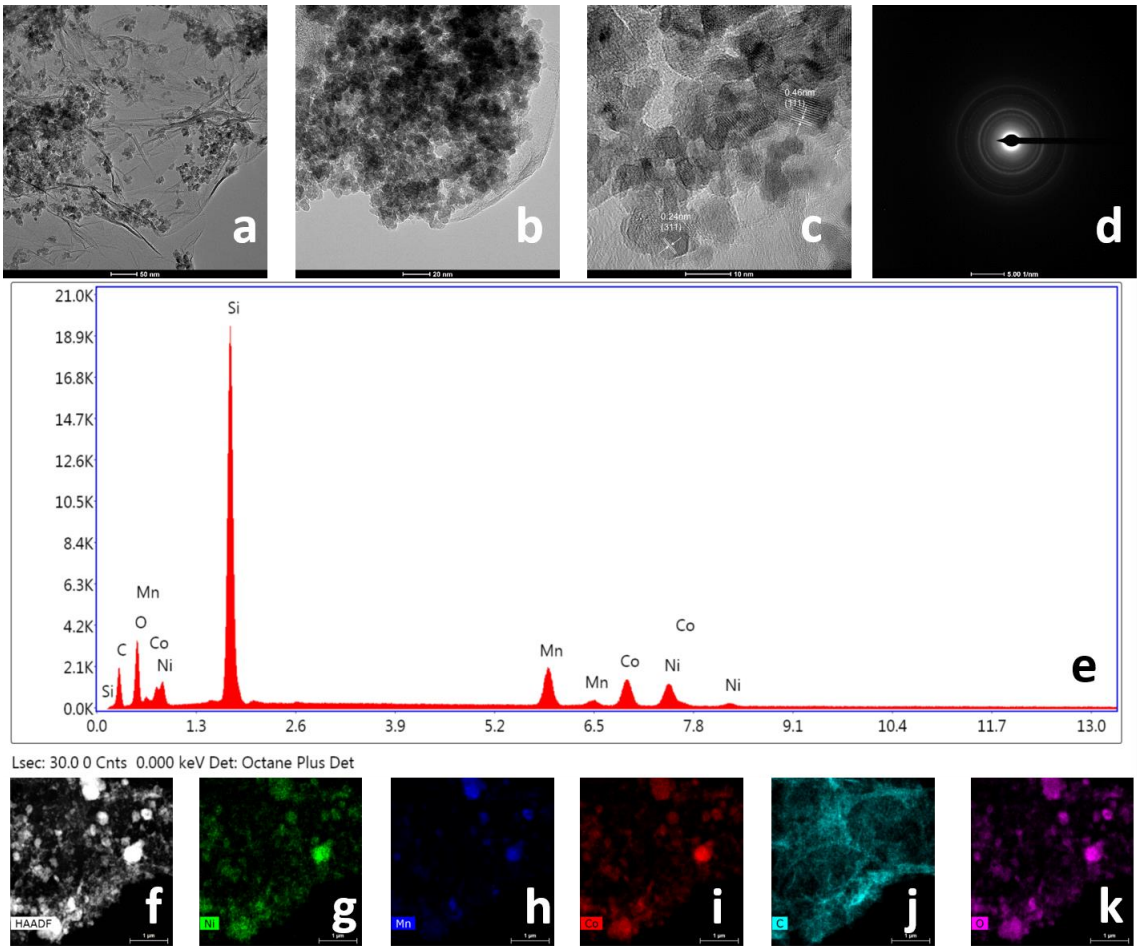

Figure 3.4 (a-c) TEM images; (d) SAED pattern; (e) EDX profile of the rGO/NMC-312; (f-k) elemental mapping of the rGO/NMC-312.

NMC spinel oxide (**Figure 3.4c**). The corresponding selected area electron diffraction (SAED) pattern (**Figure 3.4d**) showed clear and ordered rings, indicating the existence of single spinel phase with a defined orientation. To confirm the existence of Ni, Mn, Co in a single particle, the elemental composition of the rGO/NMC nanoparticles was studied through energy dispersive X-ray spectroscopy (EDX) equipped with TEM (**Figure 3.4e**). The presence of Ni, Mn, and Co peaks indicates the formation of a single-phase mixed metal oxide. Additionally, the corresponding elemental mapping images of each element are given in **Figure 3.4f-k**. Ni, Mn, Co, and O exist homogeneously in an individual particle, which confirmed the formed nanoparticles are spinel ternary oxides rather than

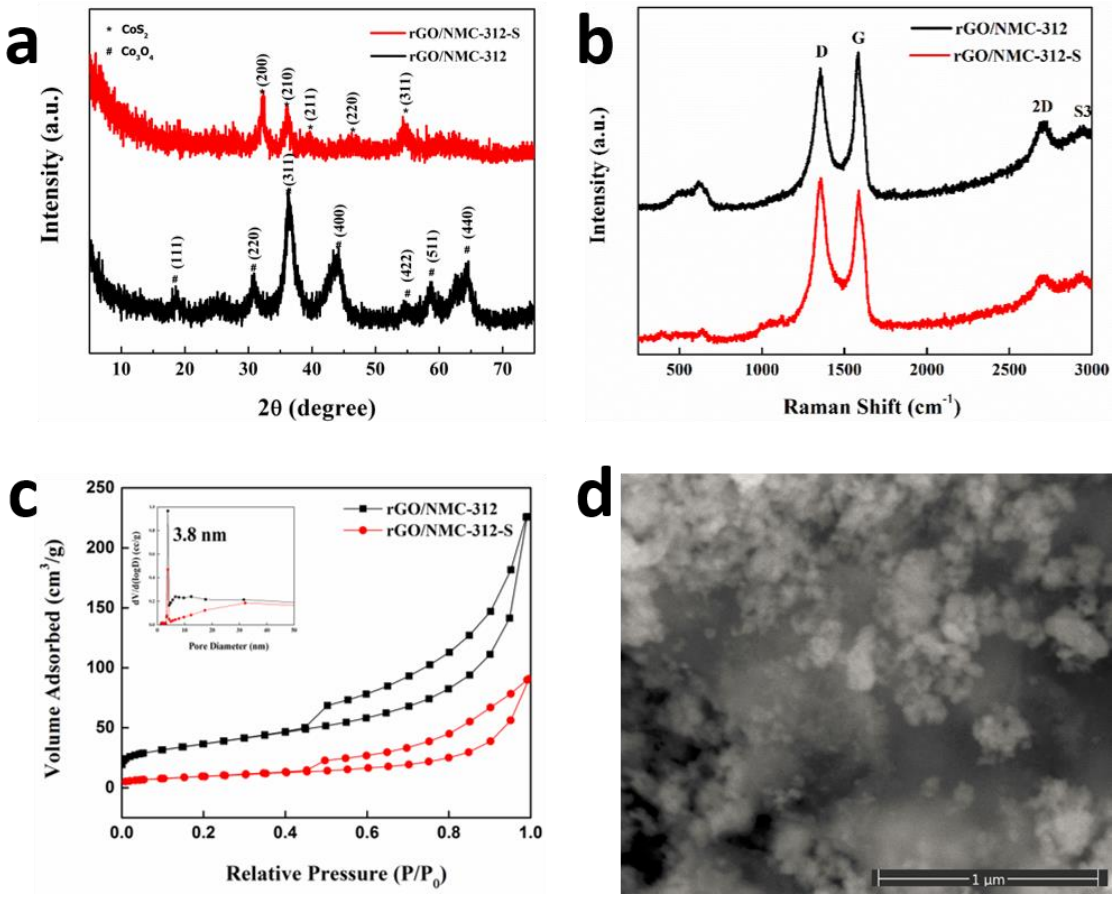

Figure 3.5 (a) X-ray diffraction patterns; (b) Raman spectra; (c) N_2 sorption isotherms and the corresponding pore size distribution curve of rGO/NMC-312 ternary oxide composites and as-converted rGO/NMC-312 ternary sulfide composites; (d) SEM images of as-converted rGO/NMC-312 ternary sulfide composites.

separated Ni, Mn, and Co oxides, consistent with the PXRD results. Carbon is uniformly distributed in the mapping image of rGO/NMC, which represents thin layers of graphene sheets. The EDX results indicate that the NMC-312 nanoparticles are attached to the surface of graphene sheets.

3.3.2 Direct Conversion of rGO/NMC-312 Ternary Oxide Composites into rGO/NMC-312 Ternary Sulfide Composites

The chemical conversion of rGO/NMC-312 ternary oxide composites into rGO/NMC-312 ternary sulfide composites was then carried out in the sulfurization apparatus (**Scheme 3.1**). The PXRD pattern of the as-converted sulfide composite shows that all the diffraction lines can be indexed to the cubic spinel Co_3S_4 phase (**Figure 3.5a**). No additional line from Co_3O_4 spinel can be observed. The crystallographic properties of the rGO/NMC-312 ternary oxide and the as-converted sulfide composites are summarized in **Table 3.1**. Raman spectroscopy was performed to confirm the coupling between the NMC-312 ternary sulfide and the reduced graphene oxide sheet. As shown in **Figure 3.5b**, the characteristic peak of C-$(S\text{-}S)_n$ at 654 cm^{-1} was observed. The presence of this peak indicated the strong interaction between sulfide and carbonaceous species, which are related to the electrochemical activity.[43]

Porosity was also studied by N_2 sorption measurements. **Figure 3.5c** shows the changes of N_2 sorption isotherms along with the BJH pore size distributions before and after the oxide-to-sulfide conversion. The rGO/NMC-312 oxide composite has a surface area of 128 m^2/g and the as-converted sulfide composite has a surface area of 57 m^2/g. The dramatic decrease in surface area is attributed to the higher atomic weight per metal atom as compared to corresponding oxide compounds with similar porosity.[44] The SEM image of the as-converted rGO/NMC-312 ternary sulfide composites shows rough surfaces, which could probably serve as more active sites for H adsorption (**Figure 3.5d**). The TEM images reveal that the grain size of the as-converted sulfide was about 10-15 nm (**Figure 3.6a-c**). The elemental mapping was employed to further confirm the

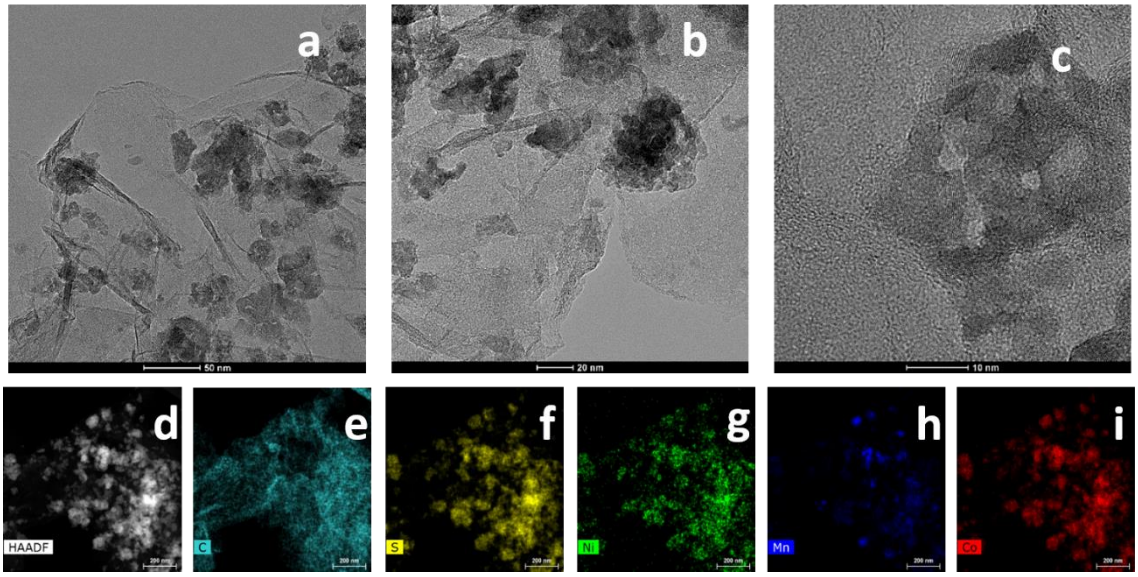

Figure 3.6 (a-c) TEM images; (d-i) elemental mapping of as-converted rGO/NMC-312 ternary sulfide composites.

uniform dispersion of the above five elements in the nanocomposites (**Figure 3.6d-i**). The extent of sulfurization of a material is based on the diffusivity of the sulfur source.[45] As shown in **Figure 3.6f**, sulfur elements are uniformly distributed throughout the particle. High resolution XPS spectra of Ni 2p, Mn 2p, and Co 2p were obtained to investigate the oxidation state of each element. The binding energies of Ni and Mn gave similar results as those of rGO/NMC-312 ternary oxide composites, indicating that the Ni^{2+} is preserved as the dominant oxidation state with the coexistence of Mn^{2+} and Mn^{3+} with a Mn^{2+}/Mn^{3+} ratio of 2 (estimated from the corresponding peak areas). In the case of Co, a pronounced satellite feature was observed due to the mixed valent state of Co^{2+} and Co^{3+}. **Figure 3.7d** reveals that the Co^{2+}/Co^{3+} ratio is approximately 2, much higher than that in the corresponding oxide composites. Compared to rGO/NMC-312 ternary oxide

Table 3.1 Average lattice constants, crystallite sizes, crystallite volume, crystal system of rGO/NMC-312 ternary oxide composites and as-converted rGO/NMC-312 ternary sulfide composites.

Materials	Average Lattice Constant (a_0)	Crystallite Size (nm)	Crystallite Volume (A^3)	Crystal System
rGO/NMC-312	0.819	7.8	550	Cubic
rGO/NMC-312-S	0.553	8.1	170	Cubic

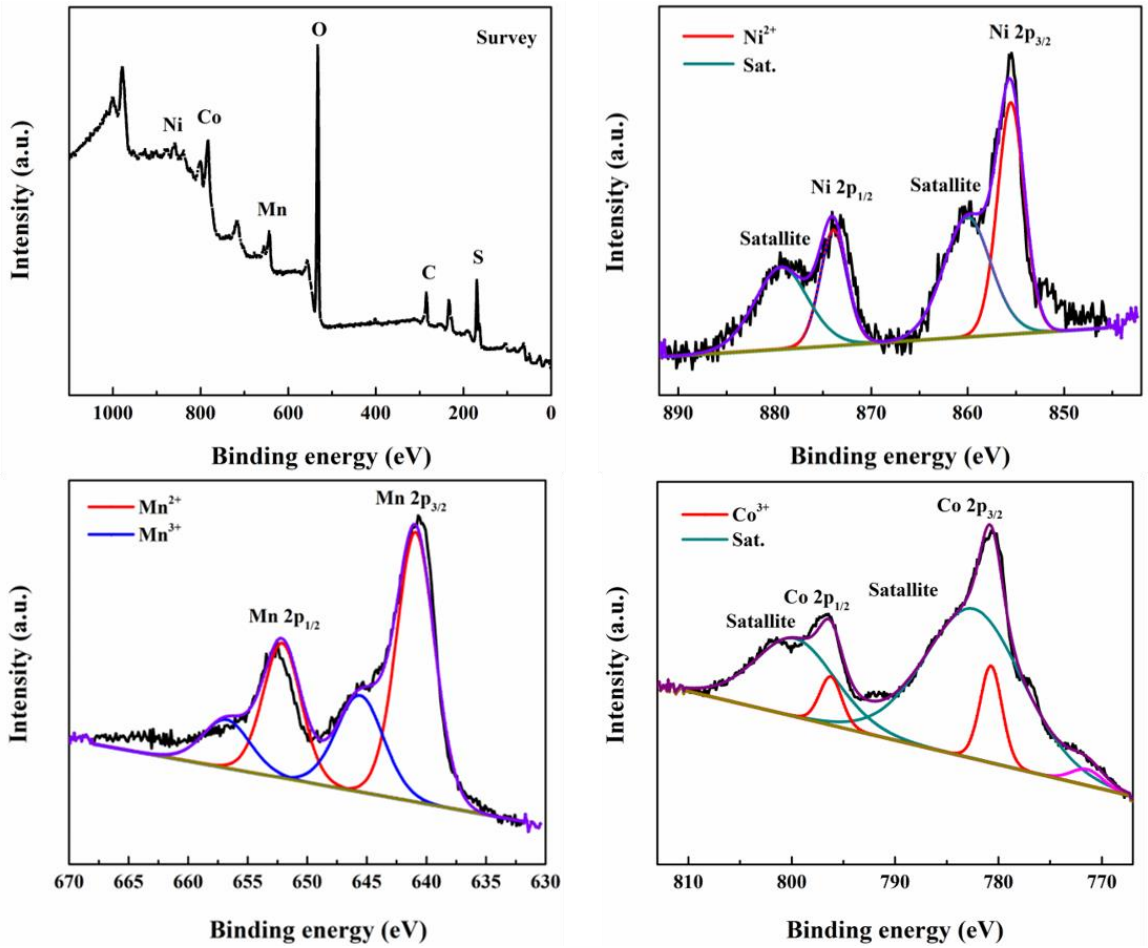

Figure 3.7 (a) XPS survey scan; (b-d) High-resolution XPS patterns of Ni 2p, Mn 2p, Co 2p for rGO/NMC-312-S.

composites, large populations of Co^{2+} and Mn^{2+} are present in the as-converted sulfide composite, which might contribute to an enhanced HER activity due to the higher concentration of oxygen vacancies (**Figure 3.7**).

3.3.3 OER Electrocatalytic Performance of rGO/NMC-312 Ternary Oxide Composites

To assess the OER performance of the rGO/NMC-312 composite, our material dispersions were first deposited onto pyrolytic glassy carbon working electrodes before measurements. Linear sweep voltammetry (LSV) was done in an O_2-saturated 0.1 M KOH electrolyte utilizing a rotating disk electrode (RDE) with a scan rate of 5 mV/s in a three-electrode system using saturated calomel electrode (SCE) as a reference electrode and platinum wire as a counter electrode. During each

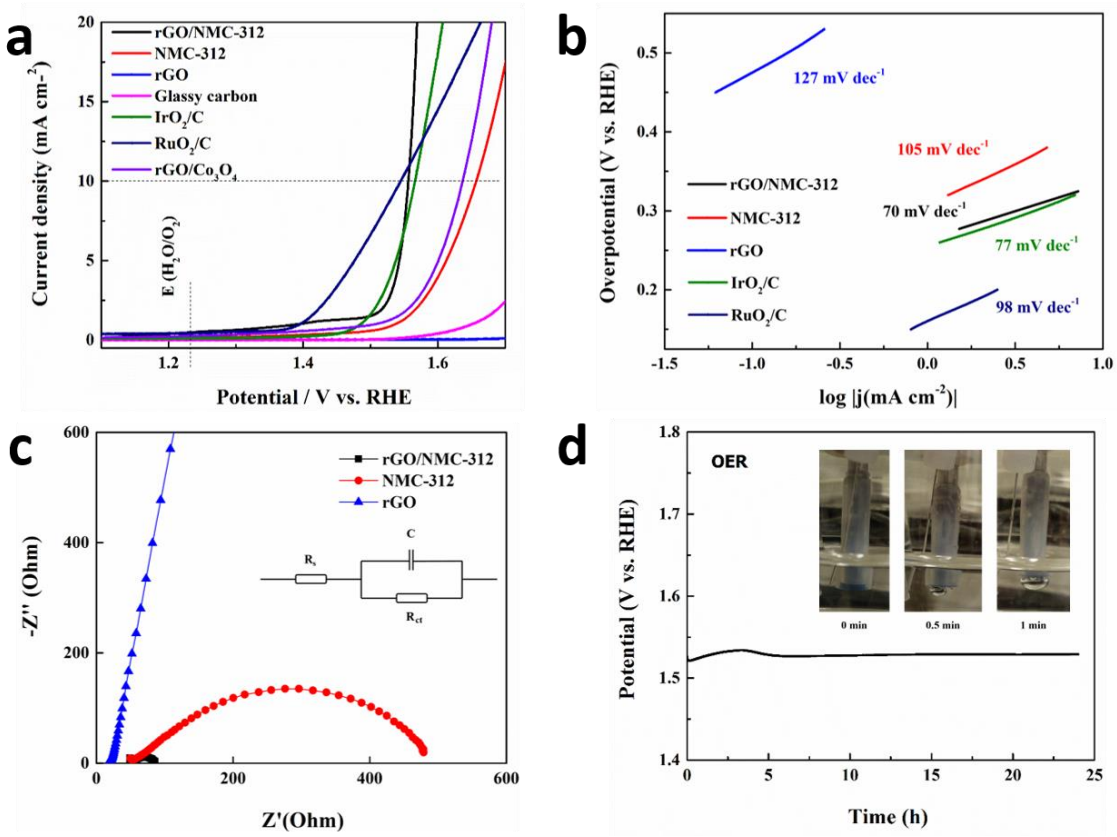

Figure 3.8 OER electrocatalytic performances. (a) Polarization curves and (b) Tafel plots of different catalysts on pyrolytic glassy carbon in O_2-saturated 0.1 M KOH at a scan rate of 10 mV/s; (c) Nyquist plots of rGO/NMC-312 ternary oxide composites at 1.66 V vs. RHE. Inset: the fitted equivalent circuit; (d) Chronopotentiometry curve of rGO/NMC-312 ternary oxide composites at a constant current density of 10 $mA \cdot cm^{-2}$. Inset: photographs showing generation of oxygen bubbles on the rGO/NMC-312 ternary oxide composite modified GCE (Glassy carbon electrode, which has a $0.196 \cdot cm^{-2}$ surface) (All tests are for OER).

measurement, the working electrode was rotated at a speed of 1600 rpm to limit diffusion effects and remove oxygen gas product from the electrode surface.

In order to better evaluate the electrochemical activity of rGO/NMC-312 composite for OER, NMC-312, reduced graphene oxide, IrO_2/C catalyst, RuO_2/C catalyst, and bare glassy carbon electrode were chosen as reference points. As shown in **Figure 3.8a**, the polarization curve of rGO/NMC-312 composite exhibits a much lower overpotential and a greater current density, in comparison to that of the NMC-312 and rGO catalysts. It is very significant to compare the overpotential (η) required to reach a current density of 10 $mA \cdot cm^{-2}$, which is a metric relevant to solar fuel synthesis.[46] The overpotential of rGO/NMC-312 composite at a current density of 10 $mA \cdot cm^{-2}$ is as small as 320 mV, which is comparable to the η of state-of-the-art OER catalysts, e.g. IrO_2 and RuO_2.[47]

In contrast, the NMC-312 requires η = 410 mV, and the bare rGO exhibits no obvious current density change under a potential lower than 1.7 V. Thus, the excellent OER performance of rGO/NMC-312 ternary oxide composite is contributed to the synergistic effect between the reduced graphene oxide and Ni-Mn-Co ternary oxides. As a blank control measurement, glassy carbon electrodes barely show activity towards OER. Moreover, the OER performance of the rGO/Co_3O_4 sample synthesized by the same protocol as rGO/NMC materials was also examined. The rGO/Co_3O_4 sample shows a much lower OER activity than the rGO/NMC-312 sample, which needs an overpotential value of 410 mV to achieve a current density of 10 $mA \cdot cm^{-2}$. The distinct difference in OER activities confirms the role of Ni and Mn in the ternary oxide materials. In addition, replacement of Co with the foreign elements provides a feasible strategy to eliminate the high cost and contamination caused by Co. The optical photographs in the inset of **Figure 3.8d** show the generation of oxygen bubbles along with time on the rGO/NMC-312 composite modified electrode surface, revealing the production of oxygen gas. The OER kinetics parameters of the above catalysts were investigated by Tafel plots, which involves plotting overpotential against log

current density. As shown in **Figure 3.8b**, the Tafel slopes for rGO/NMC-312 composite, NMC-312 catalyst, rGO, IrO_2/C, and RuO_2/C catalyst were found to be ~58, ~151, ~129, ~96, and 55 mV dec^{-1}, respectively. The small Tafel slope of rGO/NMC-312 composite (58 mV dec^{-1}) indicates the comparatively fast electron transport and excellent OER catalytic kinetics. In addition to Tafel plots, turnover frequency (TOF) is also a critical factor to evaluate the intrinsic activity of a catalyst. TOF represents the number of oxygen molecules evolved per second per active site,[48,49] which provides valuable insight about the per-site activity of a catalyst.[50,51] The TOF value of the rGO/NMC-312 at a OER overpotential of 350 mV was calculated to be ~2.6×10^{-1} s^{-1}, assuming all the metal atom sites contribute to the activities. This value is 20 times higher than that of the state-of-the-art OER catalyst RuO_2.[48]

The electrochemical impedance spectroscopy measurements (EIS) were carried out under OER reaction conditions to investigate the ionic and charge transport rate during the OER process (**Figure 3.8c**). The semicircles in the high-frequency range of the Nyquist plot are ascribed to charge-transfer resistance, which is comparable for all catalysts.[23] The values are related to the electrocatalytic kinetics, and a lower value reflects a faster electron transfer rate. The fitted equivalent circuit was used to obtain the charge transfer resistances (R_{ct}) of each catalyst. R_{ct} values increase in the order of rGO > NMC-312 > rGO/NMC-312, which correlated well with the OER activity of each material. To further assess the durability of the catalyst, chronopotentiometry was carried out in a long-term test at a current density of 10 mA·cm^{-2} in 0.1 M KOH solution at a rotation speed of 1600 rpm. As illustrated in **Figure 3.8d**, rGO/NMC-312 composite shows remarkable electrochemical stability, as the required overpotential to reach a current density of 10 mA·cm^{-2} was maintained at a constant value for more than 24 hours.

3.3.4 HER Electrocatalytic Performance of As-converted rGO/NMC-312 Ternary Sulfide Composites

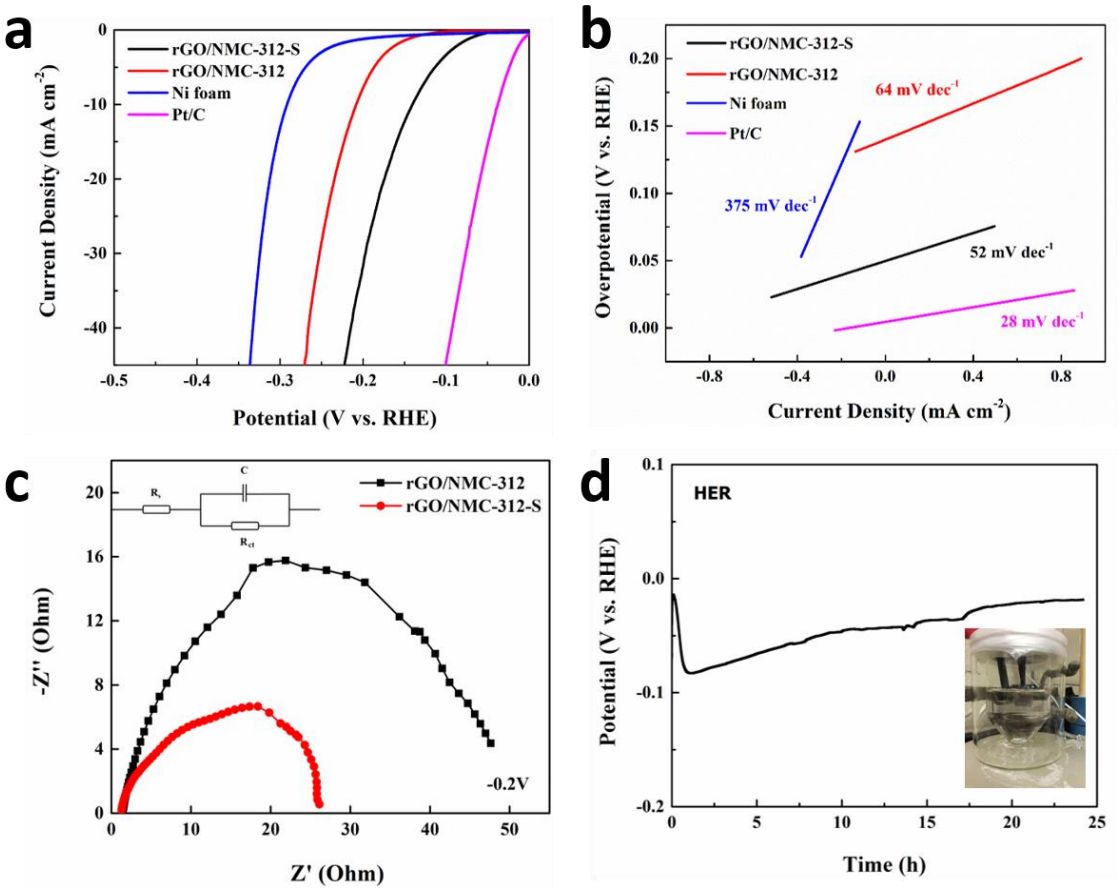

Figure 3.9 HER electrocatalytic performances. (a) Polarization curves and (b) Tafel plots of different catalysts on Ni foam in 0.1 M KOH at a scan rate of 10 mV/s; (c) Nyquist plots of rGO/NMC-312 ternary oxide composites and as-converted rGO/NMC-312 ternary sulfide composites at an overpotential of 200 mV. Inset: the fitted equivalent circuit; (d) Chronopotentiometry curve of the as-converted rGO/NMC-312 ternary sulfide composites at a constant current density of 10 $mA \cdot cm^{-2}$. Inset: photographs showing generation of hydrogen bubbles on the as-converted rGO/NMC-312 ternary sulfide composite on Ni foam (1×1 cm) (All tests are for HER).

Compared to rGO/NMC-312 ternary oxide composites, the as-converted rGO/NMC-312 ternary sulfide composites should present higher catalytic activity toward the hydrogen evolution reaction due to their smaller particle sizes and rougher surface. To confirm this idea, we evaluated the HER electrocatalytic performance of the as-converted rGO/NMC-312 ternary sulfide composites in an alkaline solution using a typical three electrode system. The as-converted rGO/NMC-312 ternary sulfide composites were dipped onto Ni foam and used as the working electrode (catalyst loading ~0.53 mg·cm^{-2}). For comparison, bare Ni foam, commercial 20 wt% Pt/C, and rGO/NMC-312 ternary oxide composites were also studied under the same conditions. **Figure 3.9a** shows the HER polarization curves obtained from linear sweep voltammetry measurements (LSV). The bare Ni foam exhibits poor HER activity in the range of measurement potential; a large overpotential is required to reach a current density of 10 mA·cm^{-2}. The rGO/NMC-312 ternary oxide composites showed an enhanced activity compared to bare Ni form, while the as-converted rGO/NMC-312 ternary sulfide composites achieve a current density of 10 mA·cm^{-2} at a significantly low overpotential of ~151 mV versus RHE. This value is superior to that of most noble metal-free HER electrocatalysts.[10,23,52] As shown in the inset of **Figure 3.9d**, vigorous bubbling on the surface of Ni foam shown in the optical photograph during the measurement. To better understand the intrinsic properties of the electrocatalyst, the polarization curves were interpreted by making Tafel plots, as shown in **Figure 3.9b**. The as-converted rGO/NMC-312 ternary sulfide composites exhibit the lowest Tafel slope of 52 mV dec^{-1} in the low overpotential range compared to bare Ni form (~357 mV dec^{-1}) and rGO/NMC-312 ternary oxide composites (~64 mV dec^{-1}), which further confirmed the high catalytic activity. As a comparison, a Tafel test of the commercial Pt/C was also conducted under the same conditions. The resulting Tafel plot yields a Tafel slope of 28 mV dec^{-1}, which agrees well with the literature value.[53] The Tafel slope value of the as-converted rGO/NMC-312 ternary sulfide composites is also comparable to previously reported alkaline water splitting catalysts, such as CoP[54] and $NiSe_2$[55]. The exchange current density (j_0) increased with the

increase of the number of active sites, which is also an important factor to evaluate the catalytic activity.[56] The j_0 of each catalyst is calculated by an extrapolation method derived from the Tafel plots. In detail, the rGO/NMC-312-S yielded an exchange current density of 2.8×10^{-2} mA·cm^{-2}, and the rGO/NMC-312 yielded an exchange current density of 8.3×10^{-3} mA·cm^{-2}. The small Tafel slope and the low exchange current density for the rGO/NMC-312-S are superior to the previously reported Pt-free HER catalysts.[49,57,58] High surface area is a key factor affecting HER activities. According to the nitrogen sorption measurements, the as-converted rGO/NMC-312 ternary sulfide composites have a Brunauer−Emmett−Teller (BET) surface area of 57 m^2/g, which is lower than that of rGO/NMC-312 oxide composites (128 m^2/g). As explained before, the decrease in surface area of sulfides is attributed to the higher atomic weight per metal atom as compared to a corresponding oxide compound with same porosity. In addition to the electrode activity measurements, intrinsic activity measurements of a catalyst provide intense understanding of the electrocatalyst on a per-site basis. The per-site activity is quantified as turnover frequency (TOF), which is usually derived from the number of active sites. Effort has been devoted to estimate the total number of active sites, which is often related to the surface area of a catalyst.[51] However, the active surface area measured by N_2 sorption techniques can be overestimated. Thus, electrochemical active surface area is preferred for further investigating the per-site activity.

In order to investigate the electrochemical effective surface area (ECSA) of those two catalysts, double-layer capacitances (C_{dl}) were calculated via cyclic voltammetry in a non-Faradaic potential range. The rGO/NMC-312 ternary sulfide composites exhibit a C_{dl} of 25.2 mF·cm^{-2}, which is slightly higher than that of a rGO/NMC-312 oxide composite (20.5 mF·cm^{-2}) regardless of the reduced BET surface area. The results suggest that more exposed active sites toward HER can be obtained in rGO/NMC-312 ternary sulfide composites, due to a higher concentration of oxygen vacancies. Then, the turnover frequency (TOF) for each catalyst was calculated based on the above ECSA to evaluate the intrinsic activity. At a current density of 10 mA·cm^{-2}, the TOF of rGO/NMC-

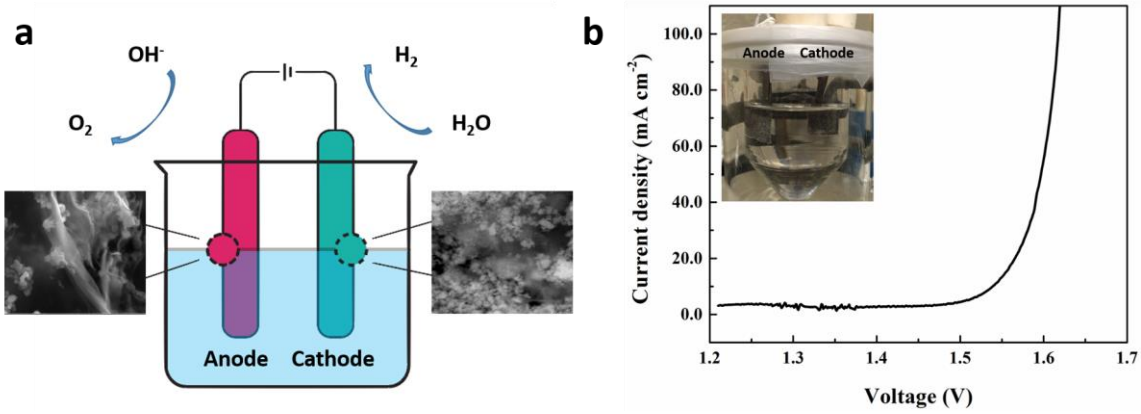

Figure 3.10 (a) Schematic representation of the overall water splitting reaction; (b) Polarization curve of the overall water splitting using rGO/NMC-312 ternary oxide composites and as-converted rGO/NMC-312 ternary sulfide composites as anode and cathode material, respectively, in 1 M KOH. Inset: Photographs showing the generation of oxygen and hydrogen bubbles on Ni foam.

---

312 sulfide composites and oxide composites were estimated to be 1.6×10^{-1} s^{-1} and 1.5×10^{-1} s^{-1}, respectively. The above values are comparable to the recently reported superior Co-based HER catalysts, such as CP/CTs/Co-S (TOF = 1.2×10^{-1} s^{-1} at $j > 10$ $mA \cdot cm^{-2}$).[53]

The electrode kinetics under HER operating conditions were further investigated by electrochemical impedance spectroscopy (EIS). The frequency-dependence of this impedance can reflect intrinsic chemical properties. The EIS measurements were conducted over a frequency range from 100 kHz to 0.01 Hz at an overpotential of 200 mV. The EIS data were fitted into an equivalent circuit, as shown in the inset of **Figure 3.9c**. The charge transfer resistance (R_{ct}) can be obtained from the semicircle in the high-frequency range of the Nyquist plot. The R_{ct} value for the as-converted rGO/NMC-312 ternary sulfide composite is about 29 **Ω**, which is lower than that of the corresponding oxide composite (47 **Ω**), suggesting a faster electron transfer rate and a more favorable HER kinetics at the as-converted rGO/NMC-312 ternary sulfide composite electrode. To examine the durability of the as-converted HER catalyst, we carried out chronopotentiometric measurements. As shown in **Figure 3.9d**, the overpotential needed to achieve a current density of 10 $mA \cdot cm^{-2}$ increased in the first hour followed by continuous decreasing within the rest of the 23

h test. In summary, the rGO/NMC-312-S composites show a high current density, a low overpotential at a constant current density, a small Tafel slope, and good electrochemical durability under alkaline conditions.

Based on the above results, the rGO/NMC-312 ternary oxide composites and their as-converted sulfide composites possess high OER and HER efficiency under alkaline conditions, respectively. Furthermore, we performed the overall water splitting in an alkaline solution (1 M KOH) using a two-electrode system by applying the rGO/NMC-312 ternary oxide composites as the oxygen evolution catalyst and the as-converted rGO/NMC-312 ternary sulfide composites as the hydrogen evolution catalyst (**Figure 3.10a**). This cell requires 1.56 V to achieve a current density of 20 $mA \cdot cm^{-2}$ in water electrolysis. Considerable oxygen and hydrogen bubbles on Ni foam are observed (Inset of **Figure 3.10b**). Ni foam acts as a high surface area support, which benefits the contact between electrocatalyst and electrolyte.[59]

3.4 Discussion

In an electrochemical catalytic system, the physicochemical properties of the catalyst will have significant effect on the catalytic activities, such as morphologies, crystal structures, and surface areas. In addition, mixed valent states also significantly influence the catalyst performance in this ternary oxide system. Typically, in the process of oxygen evolution reactions, Co II species are being oxidized to Co III species along with increasing anodic potential. The formation of CoOOH species is the rate-determining step in the OER process. The Co III species are considered to be the active sites for OER. Since Ni is more electronegative than Co, Ni might be able to facilitate the oxidation of Co II to Co III.[60] The chemical composition of the rGO/NMC-312 ternary oxide composites is revealed by XPS analysis (**Figure 3.3**). The results from deconvoluted Co 2p and Ni 2p spectrum show a full substitution of Co^{2+} by Ni^{2+}, which contributes to a good OER activity. Since the incorporation of Ni in spinel Co_3O_4 results in a higher electronegativity, which makes the adsorption of OH^- more favorable during the OER process.[8] The good electrochemical

performance was also favored by the existence of carbonaceous species. Most of the metal oxides possess low electric conductivity that limits the electron transport through the active sites. As graphene sheets with high surface area serve as a good supporting matrix in the composite material, such structure ensured an enhanced mechanical strength and a promoted chemical durability.[61–64] The homogeneously distributed NMC-312 ternary oxide on high surface area reduced graphene oxide sheets favored the more efficient use of active sites of the electrocatalyst. The high conductivity of reduced graphene oxide enabled a faster electron transfer process. To verify the synergistic effect between rGO and the ternary oxide, the rGO without NMC spinel oxide was examined as an OER electrocatalyst in alkaline conditions. This material shows negligible activity towards OER, which indicates the GO itself may not act as an active site. However, the strong electrical and chemical coupling between graphene and NMC-312 causes a synergistic effect between rGO and NMC spinel oxides or sulfides, which contributes to the superior catalytic efficiency for OER and HER. Compared to the bulk single metal oxide materials, the reduced crystal size of ternary oxides also contributed to the good electrochemical performance. In addition to the size effect, the excellent dispersibility of the nanoparticles might also offer significant advantages in the further fabrication of different electrode architectures.[16]

To better understand the HER mechanism, we performed electrochemical impedance studies to evaluate the intrinsic properties of the rGO/NMC-312 oxide and sulfide composites. The charge transfer resistance (R_{ct}) value is related to the electrocatalytic kinetics, charge transfer rate, e.g. Generally, the smaller the R_{ct} value, the faster the HER rate. As shown in **Figure 3.9c**, the rGO/NMC-312 sulfide composite exhibits a smaller R_{ct} value (29 **Ω**) than its corresponding oxide composite (47 **Ω**), suggesting a higher electrical conductivity. The corresponding Tafel plots (overpotential vs. log j) was obtained to determine the HER kinetics of the catalysts. The Tafel

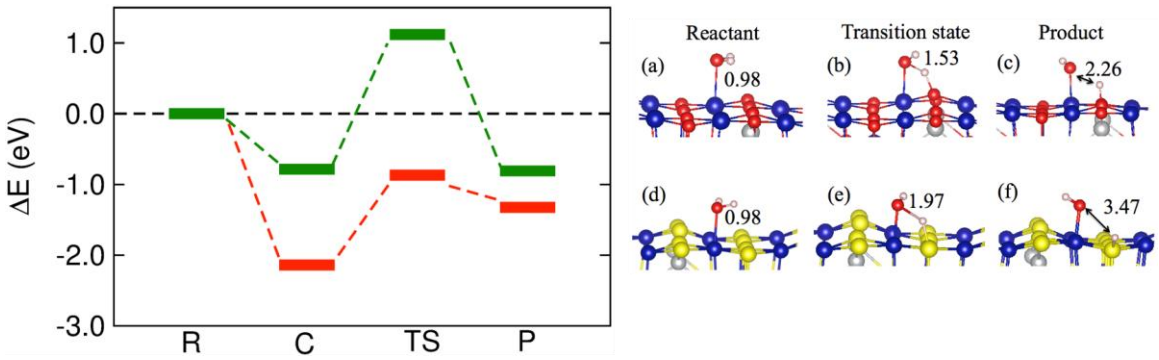

Figure 3.11 Left: Reaction pathways for the O-H bond breaking of water on spinel sulfide (red line) and oxide (green line) surfaces. R, C, TS and P represent the reactant, reactant complex, transition state and the product, respectively. ΔE: The energy difference of R, C, TS and P with respect to the combined energy of the separated species (Here separated species means the spinel surface and the H_2O molecule). Right: Optimized geometries of reactant complex, transition state and product for (a-c) spinel oxide; (d-f) spinel sulfide. Only parts of the surfaces are shown for a better view. The digits indicate the stretched O-H bond distances in Å.

slope value is a useful indicator of the HER reaction rates and mechanism pathways, which can be determined by fitting the Tafel plots to the Tafel equation ($\eta = b \log j + a$, where b is the Tafel slope and j is the current density).[59] For a completed HER process, there are different mechanism pathways under alkaline conditions. The adsorption of water molecules is involved in both pathways. This is followed by a direct combination of two H_{ads} to release H_2 (Volmer-Tafel pathway, as shown in Equation 1) or generation of H_2 by combination with another proton source and electrons (Volmer-Heyrovsky pathway, as shown in Equation 2). Under alkaline conditions, the HER process with Pt/C occurs via a fast Volmer-Tafel pathway, as indicated by the measured Tafel slope (28 mV dec^{-1}). As shown in **Figure 3.9b**, a Tafel slope of 52 mV dec^{-1} is observed for the as-converted rGO/NMC-312 ternary sulfide composites. The value suggests that the HER process follows the Volmer-Heyrovsky mechanism. In general, a lower Tafel slope shows that lower overpotential is needed to reach a required current density.[12]

Equation 1:

$$H_2O_{(l)} + e^- \rightarrow H_{ads} + OH^-_{(aq)} \, (Volmer)$$

$$H_{ads} + H_{ads} \rightarrow H_{2(g)} (Tafel)$$

Equation 2:

$$H_2O_{(l)} + e^- \rightarrow H_{ads} + OH^-_{(aq)} (Volmer)$$

$$H_{ads} + H_2O_{(l)} + e^- \rightarrow H_{2(g)} + OH^-_{(aq)} (Heyrovsky)$$

We carried out DFT calculations on both the rGO/NMC-312 oxide and sulfide to gain deeper insight into the surface structure and reaction pathway.[65] To simplify the calculation process, we only included Co and Ni in both oxide and sulfide materials. In the DFT calculations, we let an H_2O molecule be adsorbed at three critical sites of the spinel surfaces; these sites are on the sulfur or oxygen site (A), on the Co site (B) and the interstitial site (C). Our calculations indicate that the water molecule is adsorbed in the order (E(B): E(C): E(A) = 0.0: 1.83: 1.88 eV) for the sulfide surface, while on the oxide surface the energy ordering is (E(A): E(B): E(C) = 0.0: 0.59: 0.87 eV). The low energy configuration for the sulfide surface has water molecules adsorbed on Co atoms with the oxygen atoms of water forming a bond with the Co atoms of the surface while for oxide surfaces, water adsorbs on the oxygen atoms with one of the H atoms pointing towards the oxygen atoms on the surface.

The reaction pathways are studied for the case where the water molecule is adsorbed on the Co atoms for both surfaces. **Figure 3.11** shows the reaction pathways for both surfaces (top panel) and the corresponding geometries along the reaction pathway (**Figure 3.11a-f**). The activation barriers calculated from Eq. (2) for the O-H bond breaking on sulfide and oxide surfaces are found to be 1.27 eV and 1.90 eV, respectively. ETS from Eq. (3) is calculated to be -0.87 eV and 1.12 eV, respectively. Our calculations show that the O-H bond of water molecules could break more

readily (low EA) on sulfide surfaces than the oxide surfaces. This indicates a high preferability of the HER reaction for sulfide surfaces. This finding agrees well with the experimental results where a high activity is found for spinel sulfides. This result is further supplemented by the binding energies where the initial binding of water molecule is high on a sulfide surface (2.14 eV) as compared to that of the oxide surface (0.78 eV). To gain further insight into the reaction mechanism, single hydrogen atom binding energies on both surfaces are studied and are found to be 2.19 eV and 3.56 eV for sulfide and oxide surfaces, respectively. This suggests that the hydrogen atoms are weakly bound on sulfide surfaces leading to an easy desorption as compared to oxide surfaces. Therefore, sulfide surfaces can be projected as a better candidate for the HER reaction as compared to oxide surfaces.

3.5 Conclusions

In summary, we demonstrated a facile synthesis strategy for the preparation of reduced graphene oxide supported ternary oxide composites and corresponding sulfide composites, which exhibit excellent OER and HER activity in alkaline media, respectively. For OER, the rGO supported ternary spinel oxide composites offer a superior catalytic activity with a low overpotential of 320 mV at a current density of 10 $mA \cdot cm^{-2}$ and exhibit remarkable electrochemical durability for 24 h under continuous operation under alkaline conditions. For HER, rGO supported ternary sulfide composites show a significantly low overpotential of ~151 mV at a current density of 10 $mA \cdot cm^{-2}$ with a mass loading of 0.53 $mg \cdot cm^{-2}$, and a small Tafel slope of 52 mV/decade. With the help of DFT calculation results, sulfide surfaces serve as a better candidate for the HER reaction as compared to oxide surfaces due to suitable energetics for the O-H bond breakage and H_2 desorption. When rGO/NMC-312 oxides and sulfides served as alkaline water electrolysis anodes and cathodes, respectively, a voltage of 1.56 V is required to reach 20 $mA \cdot cm^{-2}$ at room

temperature. Versatile nonprecious electrodes were exploited as anodes and cathodes, in which the spinel oxide anodes can be converted to cathode materials in a facile protocol, facilitating the overall water splitting process. This facile conversion route offers new avenues for the design of highly effective ternary oxide or sulfide electrocatalysts with multiple valent states, thus promoting the development of clean energy conversion technologies.

3.6 References

(1) Yang, H.; Zhang, Y.; Hu, F.; Wang, Q. *Nano Lett.* **2015**, *15* (11), 7616–7620.

(2) Gao, M.; Sheng, W.; Zhuang, Z.; Fang, Q.; Gu, S.; Jiang, J.; Yan, Y. *J. Am. Chem. Soc.* **2014**, *136* (19), 7077–7084.

(3) Trotochaud, L.; Young, S. L.; Ranney, J. K.; Boettcher, S. W. *J. Am. Chem. Soc.* **2014**, *136* (18), 6744–6753.

(4) Lee, Y.; Suntivich, J.; May, K. J.; Perry, E. E.; Shao-horn, Y. *J. Phys. Chem. Lett.* **2012**, *3*, 399–404.

(5) Gong, M.; Li, Y.; Wang, H.; Liang, Y.; Justin, Z.; Zhou, J.; Wang, J.; Regier, T.; Wei, F.; Dai, H.; Wu, J. Z. *J. Am. Chem. Soc.* **2013**, *135*, 8452–8455.

(6) Gao, M.; Xu, Y.; Jiang, J.; Zheng, Y.; Yu, S. *J. Am. Chem. Soc.* **2012**, *134* (103), 2930–2933.

(7) Duan, J.; Chen, S.; Jaroniec, M.; Qiao, S. Z. *ACS Nano* **2015**, *9* (1), 931–940.

(8) Yeo, B. S.; Bell, A. T. *J. Am. Chem. Soc.* **2011**, *133* (14), 5587–5593.

(9) Kuo, C.-H.; Mosa, I. M.; Poyraz, A. S.; Biswas, S.; El-Sawy, A. M.; Song, W.; Luo, Z.; Chen, S.-Y.; Rusling, J. F.; He, J.; Suib, S. L. *ACS Catal.* **2015**, *5*, 1693–1699.

(10) McCrory, C. C. L.; Jung, S.; Ferrer, I. M.; Chatman, S. M.; Peters, J. C.; Jaramillo, T. F. *J. Am. Chem. Soc.* **2015**, *137* (13), 4347–4357.

(11) Li, R.; Wei, Z.; Gou, X. *ACS Catal.* **2015**, *5*, 4133–4142.

(12) Zhou, X.; Liu, Y.; Ju, H.; Pan, B.; Zhu, J.; Ding, T.; Wang, C.; Yang, Q.; Zhou, X.; Liu, Y.; Ju, H.; Pan, B.; Zhu, J.; Ding, T.; Wang, C.; Yang, Q. *Chem. Mater.* **2016**, *28*, 1838–1846.

(13) Lu, Y.; Xu, Z.; Gasteiger, H. *J. Am. Chem. Soc.* **2010**, *132*, 12170–12171.

(14) Chen, S.; Duan, J.; Jaroniec, M.; Qiao, S. Z. *Angew. Chemie - Int. Ed.* **2013**, *52* (51), 13567–13570.

(15) Khakpash, N.; Simchi, A.; Jafari, T. *J. Mater. Sci. Mater. Electron.* **2012**, *23*, 659–667.

(16) Fominykh, K.; Chernev, P.; Zaharieva, I.; Sicklinger, J.; Stefanic, G.; DoBlinger, M.; Mu, A.; Pokharel, A.; Bo, S.; Scheu, C.; Bein, T.; Fattakhova-rohlfing, D. *ACS Nano* **2015**, *9* (5), 5180–5188.

(17) Shen, M.; Ruan, C.; Chen, Y.; Jiang, C.; Ai, K.; Lu, L. *ACS Appl. Mater. Interfaces* **2015**, *7* (2), 1207–1218.

(18) Liu, Y.; Cheng, H.; Lyu, M.; Fan, S.; Liu, Q.; Zhang, W.; Zhi, Y.; Wang, C.; Xiao, C.; Wei, S.; Ye, B.; Xie, Y. *J. Am. Chem. Soc.* **2014**, *136*, 15670–15675.

(19) Li, Y.; Hasin, P.; Wu, Y. *Adv. Mater.* **2010**, *22* (17), 1926–1929.

(20) Dutta, B.; Biswas, S.; Sharma, V.; Savage, N. O.; Alpay, S. P.; Suib, S. L. *Angew. Chemie - Int. Ed.* **2016**, *55* (6), 2171–2175.

(21) Liu, X.; Chang, Z.; Luo, L.; Xu, T.; Lei, X.; Liu, J.; Sun, X. *Chem. Mater.* **2014**, *26* (5), 1889–1895.

(22) Chellam, U.; X, Z. P.; Z, H. C. *Chem. Mater.* **2000**, *12*, 650–658.

(23) Jin, H.; Wang, J.; Su, D.; Wei, Z.; Pang, Z.; Wang, Y. *J. Am. Chem. Soc.* **2015**, *137* (7), 2688–2694.

(24) Mohamed, S. G.; Tsai, Y.-Q.; Chen, C.-J.; Tsai, Y.-T.; Hung, T.-F.; Chang, W.-S.; Liu, R.-S. *ACS Appl. Mater. Interfaces* **2015**, *7* (22), 12038–12046.

(25) Li, L.; Zhang, Y.; Shi, F.; Zhang, Y.; Zhang, J.; Gu, C.; Wang, X.; Tu, J. *ACS Appl. Mater. Interfaces* **2014**, *6*, 18040–18047.

(26) Chi, B.; Li, J.; Han, Y.; Chen, Y. *J. Phys. Chem. C* **2014**, *118*, 25939–25946.

(27) Li, D.; Baydoun, H.; Verani, C. N.; Brock, S. L. *J. Am. Chem. Soc.* **2016**, *138* (12), 4006–4009.

(28) Luo, Z.; Poyraz, A. S.; Kuo, C.; Miao, R.; Meng, Y.; Chen, S.; Jiang, T.; Wenos, C.; Suib, S. L. *Chem. Mater.* **2015**, *27*, 6–17.

(29) Zhang, Z.; Lim, S. H.; Li, B.; Wang, X.; Liu, Z. *ACS Appl. Mater. Interfaces* **2014**, *6*, 12684–12691.

(30) Liang, Y.; Li, Y.; Wang, H.; Zhou, J.; Wang, J.; Regier, T.; Dai, H. *Nat. Mater.* **2011**, *10* (10), 780–786.

(31) Mao, S.; Wen, Z.; Huang, T.; Hou, Y.; Chen, J. *Energy Environ. Sci.* **2014**, *7* (2), 609–616.

(32) Jafari, T.; Moharreri, E.; Amin, A.; Miao, R.; Song, W.; Suib, S. *Molecules* **2016**, *21* (7), 900.

(33) Arcibar-Orozco, J. A.; Wallace, R.; Mitchell, J. K.; Bandosz, T. J. *Langmuir* **2015**, *31* (9), 2730–2742.

(34) Zhang, F.; Song, Y.; Song, S.; Zhang, R.; Hou, W. *ACS Appl. Mater. Interfaces* **2015**, *7* (13), 7251–7263.

(35) Hummers, W. S.; Offeman, R. E. *J. Am. Chem. Soc.* **1958**, *80* (6), 1339–1339.

(36) Wang, H.; Robinson, J. T.; Li, X.; Dai, H. *J. Am. Chem. Soc.* **2009**, *131* (29), 9910–9911.

(37) Miao, R.; Luo, Z.; Zhong, W.; Chen, S.-Y.; Jiang, T.; Dutta, B.; Nasr, Y.; Zhang, Y.; Suib, S. L. *Appl. Catal. B Environ.* **2016**, *189*, 26–38.

(38) Ferrari, A. C. *Solid State Commun.* **2007**, *143* (1–2), 47–57.

(39) Pahalagedara, M. N.; Pahalagedara, L. R.; He, J.; Miao, R.; Gottlieb, B.; Rathnayake, D.; Suib, S. L. *J. Catal.* **2016**, *336*, 41–48.

(40) Lin, Z.; Yao, Y.; Li, Z.; Liu, Y.; Li, Z.; Wong, C.-P. *J. Phys. Chem. C* **2010**, *114*, 14819–14825.

(41) Jung, I.; Field, D. a; Clark, N. J.; Zhu, Y. W.; Yang, D. X.; Piner, R. D.; Stankovich, S.; Dikin, D. a; Geisler, H.; Ventrice, C. a; Ruoff, R. S. *J. Phys. Chem. C* **2009**, *113*, 18480–18486.

(42) Zhu, J.; He, J. *ACS Appl. Mater. Interfaces* **2012**, *4*, 1770–1776.

(43) Ganesan, P.; Prabu, M.; Sanetuntikul, J.; Shanmugam, S. *ACS Catal.* **2015**, *5* (6), 3625–3637.

(44) Yonemoto, B. T.; Hutchings, G. S.; Jiao, F. *J. Am. Chem. Soc.* **2014**, *136*, 8895–8898.

(45) Pahalagedara, L. R.; Poyraz, A. S.; Song, W.; Kuo, C.-H.; Pahalagedara, M. N.; Meng, Y.-T.; Suib, S. L. *Chem. Mater.* **2014**, *26* (22), 6613–6621.

(46) Gao, M.-R.; Cao, X.; Gao, Q.; Xu, Y.-F.; Zheng, Y.-R.; Jiang, J.; Yu, S.-H. *ACS Nano* **2014**, *8* (4), 3970–3978.

(47) Gorlin, Y.; Jaramillo, T. F. *J. Am. Chem. Soc.* **2010**, *132* (39), 13612–13614.

(48) Sun, T.; Xu, L.; Yan, Y.; Zakhidov, A. A.; Baughman, R. H.; Chen, J. *ACS Catal.* **2016**, *6*, 1446–1450.

(49) Benson, J.; Li, M.; Wang, S.; Wang, P.; Papakonstantinou, P. *ACS Appl. Mater. Interfaces* **2015**, *7*, 14113–14122.

(50) Wang, J.; Wang, W.; Wang, Z.; Chen, J. G.; Liu, C. *ACS Catal.* **2016**, *6*, 6585–6590.

(51) Benck, J. D.; Hellstern, T. R.; Kibsgaard, J.; Chakthranont, P.; Jaramillo, T. F. *ACS Catal.* **2014**, *4*, 3957–3971.

(52) Lee, S. C.; Benck, J. D.; Tsai, C.; Park, J.; Koh, A. L.; Abild-Pedersen, F.; Jaramillo, T. F.; Sinclair, R. *ACS Nano* **2016**, *10*, 624–632.

(53) Wang, J.; Zhong, H.; Wang, Z.; Meng, F.; Zhang, X. *ACS Nano* **2016**, *10*, 2342–2348.

(54) Chang, J.; Xiao, Y.; Xiao, M.; Ge, J.; Liu, C.; Xing, W. *ACS Catal.* **2015**, *5*, 6874–6878.

(55) Liang, H.; Li, L.; Meng, F.; Dang, L.; Zhuo, J.; Forticaux, A.; Wang, Z.; Jin, S. *Chem. Mater.* **2015**, *27* (16), 5702–5711.

(56) Huynh, M.; Shi, C.; Billinge, S. J. L.; Nocera, D. G. *J. Am. Chem. Soc.* **2015**, *137*, 14887–14904.

(57) Zou, X.; Huang, X.; Goswami, A.; Silva, R.; Sathe, B. R.; Asefa, T. *Angew. Chemie Int. Ed.* **2014**, *53*, 4372–4376.

(58) Zhang, S.; Chowdari, B. V. R.; Wen, Z.; Jin, J.; Yang, J.; Academy, C. *ACS Nano* **2015**, *9* (12), 12464–12472.

(59) Luo, Z.; Miao, R.; Huan, T. D.; Mosa, I. M.; Poyraz, A. S.; Zhong, W.; Cloud, J. E.; Kriz, D. A.; Thanneeru, S.; He, J.; Zhang, Y.; Ramprasad, R.; Suib, S. L. *Adv. Energy Mater.* **2016**, *6*, 1600528.

(60) Subbaraman, R.; Tripkovic, D.; Chang, K.-C.; Strmcnik, D.; Paulikas, A. P.; Hirunsit, P.; Chan, M.; Greeley, J.; Stamenkovic, V.; Markovic, N. M. *Nat. Mater.* **2012**, *11* (6), 550–557.

(61) Ma, W.; Ma, R.; Wang, C.; Liang, J.; Liu, X.; Zhou, K. *ACS Nano* **2015**, *9* (2), 1977–1984.

(62) Li, X.; Wang, H.; Robinson, J. T.; Sanchez, H.; Diankov, G.; Dai, H. *J. Am. Chem. Soc.* **2009**, *131* (43), 15939–15944.

(63) Long, X.; Li, J.; Xiao, S.; Yan, K.; Wang, Z.; Chen, H.; Yang, S. *Angew. Chemie - Int. Ed.* **2014**, *53* (29), 7584–7588.

(64) He, J.; Liu, Y.; Meng, Y.; Sun, X.; Biswas, S.; Shen, M.; Luo, Z.; Miao, R.; Zhang, L.; Mustain, W. E.; Suib, S. L. *RSC Adv.* **2016**, *6* (29), 24320–24330.

(65) de Chialvo, M. R. G.; Chialvo, A. C. *J. Electroanal. Chem.* **1994**, *372* (1–2), 209–223.

Chapter 4. Mesoporous FeS_2 Material for Highly Efficient Electrocatalytic Hydrogen Evolution

4.1 Introduction

Increasing environmental issues and depletion of fossil fuels has motivated intense research on the alternative clean and sustainable energy carrier.[1] Hydrogen has been regarded as a promising energy carrier by virtue of its high energy density and zero-emission merit when burned with oxygen.[2] Electrocatalytic hydrogen evolution reaction (HER) is one of the most appealing approaches to extract molecular hydrogen from water.[3,4] Currently, Pt-based materials are regarded as the most efficient electrocatalysts for HER.[5] However, the low abundance and high cost limit their widespread applications.[6] One challenging issue in this pursuit is the development of energy- and cost-efficient catalysts that can be applied in this process.

In pursuit of an inexpensive alternative to Pt as the HER electrocatalyst, a great deal of effort has been made. Metal chalcogenides, which contain only non-precious, transition metals, are considered as a class of very promising candidates for HER due to their high abundance, low cost, high conductivity, thermal and mechanical stability.[7,8] Metal chalcogenides, MoS_2,[9] WS_2,[10] $CoSe_2$,[11] $NiSe_2$,[12] have been investigated widely as HER electrocatalysts over the past decades. Surprisingly, iron sulfide materials have rarely been investigated as HER electrocatalysts, and none have shown superior performance without further modifications.[13,14] Iron sulfide is an earth abundant and environmentally friendly semiconductor, which received resurgent interest for energy conversion applications in the past few years.[15,16] The practical applications of iron sulfide as HER cathode material are limited by their low surface area and few active sites. Due to the volume contraction and low electronic affinity between metal and sulfur, synthesis of metal

sulfides with high surface area is extremely challenging.[17] Meanwhile, the mesoporous materials are of great interest in a variety of applications such as adsorptions, separations, catalysis, lithium-ion batteries, and fuel cells ever since the pioneer works done by Mobil researchers.[18] in electrochemical water-splitting catalysis due to their abundance of accessible mesopores and exposure of active sites, which can facilitate the charge transfer and product diffusion.[19,20] Our synthetic protocol reported here involves a facile inverse micelle sol-gel method. The resulting mesoporous metal oxide materials are named UCT materials (University of Connecticut mesoporous materials).[21] The inverse micelle sol-gel method used nonionic surfactant P123 as a soft template, which formed inverse micelles in a low pH condition. By varying the heat treatment conditions, the crystallinity and pore structural parameters can be tuned.

Herein, we synthesize a mesoporous pyrite FeS_2 nanoparticles via a facile two-step synthetic protocol including inverse micelle sol-gel method followed by low-temperature sulfurization treatment. The structure of the resulting FeS_2 material is studied via multiple characterization techniques. The as-prepared mesoporous FeS_2 nanoparticles material exhibit superior performance as a HER electrocatalyst with a low overpotential of ~96 mV at a current density of 10 $mA \cdot cm^{-2}$ with an active loading of 0.53 $mg \cdot cm^{-2}$ and exhibit remarkable electrochemical durability for 24 h under alkaline conditions.

4.2 Experimental Section

4.2.1 Chemicals

Iron nitrate nonahydrate (≥98%), poly-(ethylene glycol)-block-poly (propylene glycol)-block-poly-(ethylene glycol) with average Mn~5800, nitric acid (≥70%), 1-butanol (≥99.4%), sodium hydroxide (≥99.99%), 2-proponal, 5 wt% Nafion. All chemicals were used as received without further purification.

4.2.2 Synthesis of mesoporous iron oxide

In a typical synthesis, 0.01 mol iron nitrate nonahydrate (> 98%, purchased from Sigma-Aldrich) was dissolved in a solution containing 0.12 mol of 1-butanol, 0.019 mol of nitric acid, and 2×10-4 mol of P123 surfactant in a 150-mL beaker at room temperature with magnetic stirring. Then the obtained clear gel was placed in an oven running at 80 °C for 3 h. The resulting products was cooled and washed with ethanol for four times and then centrifuged. Finally, the powder is dried in a vacuum oven overnight. The dried powder was calcined at 150 °C for 12 h in static air, and further heated at 250 °C for 4 h, and then heated at 350 °C or 450 °C for 4 h. The resulting samples were denoted as UCT-Fe-X (X = 150, 250, 350, and 450).

4.2.3 Synthesis of mesoporous iron sulfide

The sulfurization experiments were carried out at 250 °C under atmospheric pressure. In each experiment, about 100 mg of as-prepared amorphous iron oxide and 200 mg sulfur powder was loaded into a quartz tubular reactor. Helium gas was flowed through the sulfurization set-up for a leak check. Then 1% H_2S/He was passed through the sample with a flow rate of 47 sccm. The sample was heated at 1 °C/min to 250 °C and held at this temperature for 12 h. The exhaust gas was bubbled through a lead nitrate solution to neutralize excess H_2S. The resulting sample was denoted as mseo FeS_2.

4.2.4 Materials Characterization

All the synthesized materials were ground to a fine powder in an agate mortar. The Powder X-ray diffraction (XRD) analysis was carried out at room temperature on a Rigaku Ultima IV diffractometer (Cu Kα radiation, λ = 1.5406 A). A beam voltage of 40 kV and a current of 44 mA were used. The morphologies of the materials were investigated using an FEI Nova SEM 450 with an accelerating voltage of 2.0 kV. Energy dispersive high-resolution transmission electron

microscopy (HR-TEM) images were collected using a Talos F200X microscope operating at 200 kV equipped with an Energy Dispersive Spectrometer (EDX). N_2 sorption measurements were performed on a Quantachrome Autosorb-1-1C automated sorption system. The samples were degassed at 150 °C for 6 h prior to the experiments. The surface areas were calculated by the Brunauer−Emmett−Teller (BET) method, and the pore size distributions were obtained by the Barrett−Joyner−Halenda (BJH) method from the desorption branch of the isotherms. Raman spectra were taken with a Renishaw 2000 Raman microscope with an Ar^+ ion laser (514 nm) as the excitation source. X-ray photoelectron spectroscopy (XPS) measurements were performed in a PHI Model 590 spectrometer with multiprobes (Al Kα radiation, λ = 1486.6 eV, operated at 250 W). The temperature programmed oxidation (TPO), and mass spectrometry were performed with a Thermolyne 79300 model tube furnace equipped with an MKS gas analyzer coupled with a quadrupole mass selective detector. The FeS_2 samples were packed in a quartz tube and then mounted in a tubular furnace. The loaded samples were pretreated with Ar flow for 1 h at 200 °C before the measurement. In a typical experiment, 10% vol. O_2/Ar gas mixtures were passed through the tube reactor at a constant flow rate in the temperature range of 35-700 °C at a heating ramp rate of 10 °C·min^{-1}.

4.2.5 Electrochemical Measurements

All the electrochemical measurements were performed in a three-electrode cell on a CHI 760E electrochemical workstation at room temperature. A platinum wire and a saturated calomel electrode (SCE) were used as a counter electrode and a reference electrode, respectively. The potentials reported in this work are referenced to the reversible hydrogen electrode (RHE). The HER measurements were carried out by using Ni foam (1×1 cm) covered with electrocatalysts as the working electrode, a graphite rod, and an SCE as a counter electrode and a reference electrode,

respectively. The working electrode was prepared as follows: 5 mg of catalyst sample and 40 μL of a 5 wt% Nafion solution was dispersed in 400 μL of a water/ethanol solvent mixture with a volume ratio of 1:3. The mixture catalyst ink was ultrasonicated for 30 min. Then 40 μL of the homogeneous suspension was dropped onto Ni foam and left air dry. The active loadings of catalyst were 0.53 $mg \cdot cm^{-2}$. The HER activity of the catalysts was evaluated using linear sweep voltammetry (LSV) in the potential window ranging from -0.5 to 0.0 V versus RHE. Electrochemical impedance spectroscopy (EIS) was carried out in 0.1 M KOH solution at an applied potential of -0.2 V (vs. RHE). The spectra were collected at an ac voltage of 5 mV with the frequency range from 0.01 to 100 kHz. Chronopotentiometry experiments were performed at a constant current density of 10 $mA \cdot cm^{-2}$. The potential window was set between -0.2 V and 0.0 V (vs. RHE), which falls in the HER active potential range. Note all the LSV and CV tests were 100% iR compensated.

4.3 Results

4.3.1 Comparison of physicochemical properties of as-prepared iron sulfide using mesoporous iron oxides calcined at different temperature as a precursor

To prepare mesoporous FeS_2, previously reported UCT mesoporous iron oxide materials were chosen as the precursor. In a typical synthetic procedure, the presence of nitrate ions facilitates the penetration of positively charged metal nitro-clusters into the inverse micelle followed by a thermal decomposition of nitrate ions into nitric oxide species, which controlled the sol-gel chemistry. The mesoporous structure is formed in a random fashion, where the mesopores are

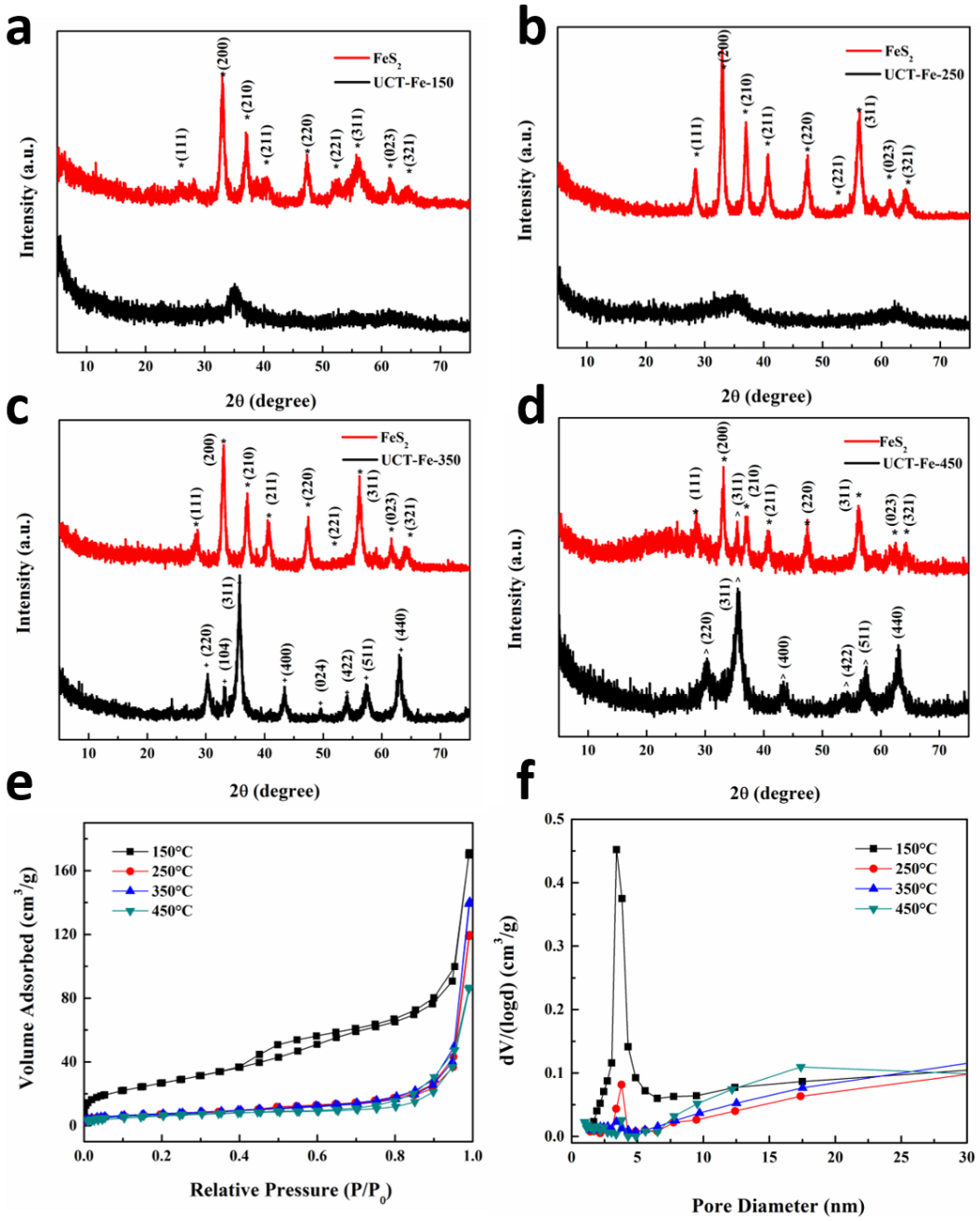

Figure 4.1 (a-d) XRD patterns of as-prepared FeS_2 materials using UCT-Fe-X (X = 150, 250, 350, and 450 °C) as a precursor. BET measurements: (e) N_2 sorption of isotherms and (f) BJH desorption pore size distribution of as-prepared FeS_2 materials using UCT-Fe-X (X = 150, 250, 350, and 450 °C) as a precursor. *, $^{+}$, and ^ stand for FeS_2, Fe_2O_3, and Fe_3O_4, respectively.

formed by the connected intraparticle voids. The mesoporous iron oxide samples were calcined at different temperatures and used as precursors for direct sulfurization process. The iron oxide materials are amorphous at low calcination temperatures (150 and 250 °C) and become crystalline at high temperatures (350 and 450 °C). Different physicochemical properties of the as-prepared FeS_2 are expected. **Figure 4.1a-d** show the XRD patterns of the as-prepared FeS_2 synthesized by using mesoporous iron oxide calcined at different temperatures. The XRD patterns of the FeS_2 synthesized from UCT-Fe-150, UCT-Fe-250, UCT-Fe-350, and UCT-Fe-450 confirm the pyrite FeS_2 structure. The as-prepared FeS_2 sample using UCT-Fe-150 as a precursor shows the lowest crystallinity, while it becomes more crystalline when treated at higher calcination temperatures. In addition, by using UCT-Fe-450 as a precursor, an impurity phase was observed in XRD patterns of the as-synthesized FeS_2. As shown in **Figure 4.1d**, a diffraction line located at 36° was presented corresponding to the (311) plane of Fe_3O_4.[22] In order to further confirm the trends found in the XRD results, N_2 sorption measurements were performed (**Figure 4.1e and f**). The FeS_2 synthesized from UCT-Fe-150 showed a characteristic Type IV N_2 adsorption isotherm with a Type I hysteresis loop, indicating the existence of regular mesoporous stricture.[23] This material exhibits much higher surface area (>100 $m^2 \cdot g^{-1}$) and larger pore volume (>0.20 $cm^3 \cdot g^{-1}$) than other samples. The Barrett-Joyner-Halenda (BJH) desorption pore size distribution shows a uniform mesoporous structure with a monomodal pore size of 3.4 nm. However, the nonporous nature was observed when the mesoporous iron oxide precursor calcined above 250 °C, and a dramatically decreased surface area for the as-synthesized FeS_2 materials is obtained. Above results further demonstrated the successful synthesis of mesoporous FeS_2 materials with expected high surface area and large pore size.

The crystalline phases were further identified by Raman due to a higher sensitivity. The two

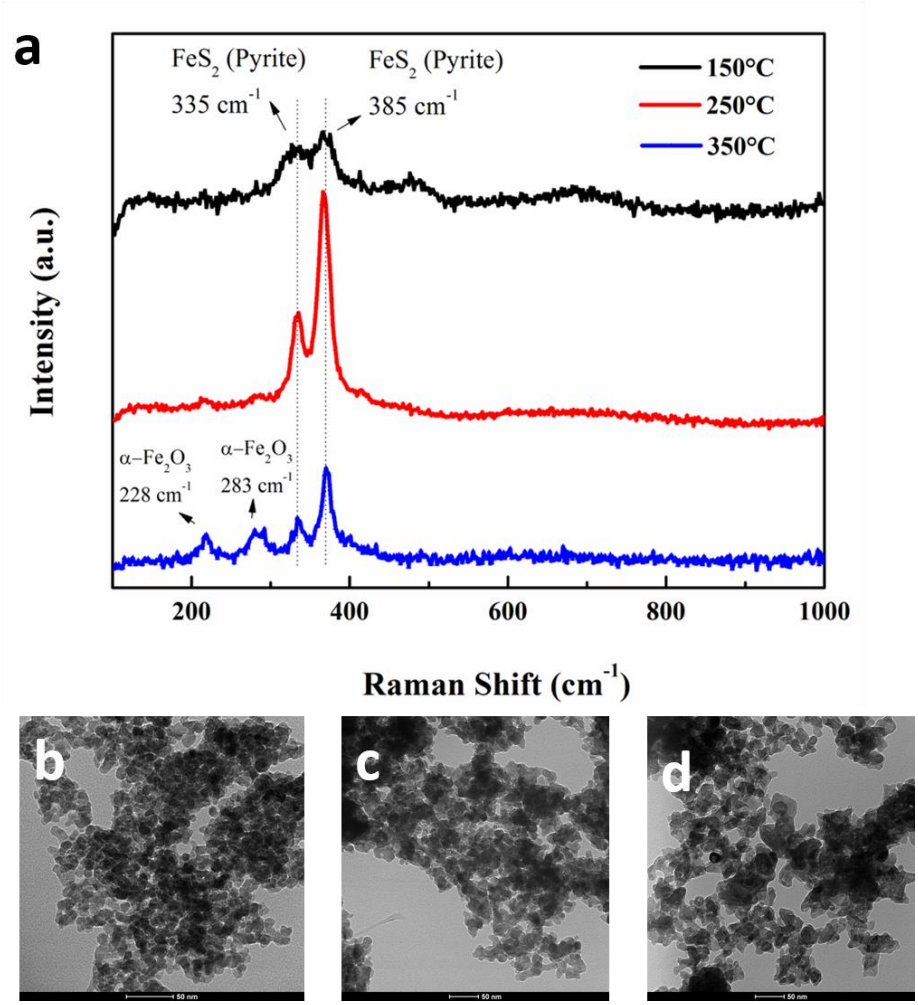

Figure 4.2 (a) Raman spectra for as-prepared FeS_2 materials using UCT-Fe-X (X = 150, 250, and 350 °C) as a precursor. TEM images of (b) as-prepared FeS_2 materials using UCT-Fe-150 as a precursor, (c) as-prepared FeS_2 materials using UCT-Fe-250 as a precursor, and (d) as-prepared FeS_2 materials using UCT-Fe-350 as a precursor.

characteristic vibrational modes of the pyrite phase at 335 cm^{-1} and 385 cm^{-1} were observed for all FeS_2 samples synthesized from UCT-Fe-150, UCT-Fe-250, and UCT-Fe-350. Increasing calcination temperature (150 to 250 °C) resulted in sharper vibrational bands, which indicated the higher crystallinity and larger particle grain sizes. The results indicate that the formation of a mesoporous structure is favored at low heat treatment conditions. Also, vibrational modes of the Fe_2O_3 phase appeared when the calcination temperature reached 350 °C, suggesting the presence of an impurity. The results are in consistent with the XRD observations. The morphology and mesoporous structure of the as-synthesized materials could be confirmed by TEM imaging (**Figure 2b-d**). The samples are spherical particles with a mean size of 20 nm. The FeS_2 sample synthesized from UCT-Fe-150 exhibits well-dispersed nanospheres without any aggregation, while the FeS_2 materials synthesized from UCT-Fe-250 and UCT-Fe-350 fail to show a uniform particle distribution due to the collapse of the mesoporous structure. In summary, by comparing the physicochemical properties of FeS_2 samples, mesoporous pyrite FeS_2 can be most easily synthesized by using mesoporous iron oxide sample that calcined at 150 °C.

4.3.2 Catalyst Characterization

The mesoporous FeS_2 composite materials were prepared by a sol-gel process followed by a gas phase sulfurization process. In a typical synthesis of mesoporous FeS_2 nanoparticles, the amorphous iron oxide was first obtained via an inverse micelle sol-gel method. The synthesized material was heated to 150 °C in static air to obtain the amorphous iron oxide structure and to remove the adsorbed carboxyl and nitrate species on the surface. Then, H_2S gas and sulfur powder were used as sulfur sources, which allowed for a facile chemical conversion from oxide to sulfide without damaging the mesoporous structure. The carboxyl and nitrate removal are further completed in the sulfurization process. The crystalline structure of pyrite FeS_2 was first confirmed

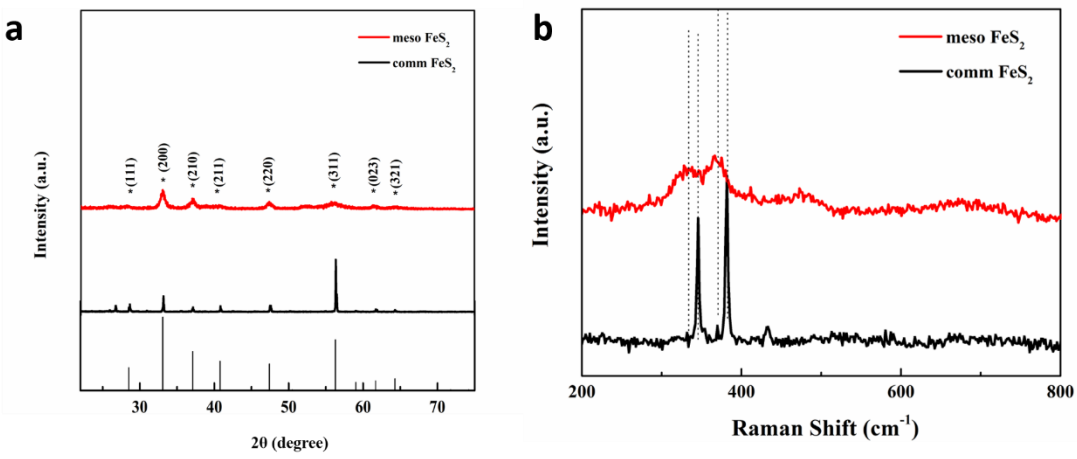

Figure 4.3 (a) XRD pattern of meso FeS_2, comm FeS_2, and the JCPDS pattern for standard pyrite. (b) Raman Spectra of meso FeS_2 and comm FeS_2.

---

by the X-ray diffraction (XRD) pattern. As shown in **Figure 4.3a**, the diffraction pattern of the mesoporous FeS_2 can be indexed to the cubic phase of pyrite FeS_2 (JCPDS No. 42-1340), suggesting successful conversion of Fe_2O_3 into FeS_2. The commercial FeS_2 (comm FeS_2) also exhibits the pyrite phase, but with different crystallinity degree. The much lower crystallinity of the mesoporous FeS_2 may be due to the existence of the mesoporous structure, which destroyed the structural order over long distances.[24] The phase purity of the pyrite samples was further characterized by Raman spectroscopy (**Figure 4.3b**). The two peaks associated with the vibrational modes of the pyrite phase at 335 and 385 cm^{-1} are observed for both samples. In contrast to the sharp peaks of the commercial FeS_2, the Raman bands of mesoporous FeS_2 are very broad, indicating the structural disorder in the mesostructured. All characteristic vibrational modes are in agreement with previous literature reported on pyrite FeS_2.[13,25] The composition of the mesoporous pyrite FeS_2 was investigated by energy dispersive X-ray spectrum (EDX), which reveals a ratio of S/Fe of 2.3.

Scanning electron microscopy (SEM) images for the meso FeS_2 sample were shown in **Figure 4.4a**. It is clearly seen that the pores are well-dispersed all over the spherical material. As a

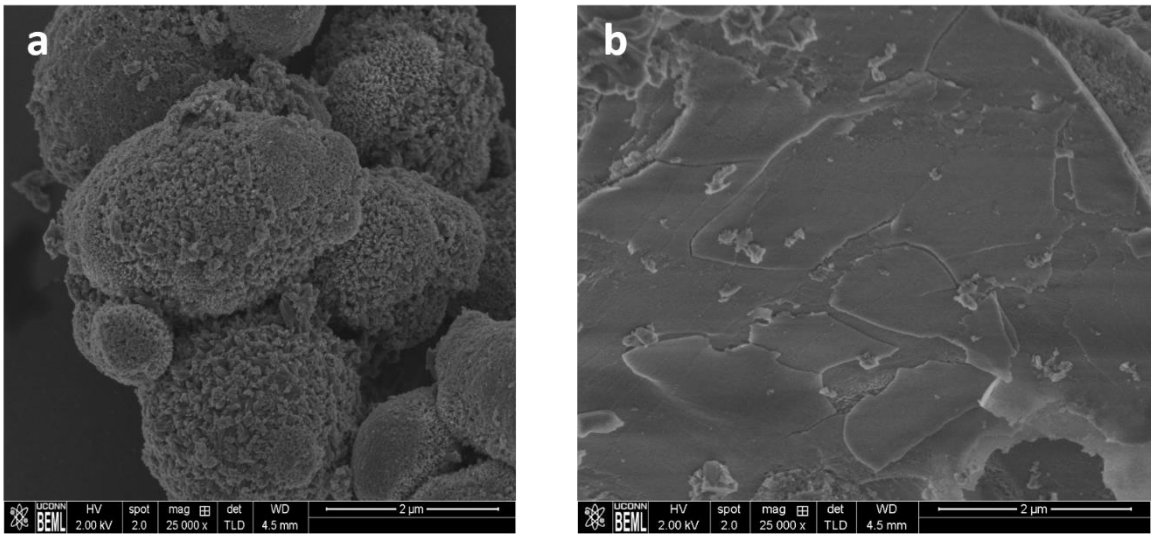

Figure 4.4 SEM images of (a) meso FeS_2 and (b) comm FeS_2.

comparison, the SEM imaging of commercial FeS_2 material was also conducted (**Figure 4.4b**). A chunky morphology is shown, indicating no porosity could be obtained in the commercial FeS_2 material. Transmission electron microscopy (TEM) was used to further demonstrate the mesoporous structure and crystallinity. As shown in **Figure 4.5a** and **4.5b**, the loose internal structure of FeS_2 spheres confirms the existence of mesopores with a pore size in the range of 4-7 nm. The crystal sizes of the mesoporous FeS_2 spheres are in agreement with the calculated value based on the XRD pattern (20 nm). In **Figure 4.5c**, the lattice fringe shows an interplanar distance of 0.31 nm corresponding to the (111) planes of pyrite FeS_2. Furthermore, the high-angle annular dark-field TEM image (**Figure 4.5d**) clearly indicated a mesoporous nanostructure of meso FeS_2. The corresponding element mapping results show a homogeneous nature of the as-prepared material, in which Fe and S are uniformly distributed in the mapping image of FeS_2 (**Figure 4.5e-g**).

To estimate the pore size distribution and the surface area, nitrogen adsorption-desorption measurements were performed. The isotherm of the mesoporous FeS_2 reveals a type-IV adsorption

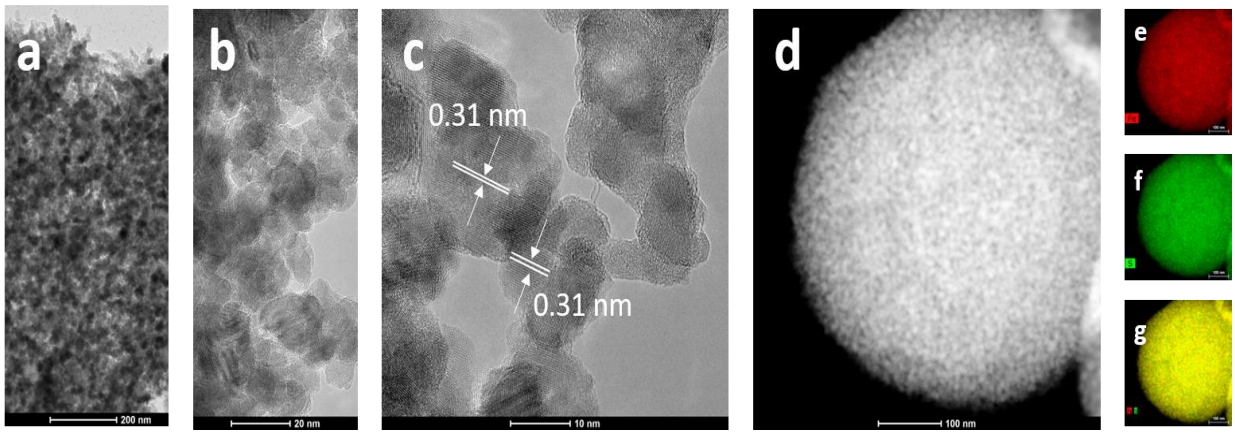

Figure 4.5 (a-c) Low- and high-magnification TEM images, and (d) High-angle annular dark-field TEM image of meso FeS_2. (e-g) EDX elemental mapping of Fe and S for the meso FeS_2.

isotherm (**Figure 4.6a**), suggesting the existence of a mesoporous structure according to the IUPAC classification.[26] The Brunauer-Emmett-Teller (BET) surface area and total pore volume of the mesoporous FeS_2 were calculated to be 128 $m^2 \cdot g^{-1}$ and 0.23 $cm^3 \cdot g^{-1}$, respectively. The pore size distribution of the as-synthesized FeS_2 was obtained by the Barrett-Joyner-Halenda (BJH), which exhibits a monomodal pore size (3.4 nm). In contrast, the isotherm of the comm FeS_2 shows a nonporous structure with a surface area less than 1 $m^2 \cdot g^{-1}$. The mesoporous structure of meso FeS_2 was further confirmed by the low-angle XRD (**Figure 4.6b**). The small diffraction angles can be an indicator of the existence of mesoporous structure due to the fact that most mesoporous materials are amorphous on the atomic scale and thus process large unit cells.[27,28]

X-ray photoelectron spectroscopy (XPS) was carried out to investigate the oxidation states of each element. As shown in **Figure 4.7**, the survey spectrum revealed Fe, S species in the material, which is consistent with the EDX results. The peak deconvolution was carried out using Gaussian−Lorentzian curve fitting based on the Shirley background correction. The high-resolution Fe 2p spectrum (**Figure 4.7a**) exhibits two predominant peaks at 707 and 720 eV, corresponding to Fe $2p_{3/2}$ and Fe $2p_{1/2}$ doublet splitting features due to spin-orbit coupling,

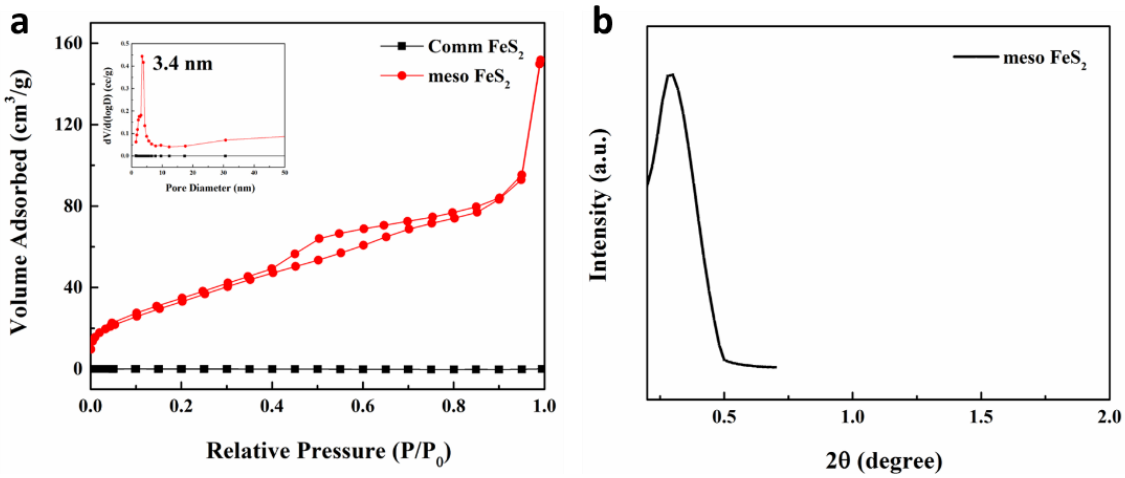

Figure 4.6 (a) N_2 sorption isotherms and the corresponding pore size distribution of commercial FeS_2 and mesoporous FeS_2. (b) low angle XRD patterns of mesoporous FeS_2.

---

respectively. The low-binding energy peak at 706.9 eV is due to the electron-deficient Fe^{2+} species, produced by the breaking of Fe (II)-S bond.[29] The two broad shoulder peaks at high binding energy are possibly attributed to the Fe^{3+} species from the surface oxidation.[30] Compared to the commercial FeS_2 sample, an obvious shift to higher binding energy was observed for the mesoporous FeS_2 sample without changing the energy difference between Fe $2p_{3/2}$ and Fe $2p_{1/2}$ peaks. The presence of mesoporous structure makes the material more accessible to the oxidants, which facilitates the surface oxidation.[31] **Figure 4.7b** shows the S 2p XPS spectrum. The major peak at 162.2 eV could be ascribed to the disulfide ions (S_2^{2-}) on the surface, while the minor peak at 163. 5 eV was attributed to the polysulfides (S_n^{2-}).[29] The sulfur peak at 169.1 eV in **Figure 4.7b** could be attributed to iron sulfate species (SO_4^{2-}).[14,32]

4.3.3 Hydrogen Evolution Reaction (HER) Performance

The electrocatalytic HER performance for the mesoporous FeS_2 was then carefully investigated using a three-electrode system under alkaline media. For comparison, the HER activity of commercial FeS_2, Pt/C (20%), and bare Ni foam was also measured. As depicted in **Figure 4.8a**,

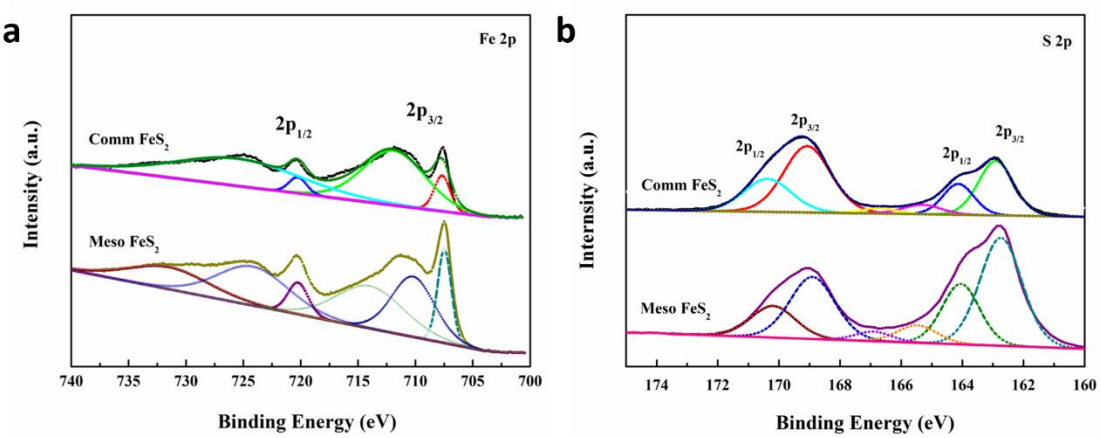

Figure 4.7 High-resolution XPS patterns of (a) Fe 2p, and (b) S 2p. Lower and upper curves are comm FeS_2 and meso FeS_2, respectively.

---

the mesoporous FeS_2 coated electrode requires a significant small overpotential of 96 mV to achieve a current density of 10 $mA \cdot cm^{-2}$, which is comparable to the state-of-the-art HER catalyst in alkaline media at the same mass loading density. In contrast, bare Ni foam shows little HER activity, and the commercial FeS_2 requires a large overpotential to reach a 10 $mA \cdot cm^{-2}$ current density.

The Tafel slope is an important indicator or reaction kinetics and the rate-determining step in the HER process, which reveals the extra voltage required to increase current density by 10-fold. In a whole HER process, the hydrogen evolution steps involve the adsorbed H atom discharge reaction, followed by electrochemical desorption of OH^- and H_2 (Volmer-Heyrovsky mechanism), or the direct recombination of two adsorbed H atoms to release H_2 (Volmer-Tafel mechanism).[33,34] In **Figure 4.8b**, the calculated value for meso FeS_2 is about 78 mV/dec, indicating a fast Volmer-Heyrovsky mechanism. Such a mechanism involved an electrochemical desorption of hydrogen as the rate-determine step.[10] Furthermore, the exchange current density (j_0) was calculated by an extrapolation method from Tafel plots (**Figure 4.8c**). The exchange current density value is highly dependent on the nature of the electrode material, which suggests the intrinsic electron transfer

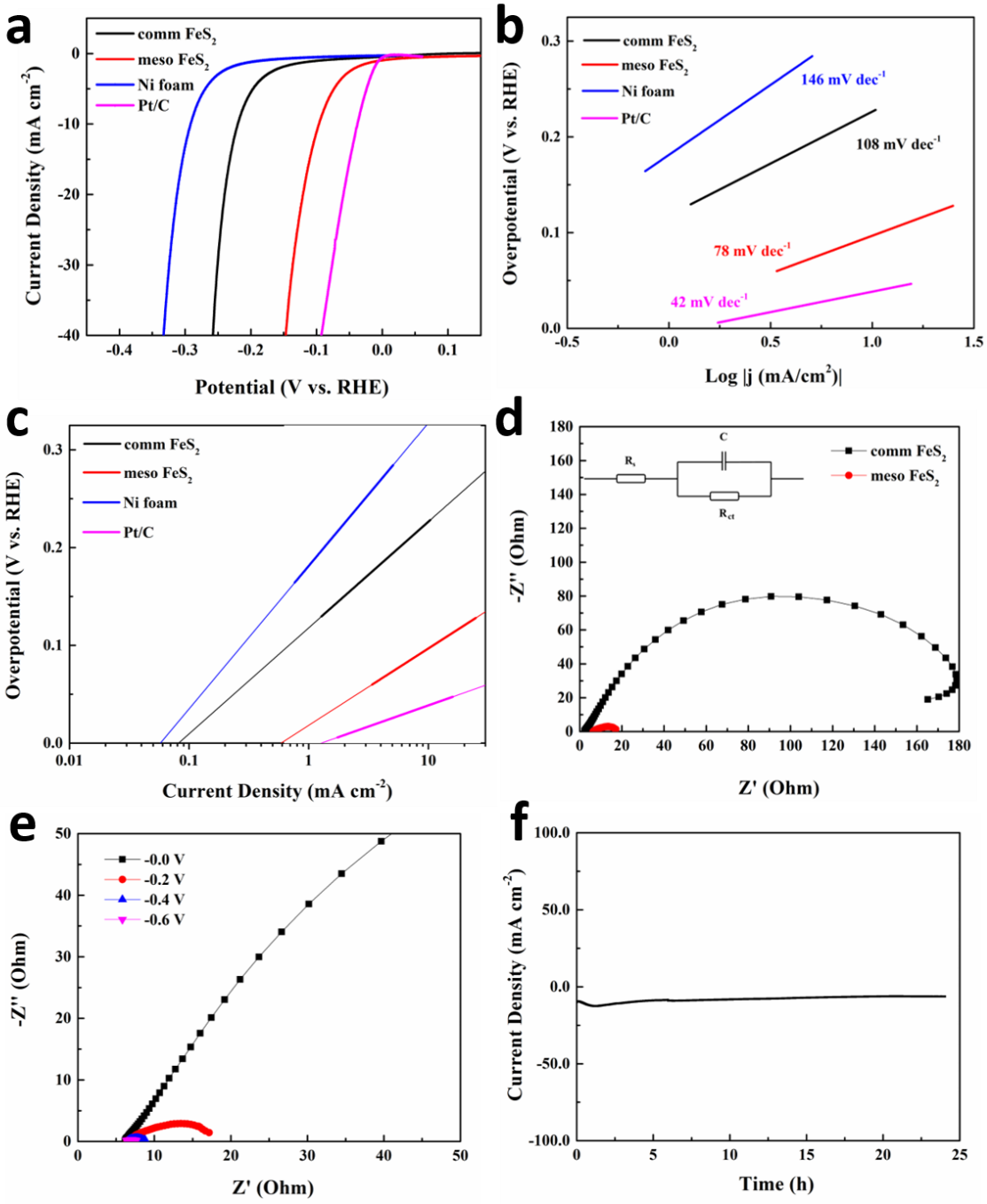

Figure 4.8 HER performance of the mesoporous FeS_2. (a) Polarization curves and (b) Tafel plots of the commercial FeS_2, mesoporous FeS_2, 20% Pt/C, and the bare Ni foam in 0.1 M KOH at a scan rate of 10 mV/s. (c) Exchange current densities for HER calculated from Tafel plots via extrapolation method. (d) Nyquist plots of commercial FeS_2 and mesoporous FeS_2 at an overpotential of 200 mV. The inset shows the fitted equivalent circuit. (e) Nyquist plots of the mesoporous FeS_2 at 0.00, -0.20, -0.40, and -0.60 V versus RHE, respectively. (f) Chronoamperometry curve of the mesoporous FeS_2 at a constant overpotential of 100 mV.

rates between the electrode and the electrolyte. The j_0 value of mesoporous FeS_2 for HER is 6.3×10^{-1} mA·cm^{-2}, which is 7 times that of commercial FeS_2 (8.4×10^{-2} mA·cm^{-2}).

Electrochemical impedance spectroscopy (EIS) was applied to investigate the electrode kinetics under HER operating conditions. The EIS results were fitted into an equivalent circuit, as shown in the inset of **Figure 4.8d**. The semicircle in the high-frequency range of Nyquist plot revealed the charge transfer resistance (R_{ct}), which suggests that mesoporous FeS_2 (7**Ω**) has a much lower charge transfer resistance than that of commercial FeS_2 (238**Ω**). The small R_{ct} value indicates the high electron transport efficiency and a more favorable HER kinetics at the mesoporous FeS_2 electrode. The Nyquist plots in **Figure 4.8e** also exhibit the change in R_{ct} values in the potential range of 0 to -0.6 V, which is in consistent with the polarization plots of meso FeS_2 in **Figure 4.8a**.

Durability is another important criterion to evaluate a good electrocatalyst. The superior robustness of the mesoporous FeS_2 is confirmed by the chronopotentiometric curve in **Figure 4.8f**. The potential required to reach a current density of 10 mA·cm^{-2} was a constant value without any obvious increase even after 24 h, indicating the superior durability of the as-prepared mesoporous FeS_2.

4.4 Discussion

This study aims to overcome obstacles in synthesizing mesoporous iron sulfides with high surface areas and applying the resulting material as efficient hydrogen evolution electrocatalysts in alkaline media. Mesoporous iron sulfide was synthesized by a sol-gel method followed by a gas phase sulfurization approach. The chemisorbed carboxyl groups from the oxidation of surfactant can be removed during calcination at 150 °C, while the remaining nitrate groups are not fully removed until 250 °C. A further slow removal of the remaining carboxyl and nitrate groups occurred during sulfurization under a helium flow at 250 °C.[21] During the sulfurization process,

the oxide to sulfide conversion is done under a flow of H_2S and He. The H_2S and sulfur powder could serve as a reducing agent to reduce Fe^{3+} to Fe^{2+}. Simultaneously, the remaining nitrate species reacts with H_2S, resulting in the production of extra sulfur powder. The sulfur powder sublimed to sulfur vapor and also acts as a reducing agent. The additional sulfur favors the formation of the pyrite phase FeS_2 with a desired 1:2 stoichiometric ratio.

In this study, the mesoporous FeS_2 materials have shown excellent performance toward electrochemical hydrogen evolution reaction. Commercial FeS_2 with extremely low surface area exhibits little HER performance due to their limited exposed active sites.[35] Compared to the commercial FeS_2 materials, the improved HER activity of the mesoporous FeS_2 materials is attributed to the mesoporous properties, as the structure of an electrocatalyst plays a decisive role in catalytically activities. First, higher surface area leads to more catalytic active sites in general.[36,37] As shown in the N_2 sorption results (**Figure 4.6a**), the surface area of mesoporous FeS_2 (128 $m^2 \cdot g^{-1}$) is much higher than that of commercial FeS_2 (<1 $m^2 \cdot g^{-1}$). The loose internal structure as shown in the SEM image of the mesoporous FeS_2 spheres offers more exposed accessible channels. Thus, the mesoporous structure of FeS_2 provides abundant interfacial catalytically active sites for the HER process. Secondly, the charge transfer rate has a great effect on HER activity.[10] As exhibited by the much lower charge-transfer impedance of mesoporous FeS_2 than that of the commercial FeS_2 (**Figure 4.8d**), the mesoporous structure significantly facilitates charge transfer. Thirdly, the interconnected mesopores also facilitate mass transport by enhancing the contact of reactant ions (e.g., OH^-) with active sites as well as the diffusion of product molecules.[19,24] Overall, the mesoporous structure significantly promotes the mass and charge transport efficiencies, giving rise to an improved HER activity.

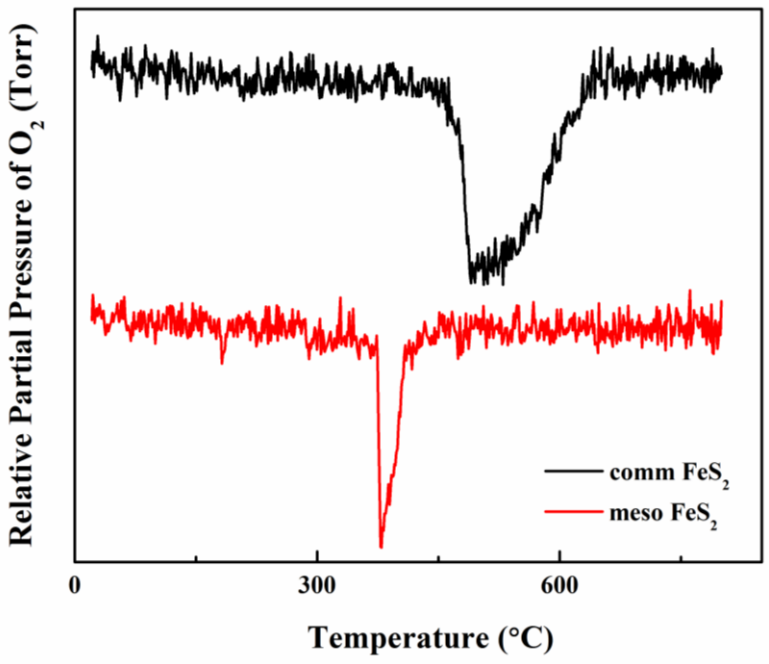

Figure 4.9 Oxygen temperature-programmed oxidation (O_2-TPO) for comm FeS_2 and meso FeS_2 samples.

The sulfur-deficient structure might also play an important role in HER activities. Raman spectroscopy was used to examine defects. **Figure 4.3b** shows two characteristic bands of pyrite FeS_2 E_g and A_g. The obvious Raman shift of both E_g and A_g peaks suggests the existence of sulfur vacancies, which can serve as active sites in the HER process.[20,38] In order to further investigate sulfur vacancies, oxygen temperature-programmed oxidation (O_2-TPO) was carried out. As revealed in **Figure 4.9**, the O_2-TPO curve of the comm-FeS_2 sample shows an oxygen consumption peak around 500 °C. Whereas, the oxygen consumption peak shifted to a much lower temperature for the mesoporous FeS_2 sample, suggesting predominantly sulfur vacancies in the mesoporous structure.

The HER under alkaline conditions is sluggish compared to the acidic HER process due to the limited number of available protons. Generally, there are two HER reaction mechanisms under alkaline conditions, including the Volmer-Tafel mechanism and the Volmer-Heyrovsky

mechanism.[39,40] The first step in the HER process is a primary proton discharge to form adsorbed hydrogen species (H_{ads}), which is called the Volmer reaction. The second step is either an electrochemical desorption step (Heyrovsky reaction) or a recombination step of adsorbed hydrogen (Tafel reaction) on catalysts.[39,41] To investigate the HER reaction kinetics and mechanistic pathways, experimentally obtained Tafel slope value can provide useful information. The Tafel slope is an intrinsic property of a catalyst. A small Tafel slope suggests a prominently enhanced HER rate with a moderate additional voltage.[35,42] In **Figure 4.8b**, a Tafel slope of 78 $mV \cdot dec^{-1}$ is obtained for the mesoporous FeS_2 sample, suggesting a fast Volmer-Heyrovsky HER reaction rate. In contrast, the commercial FeS_2 sample possessed a much larger Tafel slope value of 108 $mV \cdot dec^{-1}$, which is defined to follow a slow proton discharge reaction due to insufficient active sites.

4.5 Conclusions

In summary, the mesoporous FeS_2 materials with high surface area and abundant accessible active sites were synthesized via a two-step synthetic protocol, without the aid of a hard template. The as-synthesized mesoporous FeS_2 has a much higher surface area (128 $m^2 \cdot g^{-1}$) than the commercial FeS_2 (<1 $m^2 \cdot g^{-1}$). The resulting meso FeS_2 acts as a remarkable HER electrocatalyst in alkaline media with an exceptionally low overpotential of 96 mV at a current density of 10 $mA \cdot cm^{-2}$, a small Tafel slope of 78 mV/dec, and a superior long-term stability. The improved HER catalytic activities are attributed to the increased number of active sites resulting from the mesoporous structure. The synthetic strategy of mesoporous iron sulfide provides new insights of engineering the mesostructures of metal sulfides and is expected to be a generic method to synthesize other metal chalcogenides. In light of the excellent HER electrocatalytic performance, the mesoporous FeS_2 materials reported here with the high surface area might be promising

alternatives to Pt-based HER catalysts, thus facilitating the development of electrocatalytic water splitting.

4.6 References

(1) Yang, H.; Zhang, Y.; Hu, F.; Wang, Q. *Nano Lett.* **2015**, *15* (11), 7616.

(2) Shi, Y.; Wang, J.; Wang, C.; Zhai, T. T.; Bao, W. J.; Xu, J. J.; Xia, X. H.; Chen, H. Y. *J. Am. Chem. Soc.* **2015**, *137* (23), 7365.

(3) McCrory, C. C. L.; Jung, S.; Ferrer, I. M.; Chatman, S. M.; Peters, J. C.; Jaramillo, T. F. *J. Am. Chem. Soc.* **2015**, *137* (13), 4347.

(4) Li, D.; Baydoun, H.; Verani, C. N.; Brock, S. L. *J. Am. Chem. Soc.* **2016**, *138* (12), 4006.

(5) Lv, H.; Xi, Z.; Chen, Z.; Guo, S.; Yu, Y.; Zhu, W.; Li, Q.; Zhang, X.; Pan, M.; Lu, G.; Mu, S.; Sun, S. *J. Am. Chem. Soc.* **2015**, *137*, 5859.

(6) Miao, R.; He, J.; Sahoo, S.; Luo, Z.; Zhong, W.; Chen, S.; Guild, C.; Jafari, T.; Dutta, B.; Cetegen, S. A.; Wang, M.; Alpay, S. P.; Suib, S. L. *ACS Catal.* **2017**, *7*, 819.

(7) Gao, M.-R.; Xu, Y.-F.; Jiang, J.; Yu, S.-H. *Chem. Soc. Rev.* **2013**, *42* (7), 2986.

(8) Kong, D.; Cha, J. J.; Wang, H.; Lee, H. R.; Cui, Y. *Energy Environ. Sci.* **2013**, *6*, 3553.

(9) Lee, S. C.; Benck, J. D.; Tsai, C.; Park, J.; Koh, A. L.; Abild-Pedersen, F.; Jaramillo, T. F.; Sinclair, R. *ACS Nano* **2016**, *10*, 624.

(10) Wang, J.; Wang, W.; Wang, Z.; Chen, J. G.; Liu, C. *ACS Catal.* **2016**, *6*, 6585.

(11) Liu, Y.; Cheng, H.; Lyu, M.; Fan, S.; Liu, Q.; Zhang, W.; Zhi, Y.; Wang, C.; Xiao, C.; Wei, S.; Ye, B.; Xie, Y. *J. Am. Chem. Soc.* **2014**, *136*, 15670.

(12) Yu, B.; Wang, X.; Qi, F.; Zheng, B.; He, J.; Lin, J.; Zhang, W.; Li, Y.; Chen, Y. *ACS Appl. Mater. Interfaces* **2017**, *9*, 7154.

(13) Faber, M. S.; Lukowski, M. A.; Ding, Q.; Kaiser, N. S.; Jin, S. *J. Phys. Chem. C* **2014**, *118*, 21347.

(14) Wang, D.; Gong, M.; Chou, H.; Pan, C.; Chen, H.; Wu, Y.; Lin, M.; Guan, M.; Yang, J.; Chen, C.; Wang, Y.; Hwang, B.; Chen, C.; Dai, H. *J. Am. Chem. Soc.* **2015**, *137*, 1587.

(15) Samad, L.; Caba, M.; Shearer, M. J.; Park, K.; Hamers, R. J.; Jin, S. *Chem. Mater.* **2015**, *27*, 3108.

(16) Rickard, D.; Iii, G. W. L. *Chem. Rev.* **2007**, *107*, 514.

(17) Yonemoto, B. T.; Hutchings, G. S.; Jiao, F. *J. Am. Chem. Soc.* **2014**, *136*, 8895.

(18) Kresge, C. T.; Leonowicz, M. E.; Roth, W. J.; Vartuli, J. C.; Beck, J. S. *Nature* **1992**, *359*, 710.

(19) Sun, T.; Xu, L.; Yan, Y.; Zakhidov, A. A.; Baughman, R. H.; Chen, J. *ACS Catal.* **2016**, *6*, 1446.

(20) Wu, Z.; Guo, J.; Wang, J.; Liu, R.; Xiao, W.; Xuan, C.; Xia, K.; Wang, D. *ACS Appl. Mater. Interfaces* **2017**, *9*, 5288.

(21) Poyraz, A. S.; Kuo, C.; Biswas, S.; Suib, S. L. *Nat. Commun.* **2013**, *4*, 2952.

(22) Jiang, T.; Poyraz, A. S.; Iyer, A.; Zhang, Y.; Luo, Z.; Zhong, W.; Miao, R.; El-Sawy, A. M.; Guild, C. J.; Sun, Y.; Kriz, D. a.; Suib, S. L. *J. Phys. Chem. C* **2015**, *119*, 10454.

(23) Song, W.; Poyraz, A. S.; Meng, Y.; Ren, Z.; Chen, S.; Suib, S. L. *Chem. Mater.* **2014**, *26*, 4629.

(24) Luo, Z.; Miao, R.; Huan, T. D.; Mosa, I. M.; Poyraz, A. S.; Zhong, W.; Cloud, J. E.; Kriz, D. A.; Thanneeru, S.; He, J.; Zhang, Y.; Ramprasad, R.; Suib, S. L. *Adv. Energy Mater.* **2016**, *6*, 1600528.

(25) Jiang, F.; Peckler, L. T.; Muscat, A. J. *Cryst. Growth Des.* **2015**, *15* (8), 3565.

(26) Search, H.; Journals, C.; Contact, A.; Iopscience, M.; Address, I. P. *reports Prog. Phys.*

1999, *62*, 1573.

(27) Jiao, F.; Harrison, A.; Jumas, J. C.; Chadwick, A. V.; Kockelmann, W.; Bruce, P. G. *J. Am. Chem. Soc.* **2006**, *128* (16), 5468.

(28) Miao, R.; Luo, Z.; Zhong, W.; Chen, S.-Y.; Jiang, T.; Dutta, B.; Nasr, Y.; Zhang, Y.; Suib, S. L. *Appl. Catal. B Environ.* **2016**, *189*, 26.

(29) Shukla, S.; Loc, N. H.; Boix, P. P.; Koh, T. M.; Prabhakar, R. R. *ACS Nano* **2014**, *8*, 10597.

(30) Long, X.; Li, G.; Wang, Z.; Zhu, H.; Zhang, T.; Xiao, S.; Guo, W.; Yang, S. *J. Am. Chem. Soc.* **2015**, *137* (37), 11900.

(31) Jones, C. J.; Chattopadhyay, S.; Gonzalez-Pech, N. I.; Avendano, C.; Hwang, N.; Lee, S. S.; Cho, M.; Ozarowski, A.; Prakash, A.; Mayo, J. T.; Yavuz, C.; Colvin, V. L. *Chem. Mater.* **2015**, *27* (3), 700.

(32) Feng, L.-L.; Yu, G.; Wu, Y.; Li, G.-D.; Li, H.; Sun, Y.; Asefa, T.; Chen, W.; Zou, X. *J. Am. Chem. Soc.* **2015**, *137*, 14023.

(33) Conway, B. E.; Tilak, B. V. *Electrochim. Acta* **2002**, *47*, 3571.

(34) Jin, H.; Wang, J.; Su, D.; Wei, Z.; Pang, Z.; Wang, Y. *J. Am. Chem. Soc.* **2015**, *137* (7), 2688.

(35) Duan, J.; Chen, S.; Jaroniec, M.; Qiao, S. Z. *ACS Nano* **2015**, *9* (1), 931.

(36) Ledendecker, M.; Clavel, G.; Antonietti, M.; Shalom, M. *Adv. Funct. Mater.* **2015**, *25*, 393.

(37) Kibsgaard, J.; Chen, Z.; Reinecke, B. N.; Jaramillo, T. F. *Nat. Mater.* **2012**, *11*, 963.

(38) Yuan, B.; Luan, W.; Tu, S. *Dalt. Trans.* **2012**, *41*, 772.

(39) Anantharaj, S.; Ede, S. R.; Sakthikumar, K.; Karthick, K.; Mishra, S.; Kundu, S. *ACS Catal.* **2016**, *6*, 8069.

(40) Subbaraman, R.; Tripkovic, D.; Chang, K.-C.; Strmcnik, D.; Paulikas, A. P.; Hirunsit, P.;

Chan, M.; Greeley, J.; Stamenkovic, V.; Markovic, N. M. *Nat. Mater.* **2012**, *11* (6), 550.

(41) Xie, J.; Zhang, J.; Li, S.; Grote, F.; Zhang, X.; Zhang, H.; Wang, R.; Lei, Y.; Pan, B.; Xie, Y. *J. Am. Chem. Soc.* **2013**, *135*, 17881.

(42) Tian, J.; Liu, Q.; Asiri, A. M.; Sun, X. *J. Am. Chem. Soc.* **2014**, *136*, 7587.

Future Work

In this thesis, controlled synthesis of transition metal oxide/sulfide-based composite materials have been developed. The prepared functional materials have been characterized and applied in various energy and environmentally related applications. However, there is still much more to be explored. As a future perspective, the current methods can be further optimized and developed in the following aspects.

In the work of mesoporous TiO_2, incorporation of other semiconductors with TiO_2 can possibly adjust the band gap via constructing a heterojunction structure. A close contact between the two components could be achieved due to the mesoporous structure of TiO_2, which can possibly lead to a high charge transfer efficiency. Photocatalytic hydrogen evolution and photocatalytic CO_2 reduction by modified mesoporous TiO_2 are worthy of critical study.

In the work of water splitting on reduced graphene oxide supported NMC composite electrode materials, several goals can be pursued considering the current limitations. Synthesis of porous NMC with different physicochemical properties and improved surface area can be performed by tuning the solvent and amphiphilic surfactant system. Optimization of the metal ratios in the ternary oxide/sulfide system can also possibly alter the conductivity of the composite materials, which is necessary to explore their potential application in lithium ion batteries.

In the work of mesoporous FeS_2, the synthetic route of obtaining mesoporous FeS_2 can potentially be applied to other transition metal chalcogenides. Apart from the current synthetic method, FeS_2 prepared from dissolving commercial Fe_2O_3 combined with a soft template could be a cost effective and facile synthetic pathway. As for exploring water splitting electrocatalysts, porous iron phosphosulfide could be a promising candidate.

Appendix

List of Publications and Patent Applications

- Liu, G.; Liu, J.; Li, W.; Liu, C.; Wang, F.; He, J.; Guild, C.; Jin, J.; Kriz, D. A.; **Miao, R**.; Suib, S. L. "Aerobic oxidation of alcohols over Ru-Mn-Ce and Ru-Co-Ce catalysts:The effect of calcination temperature" *Appl. Catal. A General*. **2017**, *535*, 77–84.
- **Miao, R**.; He, J.; Sahoo, S.; Luo, Z.; Zhong, W.; Chen, S.-Y.; Guild, C.; Jafari, T.; Dutta, B.; Cetegen, S. A.; Wang, M.; Alpay, P. S.; Suib, S. L. "Reduced Graphene Oxide Supported Nickel-Manganese-Cobalt Spinel Ternary Oxide Nanocomposites and Their Chemical-Converted Sulfide Nanocomposites as Efficient Electrocatalysts for Alkaline Water Splitting" *ACS Catalysis* **2017**, *7*, 819−832.
- Jafari, T.; Moharreri, E.; Amin, A.; **Miao, R**.; Song, W.; Suib, S. L. "Photocatalytic Water Splitting—The Untamed Dream: A Review of Recent Advances" *Molecules* **2016**, *21*, 900.
- Luo, Z.; **Miao, R.**; Huan, T. D.; Mosa, I. M.; Poyraz, A. S.; Zhong, W.; Cloud, J. E.; Kriz, D. A.; Thanneeru, S.; He, J.; Zhang, Y.; Ramprasad, R.; Suib, S. L. "Mesoporous MoO_{3-x} Material as an Efficient Electrocatalyst for Hydrogen Evolution Reactions" *Adv. Energy Mater.* **2016**, *6*, 1600528.
- Luo, Z.; Cetegen, S. A.; **Miao, R.**; Jiang, T., Chen, S.-Y.; Jafari, T.; Zhang, Y.; Suib, S. L. "Structure–property relationships of copper modified mesoporous TiO_2 materials on alkyne homocoupling reactions" *J. Catal.* **2016**, *336*, 41–48.
- Pahalagedara, M. N.; Pahalagedara, L. R.; He, J.; **Miao, R.**; Gottlieb, B.; Rathnayake, D.; Suib, S. L. "Room temperature selective reduction of nitrobenzene to azoxybenzene over magnetically separable urchin-like Ni/Graphene nanocomposites" *J. Catal.* **2016**, *336*, 41–48.
- Wang, M.; **Miao, R.**; He, J.; Xu, X.; Liu, J.; Du, H. "Silicon Carbide whiskers reinforced polymer-based adhesive for joining C/C composites" *Mater. Design* **2016**, *99*, 293-302.
- He, J.; Liu, Y.; Meng, Y.; Sun, X.; Biswas, S.; Shen, M.; Luo, Z.; **Miao, R.**; Zhang, L.; Mustain, W. E.; Suib, S. L. "High-rate long-life of Li-ion batteries using reduced graphene oxide·Co_3O_4 as anode materials" *RSC Adv.* **2016**, *6*, 24320–24330.

- **Miao, R.**; Luo, Z.; Zhong, W.; Chen, S.-Y.; Jiang, T.; Dutta, B.; Nasr, Y.; Zhang, Y.; Suib, S. L. "Mesoporous TiO_2 modified with carbon quantum dots as a high-performance visible light photocatalyst" *Appl. Catal. B Environ*. **2016**, *189*, 26–38.
- Wang, M.; Tao, X.; Xu, X.; **Miao, R.**; Du, H.; Liu, J.; Guo, A. "High-temperature bonding performance of modified heat-resistant adhesive for ceramic connection" *J. Alloy. Compd.* **2016**, *663*, 82-85.
- Zhang, Y.; Jin, L.; Sterling, K.; Luo, Z.; Jiang, T.; **Miao, R.**; Guild, C.; Suib, S. L. "Potassium modified layered $Ln_2O_2CO_3$ (Ln La, Nd, Sm, Eu) materials efficient and stable heterogeneous catalysts for biofuel production" *Green Chem.,* **2015**, *17*, 3600-3608.
- Jiang, T.; Poyraz, A. S.; Iyer, A.; Zhang, Y.; Luo, Z.; Zhong, W.; **Miao, R.**; El-Sawy, A. M.; Guild, C.; Sun, Y.; Kriz, D. A.; Suib, S. L. "Synthesis of Mesoporous Iron Oxides by an Inverse Micelle Method and Their Application in the Degradation of Orange II under Visible Light at Neutral pH" *J. Phys. Chem. C* **2015**, *119*, 10454−10468.
- Luo, Z.; Poyraz, A. S.; Kuo, C.-H.; **Miao, R.**; Meng, Y.; Chen, S.-Y.; Jiang, T.; Wenos, C.; Suib, S. L. "Crystalline Mixed Phase (Anatase/Rutile) Mesoporous Titanium Dioxides for Visible Light Photocatalytic Activity" *Chem. Mater*. **2015**, *27*, 6–17.

Patent applications

Miao, R.; Dutta, B.; Suib, S. L. "Preparation methods of porous pyrite iron sulfide materials" filed in October 2015.